LATVIAN JOURNAL of PHYSICS and TECHNICAL SCIENCES

ISSN 0868 - 8257

(Vol. 58)

2021

CONTENTS

LATVIAN JOURNAL of PHYSICS and TECHNICAL SCIENCES

LATVIJAS FIZIKAS un TEHNISKO ZINĀTŅU ŽURNĀLS

ЛАТВИЙСКИЙ ФИЗИКО-ТЕХНИЧЕСКИЙ ЖУРНАЛ

Published six times a year since February 1964
Iznāk sešas reizes gadā kopš 1964. gada februāra
Выходит шесть раз в год с февраля 1964 года

2 (Vol. 58) • 2021

RĪGA

Language Editor: O. Ivanova
Computer Designer: I. Begicevs

INDEXED (PUBLISHED) IN

www.scopus.com
www.sciendo.com
EBSCO (Academic Search Complete, www.epnet.com), INSPEC (www.iee.org.com).
VINITI (www.viniti.ru), Begell House Inc/ (EDC, www.edata-center.com).

Issuers: Institute of Physical Energetics,
Institute of Solid State Physics, University of Latvia
Registration Certificate Number: 000700221

Editorial Contacts:
11 Krivu Street, Riga, LV - 1006
Ph.: + 371 67551732
E-mail: leo@lza.lv
www.fei-web.lv

sciendo

LATVIAN JOURNAL OF PHYSICS
AND TECHNICAL SCIENCES
2021, N 2

DOI: 10.2478/lpts-2021-0007

AB-INITIO CALCULATIONS OF OXYGEN VACANCY IN Ga_2O_3 CRYSTALS

A. Usseinov[1*], Zh. Koishybayeva[1*], A. Platonenko[2], A. Akilbekov[1], J. Purans[2], V. Pankratov[2], Y. Suchikova[3], A. I. Popov[1, 2, 4*]

[1]L.N. Gumilyov Eurasian National University,
2 Satpaeva Str., Nur-Sultan, KAZAKHSTAN
[2]Institute of Solid State Physics, University of Latvia,
8 Kengaraga Str., Riga, LV-1063, LATVIA
[3]Berdyansk State Pedagogical University,
4 Schmidta St., Berdyansk, 71100, UKRAINE
[4]Institute of Physics, University of Tartu,
1 W. Ostwald Str , Tartu, 50411, ESTONIA
*E-mail: usseinov_ab@enu.kz, zhanymgul.k@zerek.kz,
popov@latnet.lv

Gallium oxide β-Ga_2O_3 is an important wide-band gap semiconductor. In this study, we have calculated the formation energy and transition levels of oxygen vacancies in β-Ga_2O_3 crystal using the B3LYP hybrid exchange-correlation functional within the LCAO-DFT approach. The obtained electronic charge redistribution in perfect Ga_2O_3 shows notable covalency of the Ga-O bonds. The formation of the neutral oxygen vacancy in β-Ga_2O_3 leads to the presence of deep donor defects with quite low concentration. This is a clear reason why oxygen vacancies can be hardly responsible for n-type conductivity in β-Ga_2O_3.

Keywords: *β-Ga_2O_3, ab-initio calculations, band structure, DFT, oxygen vacancy.*

1. INTRODUCTION

Performance optimization of the functional properties of many advanced oxide materials depends on the control of point structural defects and also on a deep knowledge and understanding of their various properties and characteristics [1]–[9]. Special attention has recently been paid to gallium oxide β-Ga_2O_3 as a very promising candidate for optoelectronic devices operating at short wavelengths. Due to its wide band gap and possible modulation of optical properties by synthesis methods and doping impurities, it is a very attractive material for use in different optoelectronic devices, as well as in photocatalysis, optical fibres and scintillators [10]–[17].

One of the most important areas of both research and application is the control of electrical conductivity through doping of the material. Traditionally, in many oxygen-containing materials, oxygen vacancies (V_O) are considered a source of electrical conductivity [1], [2], [10], [18], [19]. However, recent density functional theory (DFT) calculations of Ga_2O_3 have shown that oxygen vacancies do not play a key role in conductivity [20]. At the same time, already small amounts of unintentional donors, like hydrogen, completely change the electronic structure and explain the observed activation energy of conductivity (1.7 eV) [20]. In this regard, DFT calculations play an exceptional role in understanding this fundamental issue through the study of the electronic structure and defects energetics.

In this paper, we present the results of *ab-initio* calculations of a pure and defective (with one oxygen vacancy) β-Ga_2O_3 crystal using the hybrid B3LYP exchange-correlation functional and the LCAO approximation. To describe the effect of oxygen vacancy onto electronic and conductivity properties, the charge transition levels as function of the Fermi energy have been calculated.

2. COMPUTATIONAL SET AND Ga_2O_3 CRYSTAL STRUCTURE

Large-scale *ab initio* calculations have been performed using a linear combination of atomic orbital method within the density functional theory (LCAO-DFT) approach. The hybrid B3LYP [21] functional has been used, allowing us to perform very accurate calculations of the band gap, unlike the standard LDA or GGA-type functionals. The basic sets for Ga and O atoms have been taken from Ref. [22], [23], respectively. The integration over the Brillouin zone in the reciprocal space has been performed within a 4×4×4 Pack-Monkhorst grid [24]. Effective atomic charges have been estimated using the Mulliken population analysis [25].

The β-Ga_2O_3 unit cell is shown in Fig. 1, where a⊥c, b⊥c, and the angle between *a* and *c* axes is 104°. The lattice parameters are *a* = 12.19 Å, *b* = 3.05 Å, and *c* = 5.82 Å. By symmetry, there are two distinct Ga sites, labelled Ga(1) and Ga(2) (Fig. 1). The Ga(1) atoms are bonded to four neighbouring O atoms in a (roughly) tetrahedral arrangement. The Ga(2) atoms are in an octahedral environment and bind to six neighbouring O atoms. The O atoms have three distinct sites: O(1) and O(2) bind to three Ga atoms, while O(3) binds to four Ga atoms. The Ga–O bond lengths range from

1.8 to 2.1 Å.

To simulate an oxygen vacancy, a periodic model of the extended unit cell of the crystal – a supercell – with an expansion matrix of 2×2×2 and containing 80 atoms has been used.

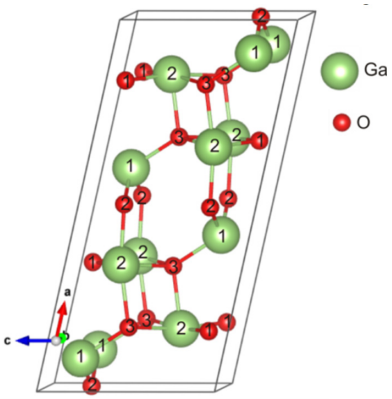

Fig. 1. Schematic representation of crystal structure of monoclinic β-Ga_2O_3. Unique positions of Ga/O atoms in the lattice are designated.

Further, we have calculated the bulk properties of pure Ga_2O_3 obtaining good agreement with the experimental data (Table 1). The optimized lattice parameters *a* and *c* slightly overestimate those obtained in experiments. The error in the estimate of band gap energies obtained using hybrid calculations has been found to be much smaller than the error in standard GGA-PBE or Hartree-Fock calculations (resulted in a huge underestimate/overestimate of the band gap). Proper estimate of band gap is an important point, since the correct description of formation energy depends on it. Mulliken's analysis showed a slight difference in the ionic charge on atoms with different positions in the crystal, which was associated with the anisotropy of the electronic properties [q(Ga1) +1.48e, q(Ga2) +1.58e, q(O1) = - 0.994e, q(O2) = - 0.997e, q(O3) = - 0.079e], as well as a considerable covalency of the Ga-O bonding (~ 0.2e).

Table 1. Bulk Properties of Pure β-Ga_2O_3 as Calculated by Means of DFT-LCAO Method

	HF	GGA-PBE	B3LYP	Exp [10]
a, Å	12.19	12.34	12.34	12.12÷12.34
b, Å	3.05	3.11	3.09	3.03÷3.04
c, Å	5.82	5.90	5.87	5.80÷5.87
E_g, eV (direct/indirect)	13.8	2.36/2.3	4.49/4.45	4.4÷5

3. FORMATION ENERGIES AND TRANSITION LEVELS

As it is known, formation energy of defect D with charge q in system X is defined as:

$$E_f = E_{tot}(D) - E_{tot}(X) + \sum_i n_i\mu_i + q(E_F + E_V) + E_{corr}, \quad (1)$$

where $E_{tot}(D)$ and $E_{tot}(X)$ are the total energies of the system with and without a defect, n_i represents the number of atoms of the element i that are removed from the system when a defect is formed (a negative value for n_i means the addition of atoms), μ_i is the chemical potential of element i, it is the energy of atoms that are removed

(or added) into the system when a defect is formed. The study is performed for dopant-rich condition, using molecular O_2 as a dopant source in the gas phase. The fourth term $q(E_F+E_V)$ is a change in the electron energy due to the exchange of electrons and holes with the carrier reservoirs. E_F+E_V is the Fermi energy relative to the maximum of the valence band of a defect-free system. E_{corr} term includes energy offset correction [26] and first-order Makov-Payne correction [27].

To calculate chemical potentials included in Eq. (1), we take the O_2 molecule (oxygen-rich conditions) and the Ga metal (oxygen-poor conditions) as limiting phases. Combining the expressions $\mu_O < 1/2\mu(O_2) = 1/2E_{tot}(O_2)$; $\mu_{Ga} < \mu_{Ga-metal} = E_{tot}(Ga)$; $2\mu_{Ga}+3\mu_O=\mu(Ga_2O_3)=E_{tot}(Ga_2O_3)$ and the formation energy of the compound $E_f(Ga_2O_3) = E_{tot}(Ga_2O_3)-2\mu_{Ga-metal}-3/2\mu(O_2)$, one gets the range of μ_O, the chemical potential of oxygen in gallium oxide:

$$1/2\mu(O_2) + 1/3\ E_f(Ga_2O_3) < \mu_O < 1/2\mu(O_2).$$

To determine the charge state transition levels for various defects, we used the approximation described by Lany and Zunger [28], based on previous studies by Scherz and Scheffler [29], stating that the transition level is the Fermi energy, at which the formation energy of a charged defect is equal to that of a neutral defect:

$$E_{tot}(D,q) - E_{tot}(X) + \sum_i n_i\mu_i + q\left(\varepsilon\left(\frac{q}{q'}\right) + E_V\right)$$
$$= E_{tot}(D,q') - E_{tot}(X) + \sum_i n_i\mu_i + q'\left(\varepsilon\left(\frac{q}{q'}\right) + E_V\right),$$

thus

$$\varepsilon(q/q') = \frac{E(D,q')-E(D,q)}{q-q'} - E_V. \quad (2)$$

The zero energy reference is set at the top of the valence band, E_V=0.We have considered cases in which an electronic charge is added to the system, i.e., the state q' corresponds to a state with an extra electron, q+1e: this corresponds to a transition from a neutral state to a negatively charged state, ε(0/-1).

4. RESULTS AND DISCUSSION

The formation energy for oxygen vacancies in three different crystallographic positions (see Fig.1) is shown in Fig. 2. Neutral V_O has the lowest energy on the O(3) site. The bend of the curve corresponds to the transition of the defect charge state. As formation energies for all types of V_O in 1+ charge state are around 2.5 eV, the oxygen vacancy is an example of a negative-U defect, where the 1+ charge state is unsta-

ble. At low Fermi energies, the 2+ charge state becomes more preferable, whereas when Fermi level is high, the neutral state becomes the most stable. For an oxygen-poor conditions, we obtain ε(2+/0)=4 eV for O(1), ε(2+/0)=3.8 eV for O(2), ε(2+/0)=3.1 eV for O(3). Under an oxygen-rich condition, formation energy increases by ~2.76 eV. Transition levels are equal or more than 1eV below CB. The amount of thermal energy required to promote an electron from the defect level to the CB is much greater than the room temperature; therefore, oxygen vacancies are *deep donors* and cannot serve as the effective source of the electron charge. Hence, oxygen vacancies cannot be responsible for n-type conductivity in Ga_2O_3. However, they can compensate acceptors by donating their electrons. As acceptor doping increases, the Fermi level is pushed down toward the VB. This reduces the formation energy for oxygen vacancies. At some point, the formation energy gets small such that the Fermi level is prevented from going any lower.

On the other hand, as shown earlier, hydrogen can be easily accumulated in a crystal due to a small migration barrier of 0.34 eV [30]. After penetrating into a crystal, hydrogen can occupy many interstitial sites (H_i) nearby to oxygen atoms with creating of O-H bounds, and also penetrate into oxygen vacancies (H_O). In all cases, hydrogen acts as a *shallow donor*. It is important to note that similar behaviour of hydrogen as a donor impurity appears in other oxide materials (ZnO, SnO_2, In_2O_3) and thus has some generality in these properties [10], [30]. There is some experimental support to the fact that hydrogen may be a shallow donor in β-Ga_2O_3 from experiments on its muonium counterpart and from electron paramagnetic resonance of single-crystal samples [31], [32]. Therefore, we believe that hydrogen is more preferable as a source of unintentional background n-type conductivity.

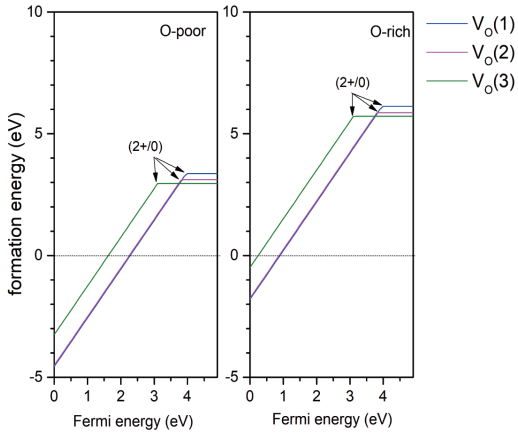

Fig. 2. Formation energies of V_O in *β*-Ga_2O_3 plotted against the Fermi energy for (a) oxygen-poor and (b) oxygen-rich conditions. For V_O, the three different vacancies are denoted $V_O(1)$, $V_O(2)$ and $V_O(3)$ as shown in Fig. 1.

5. CONCLUSIONS

In this study, we have calculated the formation energy and transition levels of oxygen vacancies in Ga_2O_3 crystal using the B3LYP hybrid exchange-correlation functional within the LCAO-DFT approach. The electronic charge redistribution in perfect Ga_2O_3 shows notable covalency of the Ga-O bonds. Formation of the oxygen vacancy in β-Ga_2O_3 leads to the presence of deep donor defects. That is why neutral oxygen vacancies can be hardly responsible for n-type conductivity in β-Ga_2O_3 accompanied by their quite high formation energy. In this respect, In this regard, we assume that the observed n-type conductivity in gallium oxide is due to the presence of interstitial and substituting hydrogen impurities in the crystal lattice.

ACKNOWLEDGEMENTS

The research has been funded by the Science Committee of the Ministry of Education and Science of the Republic of Kazakhstan (Grant No. AP08856540). J. Purans and A.I.Popov acknowledge the ERAF project 1.1.1.1/20/A/057 "Functional Ultrawide Bandgap Gallium Oxide and Zinc Gallate Thin Films and Novel Deposition Technologies".

The Institute of Solid State Physics, University of Latvia (Latvia) as the Centre of Excellence has received funding from the European Union's Horizon 2020 Framework Programme H2020-WIDESPREAD-01-2016-2017-Teaming Phase2 under grant agreement No. 739508, project CAMART2.

REFERENCES

1. Shluger, A. (2020). Defects in Oxides in Electronic Devices. *Handbook of Materials Modeling: Applications: Current and Emerging Materials*, 1013–1034.
2. Maier, J. (2003). Complex Oxides: High Temperature Defect Chemistry vs. Low Temperature Defect Chemistry. *Physical Chemistry Chemical Physics*, *5* (11), 2164–2173.
3. Lee, D., Park, J. W., Cho, N. K., Lee, J., & Kim, Y. S. (2019). Verification of Charge Transfer in Metal-Insulator-Oxide Semiconductor Diodes via Defect Engineering of Insulator. *Scientific Reports*, *9* (1), 10323.
4. Popov, A. I., Kotomin, E. A., & Maier, J. (2010). Basic Properties of the F-Type Centers in Halides, Oxides and Perovskites. *Nuclear Instruments and Methods in Physics Research Section B: Beam Interactions with Materials and Atoms*, *268* (19), 3084–3089.
5. Kozlovskiy, A., Kenzhina, I., Kaikanov, M., Stepanov, A., Shamanin, V., Zdorovets, M., & Tikhonov, A. (2018). Effect of Electronic Modification on Nanostructures Stability to Degradation. *Materials Research Express*, *5* (7), 075010.
6. Rusevich, L. L., Kotomin, E. A., Zvejnieks, G., & Popov, A. I. (2020). *Ab Initio* Calculations of Structural, Electronic and Vibrational Properties of $BaTiO_3$ and $SrTiO_3$ Perovskite Crystals with Oxygen Vacancies. *Low Temperature Physics*, *46* (12), 1185–1195.
7. Zhumatayeva, I. Z., Kenzhina, I. E., Kozlovskiy, A. L., & Zdorovets, M. V. (2020). The Study of the Prospects for the Use of $Li_{0.15}Sr_{0.85}TiO_3$ Ceramics. *Journal of Materials Science: Materials in Electronics*, *31* (9), 6764–6772.
8. Chornaja, S., Sproge, E., Dubencovs, K., Kulikova, L., Serga, V., Cvetkovs, A., & Kampars, V. (2014). Selective Oxidation of Glycerol to Glyceraldehyde over Novel Monometallic Platinum Catalysts. *Key Engineering Materials*, 604, 138–141.
9. Eglitis, R., Popov, A. I., Purans, J., & Jia, R. (2020). First Principles Hybrid Hartree-Fock-DFT Calculations of Bulk and (001) Surface F Centers in Oxide Perovskites and Alkaline-Earth Fluorides. *Low Temperature Ph*ysics, *46* (12), 1206–1212.
10. Pearton, S. J., Yang, J., Cary IV, P. H., Ren, F., Kim, J., Tadjer, M. J., & Mastro, M. A. (2018). A Review of Ga_2O_3 Materials, Processing, and Devices. *Applied Physics Reviews*, *5* (1), 011301.
11. Higashiwaki, M., Sasaki, K., Murakami, H., Kumagai, Y., Koukitu, A., Kuramata, A., ... & Yamakoshi, S. (2016). Recent Progress in Ga_2O_3 Power Devices. *Semiconductor Science and Technology*, *31* (3), 034001.

12. Luchechko, A., Vasyltsiv, V., Kostyk, L., Tsvetkova, O., & Popov, A. I. (2019). Shallow and Deep Trap Levels in X-Ray Irradiated β-Ga_2O_3: Mg. *Nuclear Instruments and Methods in Physics Research Section B: Beam Interactions with Materials and Atoms*, *441*, 12-17.
13. Drozdowski, W., Makowski, M., Witkowski, M. E., Wojtowicz, A. J., Schewski, R., Irmscher, K., & Galazka, Z. (2020). Semiconductor Scintillator Development: Pure and Doped β-Ga_2O_3. *Optical Materials*, *105*, 109856.
14. Zhao, M., Tong, R., Chen, X., Ma, T., Dai, J., Lian, J., & Ye, J. (2020). Ellipsometric Determination of Anisotropic Optical Constants of Single Phase Ga_2O_3 Thin Films in its Orthorhombic and Monoclinic Phases. *Optical Materials*, *102*, 109807.
15. Xu, C. X., Liu, H., Pan, X. H., & Ye, Z. Z. (2020). Growth and characterization of Si-doped β-Ga_2O_3 films by pulsed laser deposition. *Optical Materials*, 108, 110145.
16. Feng, B., Li, Z., Cheng, F., Xu, L., Liu, T., Huang, Z., ... & Ding, S. (2020). Investigation of β-Ga_2O_3 Film Growth Mechanism on c-Plane Sapphire Substrate by Ozone Molecular Beam Epitaxy. *Physica Status Solidi (a)*, 2000457. https://doi.org/10.1002/pssa.202000457
17. Alhalaili, B., Bunk, R. J., Mao, H., Cansizoglu, H., Vidu, R., Woodall, J., & Islam, M. S. (2020). Gallium Oxide Nanowires for UV Detection with Enhanced Growth and Material Properties. *Scientific Reports*, *10*, 21434. https://doi.org/10.1038/s41598-020-78326-x
18. Yin, W. J., Wei, S. H., Al-Jassim, M. M., & Yan, Y. (2011). Prediction of the Chemical Trends of Oxygen Vacancy Levels in Binary Metal Oxides. *Applied Physics Letters*, *99* (14), 142109.
19. Biswas, P., Ainabayev, A., Zhussupbekova, A., Jose, F., O'Connor, R., Kaisha, A., ... & Shvets, I. V. (2020). Tuning of Oxygen Vacancy-Induced Electrical Conductivity in Ti-Doped Hematite Films and its Impact on Photoelectrochemical Water Splitting. *Scientific Reports*, *10* (1), 7463. https://doi.org/10.1038/s41598-020-64231-w
20. Zacherle, T., Schmidt, P. C., & Martin, M. (2013). *Ab Initio* Calculations on the Defect Structure of β-Ga_2O_3. *Physical Review B*, *87* (23), 235206.
21. Beck, A. D. (1993). Density-Functional Thermochemistry. III. The Role of Exact Exchange. *Journal of Chemical Physics*, *98* (7), 5648–6.
22. Pandey, R., Jaffe, J. E., & Harrison, N. M. (1994). *Ab Initio* Study of High Pressure Phase Transition in GaN. *Journal of Physics and Chemistry of Solids*, *55* (11), 1357– 1361.
23. Towler, M. D., Allan, N. L., Harrison, N. M., Saunders, V. R., Mackrodt, W. C., & Apra, E. (1994). *Ab Initio* Study of MnO and NiO. *Physical Review B*, *50* (8), 5041.
24. Monkhorst, H. J., & Pack, J. D. (1976). Special Points for Brillouin-Zone Integrations. *Physical Review B*, *13* (12), 5188.
25. Mulliken, R. S. (1955). Electronic Population Analysis on LCAO–MO Molecular Wave Functions. II. Overlap Populations, Bond Orders, and Covalent Bond Energies. *Journal of Chemical Physics*, *23* (10), 1841–1846.
26. Bailey, C. L., Liborio, L., Mallia, G., Tomić, S., & Harrison, N. M. (2010). Calculating Charged Defects Using CRYSTAL. *Journal of Physics: Conference Series*, *242* (1), 012004.
27. Makov, G., & Payne, M. C. (1995). Periodic Boundary Conditions in *Ab Initio* Calculations. *Physical Review B*, *51* (7), 4014.
28. Lany, S., & Zunger, A. (2008). Assessment of Correction Methods for the Band-Gap Problem and for Finite-Size Effects in Supercell Defect Calculations: Case Studies for ZnO and GaAs. *Physical Review B*, *78* (23), 235104.
29. Scherz, U., & Scheffler, M. (1993). Density-Functional Theory of sp-Bonded Defects in III/V Semiconductors. *Semiconductors and Semimetals*, *38*, 1–58.

30. Varley, J. B., Weber, J. R., Janotti, A., & Van de Walle, C. G. (2010). Oxygen Vacancies and Donor Impurities in β-Ga_2O_3. *Applied Physics Letters*, *97* (14), 142106.

31. King, P. D. C., McKenzie, I., & Veal, A. T. (2010). Observation of Shallow-Donor Muonium in Ga_2O_3: Evidence for Hydrogen-Induced Conductivity. *Applied Physics Letters*, *96* (6), 062110.

32. King, P. D. C., & Veal, T. D. (2011). Conductivity in Transparent Oxide Semiconductors. *Journal of Physics: Condensed Matter*, *23* (33), 334214.

sciendo

LATVIAN JOURNAL OF PHYSICS
AND TECHNICAL SCIENCES
2021, N 2

DOI: 10.2478/lpts-2021-0008

BENEFITS OF ENERGY STORAGE SYSTEMS FOR SMALL-SCALE WIND FARM DEVELOPMENT IN LATVIA

E. Groza[1*], M. Balodis[2], K. Gulbis[1], J. Dirba[1]

[1] Institute of Power Engineering, Riga Technical University,
12/1 Azenes Str., Riga, LV-1048, LATVIA
[2] Research and Development Department, Latvenergo,
12 Pulkveza Brieza Str., Riga, LV-1230, LATVIA
*e-mail: Edgars.Groza@gmail.com

The paper covers the main aspects and restrictions on siting small-scale wind farms in Latvia and benefits of using energy storage systems with small-scale wind farms. The restrictions of siting have been analysed. Grid connection restrictions are addressed as the main issues for small-scale wind farm development in Latvia. Two small-scale wind farm models with similar properties have been made and analysed within the framework of the research. The paper proposes the idea for maximising the production of small-scale wind farm in a small area site with high wind potential.

Keywords: *Energy storage, wind energy, wind farm.*

1. INTRODUCTION

Nowadays renewable energy sources are more often penetrated in modern energy systems, especially wind and solar. There is a recent trend on wide deployment of distributed generation. As wind and solar power sources in their nature are stochastic, an issue on achieving a well-balanced power grid is raised. For modern power systems, the fluctuating power output can be a problem.

The placement and development of large wind farms in Latvia are strongly regulated and influenced by the government. As the modern power system is market based, wind power plants cannot rely on the government financial support. The developers must find an economically viable way for renewable development.

It is important to find a cost-effective balance to exploit small areas with high

wind potential, while maximizing possible output of wind power plant and reducing capital investment [1]. For energy storage systems (ESS), it can be a solution to maximise benefits of small wind power plants [2].

2. METHODS

The aim of this article is to propose an optimal solution to exploit small territories for wind turbines, simultaneously maximising output and optimising connection possibilities.

The main hindrance to wind farm development in Latvia is siting. Several siting restrictions have to be taken into account. The restrictions can be divided into four groups: environmental issues, grid connection issues, economic feasibility and social acceptance (Fig. 1).

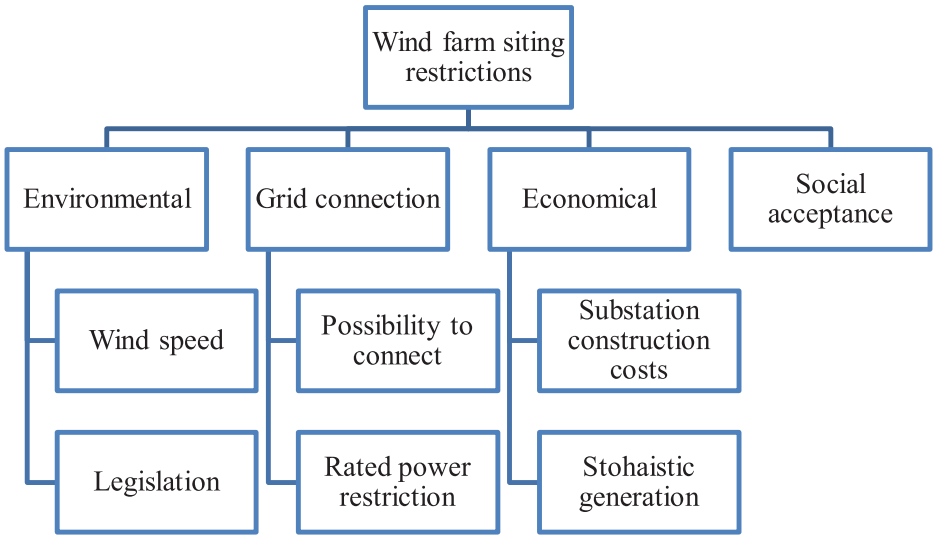

Fig. 1. Main restrictions for wind farm siting in Latvia.

Wind farm – a group of five or more wind turbines connected in a single system in which individual wind turbines are located no more than 2 km apart.

Small-scale wind farm is a group of less than five wind turbines connected in a single system in which individual wind turbines are located no more than 2 km apart.

In this paper, the economic feasibility as a siting issue is not considered, as well as social factors. Social acceptance of wind energy is an issue all over the world. The catalogue of potential solutions to overcome acceptance barriers for each country has been developed at the end of 2019 [3].

2.1. Environmental Issues

To place wind farms or few wind turbines, there are a lot of different restrictions to follow. There is a strict legislation (Cabinet Regulation No. 240 “General Rules for

Spatial Planning, Use and Construction" of 30 April 2013) that determines where a developer is not allowed to set up a large number of wind turbines in Latvia. Wind turbines are positioned no closer than three rotor diameters apart. Some restrictions for wind farms according to the Latvian legislation are as follows:

- buffer zones for wind farms around cities or villages – 2 km;
- wind farms shall be located no closer than five times the maximum height of wind turbine around residential houses in rural areas;
- wind farms shall be located no closer than 2 km from NATURA 2000 territories and micro-reserves designated for the protection of bird species, but from other NATURA 2000 territories – not closer than 500 m [4].

Due to these restrictions, there are many problems for siting wind farms. Limitations are less strict for wind power stations that are restricted to 4 wind turbines. For example, a buffer zone around cities or villages is reduced to 1 km. In Fig. 2 all the limitations, as well as state forest lands, are placed on the map of Latvia, Kurzeme region.

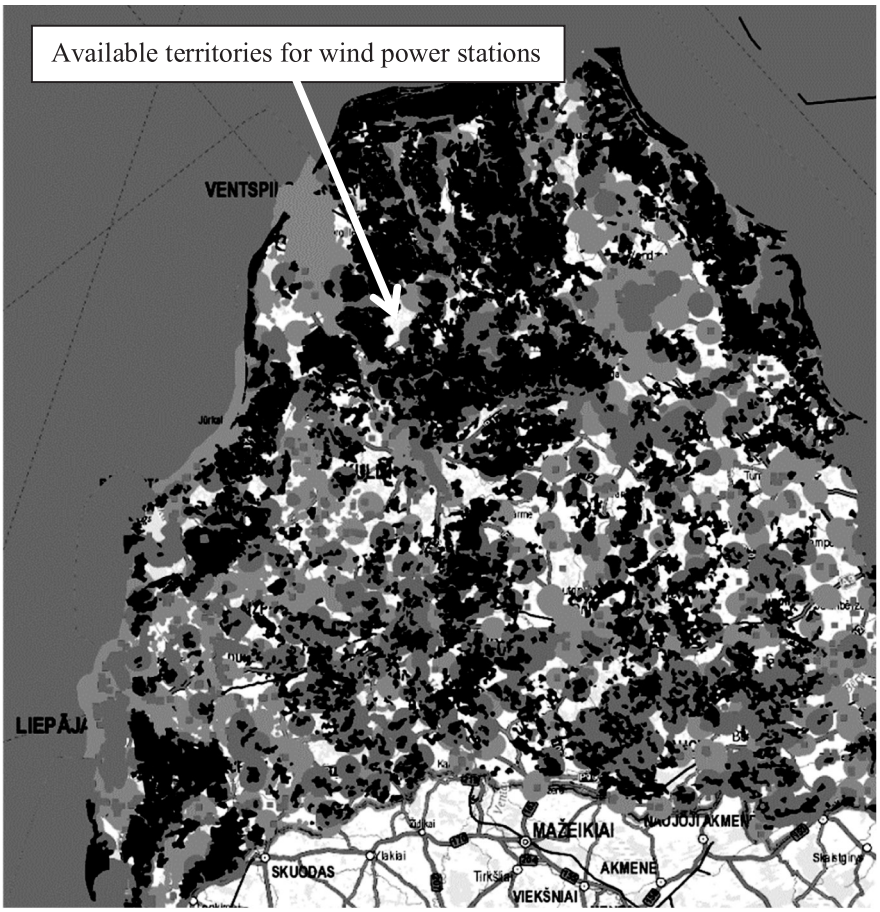

Fig. 2. Latvia, Kurzeme, different restrictions on the map.

There are some large territories where large wind farms can be built, but what cannot be seen on the map in Fig. 2 is that available territories are small. There are always some environmental risks to take into account when planning wind power plants,

for example, breeding sites of endangered bird species, feeding sites for bats. Environmental issues narrow down available areas even more. Ignoring all the different layout issues like wake losses, etc. optional area required for four turbines with a rotor diameter of 82 m is around 200 acres (around 81 ha) [5]. According to the Latvian regulation, the minimum territory should be around 48 ha. Thus, it is extremely complicated to develop wind farms and it is essential to maximise the use of the available territory.

It is important to mention that during the writing and publishing of the article, Cabinet Regulation No. 240 "General Rules for Spatial Planning, Use and Construction" has changed. Some of the restrictions have been strengthened and some have been relaxed. For example wind turbines with rated power more than 2MW must be installed no closer than 800 m from residential or public buildings. The restriction applied to Natura 2000 has been erased, although each individual case is considered separately. The decisive factor is the environmental impact assessment.

2.2. Mean Wind Speed

Latvian Environment, Geology and Meteorology Centre constantly collects wind measurement data at 10 m height. By using Hellmann exponential law (see Eq. (1)) that correlates the wind speed readings at two different heights, measurements at 10 m height are extrapolated to 100 m [6]. In the present research, Kurzeme has been chosen because the wind speed is much higher there than in other parts of the country, especially near the coastline.

$$\frac{v}{v_0} = \left(\frac{H}{H_0}\right)^{\alpha}, \tag{1}$$

where v is the speed to the height H, v_0 is the speed to the height H_0 (frequently referred to as a 10-meter height) and α is the friction coefficient or Hellman exponent.

In the research, it is important to obtain real wind measurement data. A high-quality wind speed data are crucial to project the power generation estimates and simulate the real case scenario [7].

2.3. Grid Connection Issues and Economic Feasibility

Distribution system operator (DSO) in Latvia forbids connecting a generation that is larger than 10 MW to its grid [8]. Therefore, all power stations that have large generation power must be connected to the grid of a transmission system operator (TSO). However, this connection cannot be completed with simple substation with only one transformer as illustrated in Fig. 3a. The connection to the TSO grid is possible only by completing a more complicated circuit illustrated in Fig. 3b, which is also more expensive. Building expensive substations to connect to the TSO for a small wind or solar farm may not be economically viable.

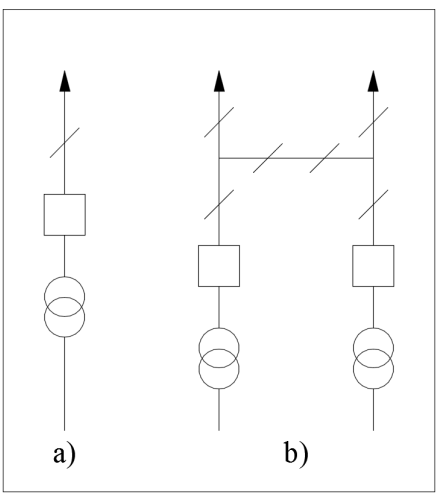

Fig. 3. Connection to TSO grid circuits [9].

Wind and solar power plant production is stochastic. The estimated installed power is not reached constantly; it is reached in peaks. Therefore, the solution is to commission more wind turbines and "dump" the excess power. Dumping the excess power limits reduces profit and increases the investment payback time.

Energy storage system (ESS) can be a solution to overcoming wind farm with rated power more than 10 MW siting restrictions. By choosing and setting up a correct ESS, it is possible to "shave" peak production power to the allowed DSO maximum by storing surplus energy in ESS and then feeding into the grid when it is most beneficial, for example, to improve wind farm production forecast, which can reach more than 50 % error of energy generation for day ahead [10] or peak shifting as the ESS is able to act as a load or generator to smooth load profile [11].

3. ANALYSIS

The wind power is proportional to the air density ρ, the intercepting area A (e.g., area of the wind turbine rotor) and the velocity V to the third power [12].

The power of an air mass that flows at speed V through area A can be calculated as follows:

$$P_W = \frac{1}{2}\rho A V^3 C_p \text{ (Watts)}, \quad (2)$$

where P_W is power of the wind, ρ is air density (kg m^{-3}), V is the wind speed (ms^{-1}), A is the area of wind turbine rotor (m^2) and C_p is the power coefficient.

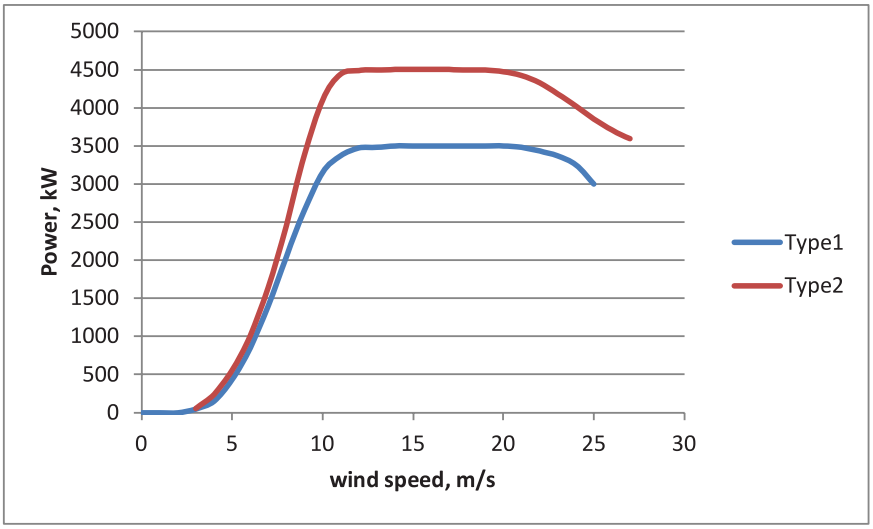

Fig. 4. Two calculated power curves of the wind turbine.

Wind data were obtained from wind farm developers who made wind measurements at the height of 40 m, 67 m and 83 m in Kurzeme – the western part of Latvia in the coastal area from 2009 to 2011 by using wind measurement masts (a common practice for acquiring accurate wind measurement data) [7], [13]. LIDAR or SODAR wind measurement devices are commonly used nowadays. Wind in this region is the highest in Latvia. These data were used to estimate power production by using two

yet similar but different turbine calculated power curves for two small scale wind power plants each containing 3 turbines.

For data analysis, the authors of the study chose a wind turbine with the rated power of 3.5 MW, rotor diameter of 138.25 m, hub height of 110 m (Type 1) and a wind turbine with the rated power of 4.5 MW, rotor diameter of 145 m and hub height of 107.5 m (Type 2). Two different layouts were examined: firstly, a wind power plant consisting of three turbines of Type 1 with the installed capacity of 10.5 MW and, secondly, a wind power plant consisting of three turbines of Type 2 with the installed capacity of 13.5 MW. Siting ignores layout issues and is designed to minimise the area used (110 to 122 ha). According to Cabinet Regulation No. 240, in Latvia a more strict regulation for siting is applied to five and more wind farms than small-scale wind farms.

The wind speed was calculated according to wind turbine hub heights using Eq. (1). To obtain reliable data, wind measurements were done for more than a year. Energy generation period of 6 months in 2009 is shown in Fig. 5. The figure shows that if the installed power of the wind farm is 13.5 MW, the wind farm produces power that exceeds 10 MW. The common method to limit the output power of the wind farm is to change a blade pitch angle [14], but the use of such a method will lead to the loss of wind farm production. Installing large-scale ESS can accumulate the excess energy and level out the system power output. In addition, the wind farm can benefit from ESS in terms of the forecast improvement service [15].

Historical data show that the capacity factor of wind farms in the Baltics is around 25 %. [16]. The efficiency of wind turbines has grown. In Fig. 6, the power output is sorted to view how much energy per year two different layouts (3x3.5 MW and 3x4.5 MW) of wind stations can generate. The first wind power plant generates around 35 GWh per year. The capacity factor of the plant is 38 %, which is reasonably high and corresponds to the manufacturer's data. The second wind power plant generates around 44 GWh per year. The capacity factor is 37 %. Due to DSO output restrictions (also shown in Fig. 5), 3.5 GWh per year will be dumped if the output power is restricted (Fig. 6 (A)).

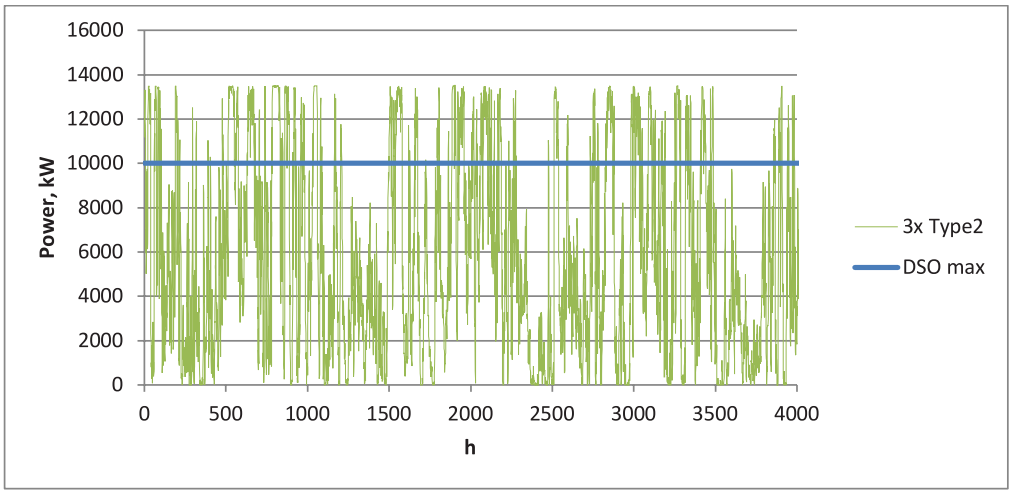

Fig. 5. The estimated production curve of the wind farm (13.5 MW).

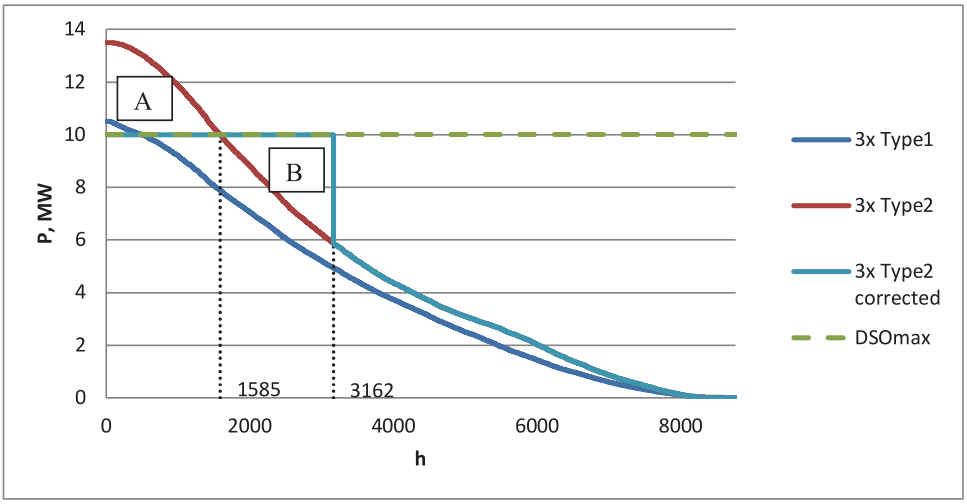

Fig. 6. The sorted production curve of the wind farm (13.5 MW).

4. CONCLUSIONS

1. According to statistics and research, ESS can be used as a solution to small wind farm development in Latvia. By overcoming DSO prohibitions of connection, the ESS allows fully exploiting small terrains for wind energy according to the Latvian legislation.
2. Using ESS to store surplus energy and feed it into the grid when the wind is low, it was possible to increase the energy output of wind turbines of the same dimensions by 20 %. The feasibility analysis should be performed to validate the long-term viability of the wind power plant.
3. As both small wind farm layouts (ignoring layout issues) with the wind turbine placement occupying the smallest possible terrain are close to 110 ha and 122 ha, it is possible to compare the potential area related gross energy yield. Using ESS and more powerful wind turbines, gross energy yield is 361 MWh/ha annually, which compared to the other layout (314 MWh/ha ann.) produces 15 % more power.
4. ESS sizing is a complex optimization task with many variables that can strongly affect successfulness of the project. To evaluate how powerful ESS should be to make the project successful and economically feasible, other studies should be performed.
5. This paper has represented an idea of ESS usage for small-scale wind farms in Latvia. The ESS selection, sizing and feasibility analysis should be performed to estimate conditions when this method is viable.

ACKNOWLEDGEMENTS

The research has been supported by the Department of Electrical Machines and Apparatus, Riga Technical University.

REFERENCES

1. Knapp, L., & Ladenburg, J. (2015). How Spatial Relationships Influence Economic Preferences for Wind Power. *A review, 8*, 6177–6201.
2. Zhao, H., Wu, Q., Hu, S., Xu, H., & Rasmussen, C.N. (2015). Review of Energy Storage System for Wind Power Integration Support. *Applied Energy, 137,* 545–553.
3. Rosaria, M., Nucci, D., Will, A., & Krug, M. (2020). *Deliverable 3.6. Catalogue of Potential Solutions to Overcome Acceptance Barriers for Each Country*.
4. Ministru kabinets. (2013). Ministru kabineta noteikumi Nr. 240. Vispārīgie teritorijas plānošanas, izmantošanas un apbūves noteikumi. *Latvijas vēstnesis, 21* (5), 41.
5. Windustry. (2008). *Community Wind Toolbox*. Minnesota.
6. Bañuelos-Ruedas, F., Ángeles Camacho, C., & Rios-Marcuello, S. (2011). Methodologies used in the extrapolation of wind speed data at different heights and its impact in the wind energy resource assessment in a region. In Gastón O. Suvire (ed.), *Wind Farm - Technical Regulations, Potential Estimation and Siting Assessment*. IntechOpen.
7. European Wind Energy Association. (2012). *Wind energy - The facts: A guide to the technology, economics and future of wind power*. London: Earthscan.
8. IEEE. (2018). *Standard for Interconnection and Interoperability of Distributed Energy Resources with Associated Electric Power Systems Interfaces*.
9. Knipšis, A. (2012). *Elektrisko pārvades tīklu elektroietaišu ekspluatācija*. Rīga.
10. Holttinen, H., Miettinen, J. & Sillanpää, S. (2013). *Wind power forecasting accuracy and uncertainty in Finland*. Espoo: VTT Technical Research Centre of Finland.
11. Awasthi, A., Karthikeyan, V., Das, V., Rajasekar, S., & Singh, A. K. (2017). Energy Storage Systems in Solar-Wind Hybrid Renewable Systems. *Green Energy and Technology,* 189–222.
12. Ackermann, T. (ed.) (2012). *Wind power in power systems* (2nd ed.). England: John Wiley & Sons, Ltd.
13. Wizelius, T. (2012). Design and Implementation of a Wind Power Project. *Comprehensive Renewable Energy,* 391–430.
14. Korchinski, W. (2012). *The limits of wind power*. Los Angeles: Reason Foundation.
15. Swierczynski, M., Teodorescu, R., Rasmussen, C. N., Rodriguez, P., & Vikelgaard, H. (2010). Overview of the energy storage systems for wind power integration enhancement. In *IEEE International Symposium on Industrial Electronics*, 4–7 July 2010, Bari, Italy.
16. Metlovs, S. (2013). *Vēja elektrostaciju, kā arī citu atjaunīgo energoresursu izmantojošo elektrostaciju jaudas regulēšanas iespēju izpēte*. Rīga: RTU.

sciendo

LATVIAN JOURNAL OF PHYSICS
AND TECHNICAL SCIENCES
2021, N 2

DOI: 10.2478/lpts-2021-0009

OPTIMIZATION OF ENERGY EXTRACTION USING DEFINITE GEOMETRY PRISMS IN AIRFLOW

I. Tipans, J. Viba, M. Irbe* and S. K. Vutukuru

Faculty of Mechanical Engineering, Transport and Aeronautics,
Riga Technical University,
6B Kipsalas Str., LV-1048, Riga, LATVIA
*e-mail: martins.irbe@rtu.lv

An approximate method for analysis and synthesis of moving rigid bodies (prisms) in the airflow without using numerical methods of space-time programming techniques is described by applying a fluid (air)–rigid solid body interaction concept for engineering applications through a straightforward mathematical model. The interaction of rigid body (prism) and air is encountered in different cases: moving body (prism) in the air; stationary bodies (prism) in the airflow; moving body (prism) in the airflow. The complicated task of rigid body (prism) and air interaction is simplified by using superposition principles, i.e., by taking into account the upstream and downstream rigid body (prism) and air interaction phenomenon, which has been found to be different under varying speeds. Numerical results obtained for various forms of prisms are shown for constant air–speed, where the steady state Reynolds-averaged Navier–Stokes (RANS) equation is solved by using k-ε realizable turbulence model. A detailed explanation to support the proposed approximate method is given by using numerical results obtained in ANSYS computations. All equations are formed based on laws of classical mechanics; the interaction of viscous forces is neglected in forming the mathematical model. Numerical results for different model prisms are compared and the theoretical results discussed in detail. The mathematical model in the present paper is applicable only to bodies that undergo a rectilinear translation motion. In the final part of the present paper, the proposed method is used in the synthesis and optimization task of energy extraction by considering the motion of a variable parameter prism in the airflow.

Keywords: *Rigid body (prisms), superposition principle, space-time programming.*

1. INTRODUCTION

The theme of the interaction between the solid (rigid) body and fluid still plays an important role in science, technology, production processes and in everyone's life.

In the present paper, three possible cases of fluid–rigid body interaction are studied: stationary rigid body in the air, non-stationary body in the air and non-stationary body in the airflow. Though good research pertaining to non-stationary rigid body–fluid interaction in fluid flows is available, no one can deny the fact that understanding the phenomena requires advanced programming skills (space–time techniques) along with in-depth knowledge of CFD and core engineering mathematics. General mesh deforming and re-meshing techniques are time consuming and strictly have geometry constrains and many times are computationally expensive. A better method compared to moving and deforming techniques with no restriction on closeness between objects and their complex motion is studied where continuity and momentum equations include motion effects [1]. Different types of mesh moving techniques for fluid–structure interaction were studied and compared. A new use of space–time discretization that could be extended for a full-time space Galerkin discretization was examined [2]. Fixed mesh technique by using arbitrary Lagrangian–Eulerian approach for flow problems in a moving domain was studied and for every time step results were displayed on a background mesh [3]–[7]. An algorithm for space–time finite element meshes was used to obtain numerical results for transient Navier–Strokes equations for an adaptive moving mesh in time [8]. New XFEM approach was proposed based on a fixed grid method, which did not take into account most of fluid unknown characteristics. This method is advantageous as simulations of deforming structures could be performed effectively [9]. Easily understandable and less complex method for space–time mesh that allows for refinement of the selected locations within the domain was also proposed [10]. Advantage of saving the computational time, accounting for flexibility of unstructured meshes and improving the scope of compressible fluid flow were mentioned in [11]. Solution for non-stationary fluid body problems by using a high-order finite element method based on space–time discontinuous Galerkin (DG) procedure was proposed and extended to explain the dynamics of parachute motion [12]. A simple method using the concept of zones, averting the space time programming techniques and extending the concept for energy extraction for simple form objects was performed in [13]. In the present study, without using any numerical space–time programming techniques and in a straightforward way using the averaged principle of superposition, fluid interaction with rigid body is explained. The entire paper specifically focuses solely on rigid body–fluid (air) interaction, does not consider flow reattachment or flow separation phenomenon and offers an alternative to a vortex induced vibration concept [14]–[16] and the same study is further extended for energy extraction by using variable parameters of definite geometry–prism. The main idea of the article is to propose a simplified approach to an interaction phenomenon and to offer an alternative to vortex induced vibration techniques through a mathematical model that does not consider the viscous effects of fluid (air) but the viscous effects are in a way indirectly resulting from the mathematical model by considering the output from steady state numerical simulations (RANS by K-ε turbulence model) in ANSYS.

2. MATHEMATICAL MODELS FOR FLUID (AIR) STRUCTURE INTERACTION

Keeping in view the much-needed tasks of analysis, synthesis and optimization that are required in many engineering applications, the present paper offers an averaged mathematical model approximately assuming a laminar flow for the incompressible fluid. However, the mathematical model does not include the viscous nature of the fluid under consideration.

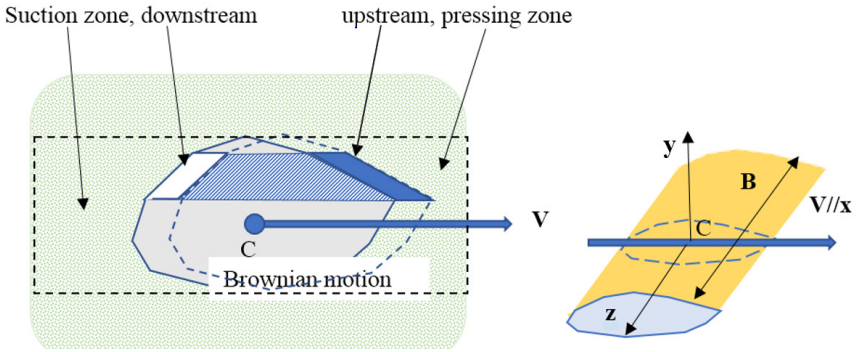

Fig. 1. External relative flow over a moving prism in very low speed airflow.

The space around the body under consideration when subjected to fluid is carefully studied; a straightforward mathematical model using classical laws of mechanics is explained based on a fluid structure interaction phenomenon.

The mathematical model is described in the case of definite geometry shaped prism (Figs. 1–3).

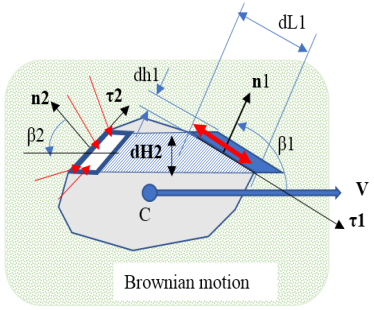

Fig. 2. Interaction of the rectilinear translation (non-rotating) motion body in windless air.

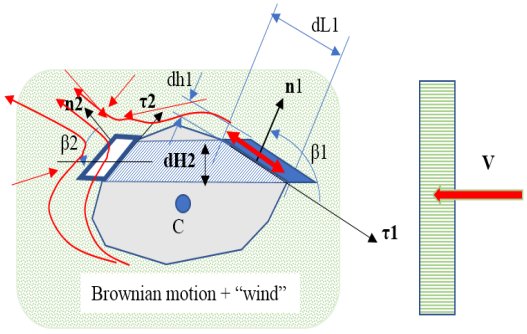

Fig. 3. Model of air interactions with stationary prism.

Considering the very small air element in the pressure zone, we use the momentum change in the differential form. According to the principle proposed in the present paper (superposition principle), taking in the projection of the area normal $n1$, before

and after collisions (fluid–body interaction), we obtain (1): from Brownian interaction to prism:

$$\begin{aligned} &m10 \cdot VB1 - (-m10 \cdot VB1) = -N1 \cdot dt, \\ &m10 = VB1 \cdot dt \cdot dL1 \cdot B \cdot \rho, \\ &p10 = \frac{|N1|}{dL1 \cdot B}, \end{aligned} \tag{1}$$

where $m10$ – Brownian interaction mass; $VB1$ – an average air normal velocity in the pressure zone; $N1$ – normal force to a small element from the air; dt – an infinitive small time interval; $dL1$ – width of a small element; B – prism height perpendicular to the plane of motion; ρ – density of air; $p10$ – atmospheric pressure in the pressure zone.

From prism air interaction at windward side (pressure side) (2):

$$\begin{aligned} &m1 \cdot v \cdot \cos(\beta 1) - 0 = -\Delta N1 \cdot dt, \\ &m1 = v \cdot \cos(\beta 1) \cdot dt \cdot dL1 \cdot B \cdot \rho, \\ &\Delta p1 = \frac{|\Delta N1|}{dL1 \cdot B}, \end{aligned} \tag{2}$$

where $m1$ – prism and air interaction boundary layer mass; v – prism velocity; $\beta 1$ – an angle between velocity v and normal $n1$; $\Delta N1$ – additional normal force acting on a prism; $\Delta p1$ – pressure increase in the pressure zone.

From the system of six equations (1), (2) it is possible to find six unknowns. The two unknowns are required to solve the following calculations:

$$p10 = 2 \cdot VB1^2 \cdot \rho \cdot dt, \tag{3}$$

$$\Delta p1 = \rho \cdot dt \cdot v^2 \cdot [\cos(\beta 1)]^2. \tag{4}$$

Accordingly, it is possible to apply equations like (1)–(4) in the suction zone (leeward side). However, the task is little complicated with the number of momentum differentials in the suction zone: it is not clear how to simplify the equations in differential form. Therefore, it is suggested to use one or the other hypothesis. Hypotheses should be tested experimentally or by using computer applications.

The first hypothesis

In the suction zone, pressure reduction $\Delta p21$ over the entire surface is constant and proportional to the square of the velocity v.

We get:

$$\Delta p21 = -\rho \cdot C1 \cdot v^2, \tag{5}$$

$$p20 = 2 \cdot VB2^2 \cdot \rho \cdot dt; \tag{6}$$

where $C1$ – a constant found according to the experimental or numerical modelling; $VB2$ – an average air normal velocity in the suction zone.

The second hypothesis

In the suction zone, pressure reduction $\Delta p22$ over the entire surface is not constant but is proportional to the square of the velocity v and also depends on the normal $n2$ to the surface area and position angle $\beta 2$. Thus, we obtain (7), (8):

$$\Delta p22 = -\rho \cdot C2 \cdot v^2 \cdot \cos(\beta 2), \tag{7}$$

$$p20 = 2 \cdot VB2^2 \cdot \rho \cdot dt, \tag{8}$$

where $C2$ is the second constant found in the same way as $C1$.

The obtained differential relationships (3)–(8) can be used in the engineering analysis and synthesis tasks in the low speed range. The prism parameters of the given configuration must be used along with the solution for the integral equations for the object surface.

For practical engineering calculations, it is recommended to adopt $VB1 = VB2$ for low velocity $v << VB1$ and $v << VB2$ ranges. Then $p01 = p02 = p0$, where $p0$ is the mean atmospheric pressure around the given prism.

3. STATIONARY BODY (PRISM) IN AIRFLOW

Looking into the interaction phenomenon of airflow with a fixed prism (Fig. 3.), it appears that the interaction process might be different, as discussed above for a rectilinear translation motion. This is because air particles have extra velocity and extra kinetic energy. However, taking the concept of interactions in relative motion, the formulas obtained previously (3)–(8) can then be used in the engineering calculations, were is air flow velocity.

4. MOVING BODY (PRISM) IN AIRFLOW

Two cases of prism motion discussed above (i.e., a rectilinear translation motion of prism in still air and a fixed prism in airflow) allow for the formulation of the interaction of a moving prism in a moving air stream (Fig. 4).

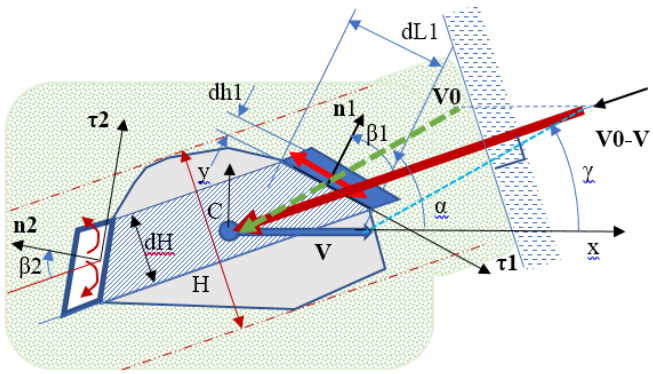

Fig. 4. Model of a moving prism in the airflow.

For this purpose, the relative motion velocity Vr vector in the pressure zone must be recalculated by determining the angle γ from the elementary parallelograms with normal directions $n1$ and $n2$ (Fig. 4). By plotting the vectors V and $V0$ on the x and y axes, we obtain (9), (10):

$$Vr = \sqrt{(-V0 \cdot \cos(\alpha) - V)^2 + (-V0 \cdot \sin(\alpha))^2}, \tag{9}$$

$$\cos(\gamma) = \frac{-V0 \cdot \cos(\alpha) - V}{\sqrt{(-V0 \cdot \cos(\alpha) - V)^2 + (-V0 \cdot \sin(\alpha))^2}}, \tag{10}$$

where Vr – a relative velocity module; $V0$ – wind velocity as a vector; V – prism rectilinear translation motion velocity as a vector and α is a $V0$ flow angle (Fig. 4).

By using the obtained relationships (3)–(8), it is possible to solve various technical tasks of fluid (air) and prism motion for engineers. For example, it is possible to carry out motion analysis tasks where airflow resistance forces can be obtained. It is even more important for solving the problems of energy extraction from a fluid (air) stream. Additionally, it is also possible to optimize the shape of the object (prism) in order to obtain the desired effect (criterion) along with motion control task optimization and real system synthesis by using mechatronic systems.

5. NUMERICAL EXPERIMENT

In the proposed airflow interaction averaging superposition method, the engineer calculations require the selection of an approximation model, which in turn requires numerical values of constants $C1$ or $C2$.

Thereby, in this direction 3D-RANS equation was solved by using K-ε realizable turbulence model. The sharp prism with two sides (other than the longest side) was 0.16 m and the depth was maintained constant at 0.16 m. In the given numerical experiment, knowing the total flow force Fx, constant $C1$ was found according to the formulas above. The numerical values of Fx and constant $C1$ are given in Figs. 5, 6.

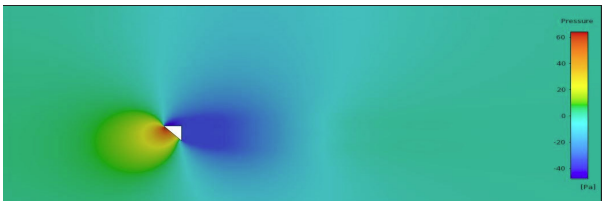

Fig. 5. Sharp right-angle Isosceles prism (angles 45° , 45°, 90°) with leading vertex 45° in stationary airflow. Quality distribution of pressure in suction and compression zones. $Fx1$ = 1.8942 N; $C1$ = 0.238.

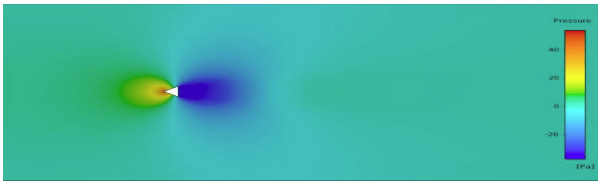

Fig. 6. Equilateral triangle (angles 60° , 60°, 60°) sharp prism in airflow with leading vertex 60°. Distribution of pressure in suction and compression zones. $Fx2$ = 1.3680 N; $C1$ = 0.245.

6. CONCLUSIONS OF THE 3D NUMERICAL SIMULATION

1. Theoretical calculations for the 2D model differ from the 3D numerical simulation.
2. Visually, the first and second hypotheses (C1, C2) come true because the pressure in the suction zone is approximately the same at all locations (Figs. 4, 5).
3. Pressure zone in different local places is different.
4. In spite of the deviations of the pressure from the constant along the edges of the pressure zone of the prism, the total force can be found according to the methodology proposed here, for a constant narrow range: $0.238 < C1 < 0.245$ (Figs. 5, 6).
5. It is known from scientific experimental studies that the difference between 3D and 2D drag coefficients is about twice. Therefore, $C \approx 0.5$ should be used in approximately 2D calculations; this value is further used in all future calculations.

7. OPTIMIZATION OF TRIANGLE PRISM IN RECTILINEAR TRANSLATION MOTION IN AIRFLOW

The motion model with given length and angles is shown in Fig. 7, where $R^{(e)}$ and $M_Z^{(e)}$ are the external forces and moment, providing a rectilinear translation motion of a triangle prism.

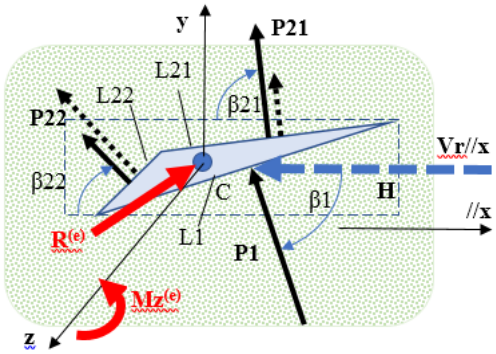

Fig. 7. Triangle prism movement in the wind direction Vr // V // x.

The optimization task should determine the prism braking velocity V that provides the maximum power in the mechatronic system. The differential equation of motion will be (11):

$$m \cdot \ddot{x} = -(V0 - V)^2 \cdot C0 + Q. \quad (11)$$

Here, $C0 = B \cdot \rho \cdot \left[(\cos(\beta 1))^3 \cdot L1 + C2 \cdot \right.$
$\left. \cdot (\cos(\beta 21))^2 \cdot L21 + C2 \cdot (\cos(\beta 22))^2 \right] \cdot L22$

where m is a prism mass; $\ddot{x}$ – constrained acceleration along x axis; Q – braking force.

The task of optimization is the following.

Given for motion parameters $C0$, m for stationary motion, when acceleration is zero ($\ddot{x} = 0$), the force Q of the prismatic braking mechatronic system shall be found to provide the maximum power P produced by the airflow force.

In the given case, without limitation, there is an optimal solution as given by (12):

$$V = \frac{V0}{3}, \quad P = \frac{4 \cdot C0 \cdot V0^3}{27}, \quad Q = \frac{4 \cdot C0 \cdot V0^3}{9}. \tag{12}$$

As can be inferred from Eq. (12), (if the flow rate $V0$ changes) the real system requires a mechatronic force control Q system.

8. MOTION OF A SHARP PRISM IN A VERTICAL PLANE

We observe the movement of a sharp prism in a vertical plane, when angles are equal $\beta 22 = \beta 21 = \beta 1$ (Fig. 8).

According to the theory of the first model mentioned above (use of a constant $C1$), the motion of a sharp prism in a vertical plane is described by differential equations (13), (14):

$$m \cdot \ddot{x} = -[\rho \cdot L \cdot B \cdot (\dot{x} \cdot \sin(\alpha) - \dot{y} \cdot \cos(\alpha))^2 \cdot (1 + C1) \cdot \sin(\alpha) \cdot sign(\dot{x} \cdot \sin(\alpha) - \dot{y} \cdot \cos(\alpha)) \cdot \sin(\alpha)], \tag{13}$$

$$m \cdot \ddot{y} = [\rho \cdot L \cdot B \cdot (\dot{x} \cdot \sin(\alpha) - \dot{y} \cdot \cos(\alpha))^2 \cdot (1 + C1) \cdot \sin(\alpha) \cdot sign(\dot{x} \cdot \sin(\alpha) - \dot{y} \cdot \cos(\alpha)) \cdot \cos(\alpha)] - m \cdot g, \tag{14}$$

where $\ddot{x}$ and $\ddot{y}$ are acceleration projections; α – an angle between normal and vertical direction; *sign* is a ±1 depending on the function in brackets; g – free fall acceleration.

The obtained equations allow solving analytical and parametric optimization problems for a given non-stationary motion case. In addition, it should be noted that this movement is close to the bird's gliding or diving movement in the air.

Example of diving motion calculation is shown below (Figs. 8–11). All parameters in system SI: $\rho = 1.25$; $L \cdot B = 0.04$; $m \cdot g = 2$; $C1 = 0.5$; $\alpha = \frac{\pi}{4}$.

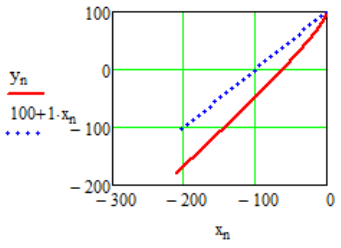

Fig. 8. The trajectory of the centre of mass motion in the vertical plane, starting from the coordinates $(x, y) = (0, +100)$.

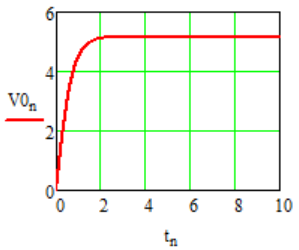

Fig. 9. Speed projection on prism normal.

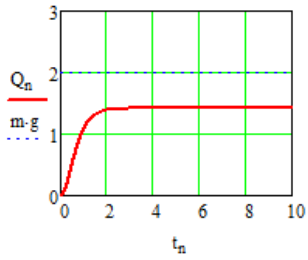

Fig. 10. Frontal force of air interaction.

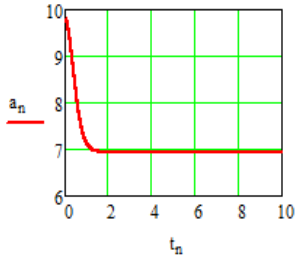

Fig. 11. Total acceleration of prism fall and lateral slip. The figure shows that the viscous forces mentioned at the beginning of the article are not taken into account.

The obtained modelling results show that the velocity projection perpendicular to the sharp prism reaches the terminal value and does not change further. However, there is no acceleration component in this direction. Accordingly, the acceleration in the tangent direction becomes constant, but the velocity component increases linearly with time. This means that in real-world applications, viscosity must be observed or a real prism with a blunt front surface must be considered.

9. SYNTHESIS AND OPTIMIZATION TASK OF ENERGY EXTRACTION

For the description of the given problem, we will use the previously obtained relation for sharp triangular prism 1, whose motion is relative to wind flow 2 (Fig. 12). The movement is along the x axis an angle α to the flow. We consider the case where the prism is attached to a base with elastic spring 3. The energy is obtained by electrodynamic braking system 4. According to expressions such as (11), the differential equation of motion is (15):

$$m \cdot \ddot{x} = -f(x) - D(\dot{x}) - A \cdot \rho \cdot (V0 \cdot \cos(\beta - \alpha) + \\ + \dot{x} \cdot \cos(\beta))^2 \cdot sign(V0 \cdot \cos(\beta - \alpha) + \dot{x} \cdot \cos(\beta)^2, \tag{15}$$

where $f(x)$ – a spring characteristic; $D(\dot{x})$ – force of an electrodynamic braking system; A – a prism area of the pressure zone, as before: $A = L \cdot B$.

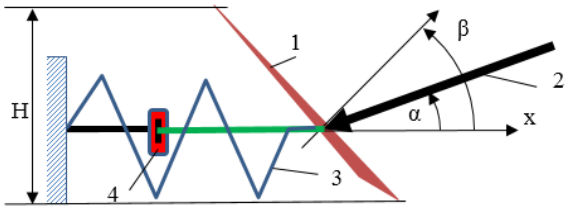

Fig. 12. Model showing the working principle for energy extraction using the phenomenon of air–body (prism) interaction with sharp triangular prism 1, wind flow 2, elastic spring 3, and electrodynamic braking system 4.

The resulting equation (15) allows solving all kinds of analytical, optimization and synthesis problems if a criterion with given constraints on system and control parameters is formulated.

As an example, we solve a synthesis problem where there can be change in area A realized by using the perforated plate. Taking into account case of linear spring with a linear electrodynamic braking system, equation (15) is expressed as (16):

$$m \cdot \ddot{x} = -c \cdot x - b(\dot{x}) \cdot \dot{x} - A(\dot{x}, x, t) \cdot \rho(V0 \cdot \cos(\beta - \alpha) + \dot{x} \cdot \cos(\beta))^2 \cdot sign(V0 \cdot \cos(\beta - \alpha) + \dot{x} \cdot \cos(\beta)^2, \quad (16)$$

where c – elasticity of spring; $b(\dot{x})$ – electrodynamic system control force; $A(\dot{x}, x, t)$ – area variation control action depending on the synthesis task of velocity, coordinate and time.

The energy optimization task should analyse the power P of the electrodynamic system (17):

$$P = d(\dot{x}) \cdot \dot{x}^2. \quad (17)$$

10. MODELLING OF VARIABLE AREA PRISM IN AIRFLOW

Let us consider the possibility of obtaining energy from the flow if the change of area occurs instantaneously when opening or closing the perforation. Let us assume the simplest direction of the wind flow parallel to the prism motion axis $\alpha = 0$ and with optimal angle $\beta = 0$ (Fig. 12). Then the differential equation of motion will be (18):

$$m \cdot \ddot{x} = -c \cdot x - b \cdot \dot{x} - (1 + C1) \cdot A \cdot (a0 - a1 \cdot sign(\dot{x} + \Delta v)) \cdot \rho(V0 + \dot{x})^2 \cdot sign(-V0 - \dot{x}), \quad (18)$$

where b, $C1$, $a0$, $a1$, Δv are constants.

Equation (18) has to be solved numerically by estimating the efficiency of energy production by criterion (17) as power.

Modelling example for a small plate is given below; all values are used in SI system. The results obtained are shown in Figs. 13–16 for parameters: m = 0.5 kg; c = 80 kg·sec^{-2}; b = 0.5 kg·sec^{-1}; $C1$ = 0.5; A = 0.04 m^2; $a0$ = 0.75; $a1$ = 0.25; Δv = 0.5 m sec^{-1}; ρ = 1.25 kg m^{-3}; $V0$ = 10 m sec^{-1}.

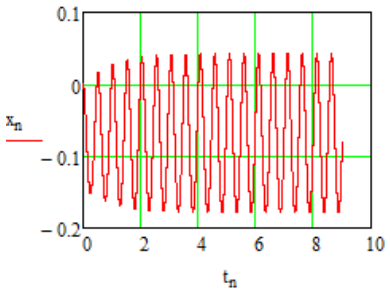

Fig. 13. Displacement with respect to time for a variable area prism.

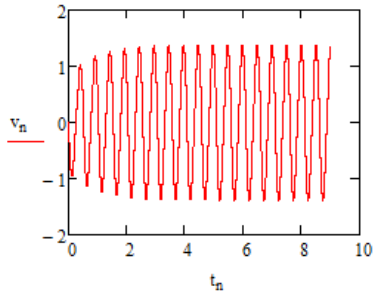

Fig. 14. Velocity with respect to time for a variable area prism.

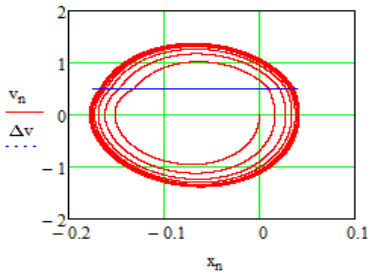

Fig. 15. Phase plane motion.

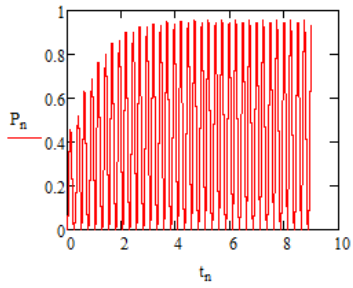

Fig. 16. Power generated for the given time interval.

From the graphs in Figs. 13–16, the following conclusions can be drawn:

1. In the aerodynamic system it is possible to initiate a stable oscillation movement by changing the interaction area of the perforated plate.
2. The opening and closing of perforations may be affected by a mechatronic system.
3. There is the second mechatronic system for generating energy, which breaks the speed of oscillation and generates power.

11. RESULTS AND DISCUSSION

Within the framework of the present study, we have developed a new method for calculating the approximate flow and rigid body interaction for: a moving body in the low speed air, a stationary body in the airflow and a moving prism in the airflow. The fluid flow is assumed to be laminar, incompressible, and viscous nature of the fluid is not taken into account for mathematical modelling, as an alternative the coefficient of interaction (constant) is introduced from numerical simulation results. Stable result in case of a variable area prism for energy extraction has been observed (see Fig. 15). Though the power obtained is small, the proposed theory (superposition principle) helps identify the cause and make a way for overall better efficiency as the nature of the proposed principle is purely mathematical and is explained in an easily understandable

and straightforward way. Good and satisfactory results are obtained both for moving prisms in the airflow and energy extraction by using a variable area prism. An alternate approach to a solid body–fluid (air) interaction phenomenon other than the traditional vortex induced vibration techniques has been found to be successful in calculating energy extraction by means of a simple mathematical model.

12. CONCLUSIONS

The method developed in the present study helps perform tasks of analysis, optimization and synthesis for the interaction of objects with fluids in a simplified way, only for rectilinear translation motion of body. The proposed techniques help overcome the extensive space–time programming methods. The analysis, optimization and computer modelling examples discussed in this paper illustrate the effectiveness of the proposed method in engineering calculations.

The present study also establishes the fact that there is an alternate approach to vortex induced vibration phenomenon for the energy extraction process considering just the body–fluid interaction coefficient in a straightforward mathematical model. The theory can be extended to any complex body–fluid interaction as the work is purely mathematical in nature.

ACKNOWLEDGEMENTS

This research has been funded by the Latvian Council of Science, project "Creation of Design of Experiments and Metamodelling Methods for Optimization of Dynamics of Multibody 3D Systems Interacting with Bulk Solids and Fluids", project No. Lzp-2018/2-0281 and supported by the Doctoral Grant programme of Riga Technical University.

REFERENCES

1. Wei, G. (2005). A Fixed-Mesh Method for General Moving Objects in Fluid Flow. *International Journal of Modern Physics B,* 19 (28), 1719–1722.
2. Wick, T. (2011). Fluid-Structure Interactions Using Different Mesh Motion Techniques. *Journal of Computers and Structures*, *89* (13), 1456–1467.
3. Codina, R., Houzeaux, G., Coppola-Owen, H., & Baiges, J. (2009). The Fixed-Mesh ALE Approach for the Numerical Approximation of Flows in Moving Domains. *Journal of Computational Physics, 228* (5), 1591–1611.
4. Tezduyar, T. E., Sathe, S., Keedy, R., & Stein, K. (2006). Space-Time Finite Element Techniques for Computation of Fluid-Structure Interactions. *Comput. Methods Appl. Mech. Eng*., *195*, 2002–2027.
5. Tezduyar, T. E., & Sathe, S. (2007). Modelling of Fluid-Structure Interaction with the Spacetime Finite Elements: Solution Techniques. *Int. J. Numer. Meth. Fluids*, *54*, 855–900.
6. Han, D., Liu, G. R., & Abdallah, S. (2020). An Eulerian-Lagrangian-Lagrangian Method for 2D Fluid-Structure Interaction Problem with a Thin Flexible Structure Immersed in Fluids. *Computers & Structures, 228*, 106179.

7. Takizawa, K, & Tezduyar, T. E. (2011). Multiscale Space-Time Fluid-Structure Interaction Techniques. *Comput. Mech., 48*, 247–267.
8. Neumuller, M., & Steinbach, O. (2011). Refinement of Flexible Space-Time Finite Element Meshes and Discontinuous Galerkin Methods. *Computing and Visualization in Science, 14*, 189–205.
9. Gerstenberger, A., & Wall, W. A. (2006). An Extended Finite Element Method Based Approach for Large Deformation Fluid-Structure Interaction. *European Conference on Computational Fluid Dynamics*. ECCOMAS CFD, Netherlands, TU Delf.
10. Behr, M. (2008). Simplex Space-Time Meshes in Finite Element Simulations. *International Journal for Numerical Methods in Fluids, 57* (9), 1421–1434.
11. Danwitz, M. V., Karyofylli, V., Hoster, N., & Behr, M. (2019). Simplex Space-Time Meshes in Compressible Flow Simulations. *International Journal for Numerical Methods in Fluids*, *91* (1), 29–48.
12. Diosady, L.T., Murman, S.M., & Carton de Wiart, C. (2018). A higher order space time finite element method for moving body and fluid structure interaction problem. In *10th International Conference on Computational Fluid Dynamics (ICCFD10)* (pp. 1–16), 9–13 July 2018, Barcelona, Spain.
13. Tipans, I., Viba, J., Irbe, M., & Vutukuru, S. K. (2019). Analysis of Non-Stationary Flow Interaction with Simple Form Objects. *Agronomy Research, 17* (1), 1227–1234.
14. Barrero-Gil, A., Pindado, S., & Avila, S. (2012). Extracting Energy from Vortex-Induced Vibrations. A Parametric Study. *Applied Mathematical Modelling, 36* (7), 3153–3160.
15. Bearman, P.W. (1984). Vortex Shedding from Oscillating Bluff Bodies. *Fluid Mech., 16*, 195–222.
16. Chin, D. D., & Lentink, D. (2016). Flapping Wing Aerodynamics: From Insects to Vertebrates. *J. Exp. Biol., 219*, 920–932.

sciendo

LATVIAN JOURNAL OF PHYSICS
AND TECHNICAL SCIENCES
2021, N 2

DOI: 10.2478/lpts-2021-0010

POTENTIAL OF END-USER ELECTRICITY PEAK LOAD SHIFT IN LATVIA

K. Lebedeva[1*], A. Borodinecs[1], A. Krumins[2],
A. Tamane[1] and E. Dzelzitis[1]

[1] Riga Technical University,
Department of Heat Engineering and Technology
6 Kipsalas Str., Riga, LV-1048, LATVIA
[2] Lafivents Ltd, 58 Bauskas Str., Riga, LV-1004, LATVIA
*e-mail: kristina.lebedeva@rtu.lv

One of the main challenges in the world as well as in Latvia is the reduction of the fossil fuel consumption. Electricity generation, which is still mainly produced by fossil fuel or nuclear power, is one of the largest shares. Nowadays end-users can efficiently control their electricity consumption by shifting electrical loads and taking into account fluctuating electricity price at Nord Pool. The smart metering systems have been expanding, but for the time being, end-users do not use this possibility efficiently.

This study provides an analysis of Latvian electricity consumption specifics and evaluates a potential to shift electricity peak loads. The study includes households, industry and commercial/public sector. Based on the questionnaire distributed among end-users, the initial data on equipment and usage profile were collected. The most essential equipment was reviewed to estimate the potential for load shift. The obtained results show that that there is a positive effect of the load shift. In the household sector, the average electrical load shift can be 6 % (95 GWh/year) during a period at a cheaper price; in the industry sector on average 37 % (36.58 GWh/year) and in the commercial/public sector there is no potential due to its specifics (working hours, constant use of refrigerators, etc.).

Key words: *Demand side management, electricity consumption of the energy sector, electricity peak, peak load shift, user behaviour.*

1. INTRODUCTION

According to the EUROSTAT report "Electricity Production, Consumption and Market Overview", total net electricity generation in the EU was 2 806 TWh in 2018. It was similar to the year before, following an increasing trend during several years before 2017. 45.5 % of the net electricity generated in the EU in 2018 came from fossil fuels (such as natural gas, coal and oil), while 25.8 % came from nuclear power stations. Among the renewable energy sources the highest share of net electricity generation in 2018 was from hydropower plants (13.0 %), followed by wind turbines (11.3 %) and solar power (4.1 %) [1].

To achieve the Energy Union energy efficiency goals, Latvia has developed the National Energy and Climate Plan of Latvia 2021–2030 [2]. This plan respects the EU targets:

- commitments for 2030 made within the Paris Agreement under the UN Framework Convention on Climate Change regarding climate change mitigation – reduction of GHG emissions and greater CO_2 sequestration in all sectors – to reduce the total EU GHG emissions by at least 40 % compared to 1990 by 2030 in a cost-effective way;
- the EU Roadmap for Moving to a Competitive Low Carbon Economy in 2050 [3] – the EU is committed to achieving an internal reduction of EU Member State emissions by 80–95 % by 2050 compared to 1990 levels in order to be a competitive economy with low carbon dioxide emissions.

In order to ensure the growth of the national economy, the demand for electricity continues to grow. According to the Central Statistical Bureau (CSB), it increased by 3% between 2015 and 2018, and in 2018 approximately 47 % of electricity was generated using fossil fuels; notably, this year growth contributed to a 1.7 % increase in global energy-related CO_2 emissions [4].

Meeting peak demand is one of the reasons for the growing emissions from electricity generation. The peak electricity needs are usually met by base-generating loads powered by fossil fuels (natural gas, oil, etc.), so peak hours are more carbon intensive than off-peak hours. The concept of demand side management (DSM) emerged after the energy crisis. It employs solutions such as reducing the daily peak load [5], which indicates the need to shift or reduce electricity demand during peak hours. Demand side management has proven to be one of the most promising peak reducing strategies, due to the fact that DSM requires the latest technologies such as smart grids, including smart meters to improve efficiency [6], [7].

To increase the potential for demand side flexibility, a deeper understanding of domestic electricity load profiles is needed [8], [9]. As results of [10] show, the household electricity sector is changing with increasing integration of PV, smart meters, two-way communication between the customer and the utility, dynamic pricing, and can effectively shift the residential peak away from the time of overall electricity system peak load. However, the research of new decentralized energy production systems (PV, micro wind turbines etc. – electrical power < 5 kW) and the building requires precise knowledge of electricity demand generation. Demand response provides the largest benefits to systems with high renewable energy penetration [11]. A tool developed in [12] gives a load profile for each device and will be used to optimise the

microgeneration system management strategy to increase electrical self-sufficiency and self-consumption. The advancements in smart-metering technology, Internet of Things, information and communication technology (ICT) for household electricity management, and energy efficiency programs may allow consumers to play an active role as providers of demand-side flexibility and thus help to balance the grid and contribute to a secure and sustainable electricity supply [6].

Many industries have great potential for demand-side management, but their accounting in energy system analysis and modelling is limited by the availability of demand data, which are usually confidential [13]. In Germany, opportunities to sell flexible industrial capacity already exist in the form of balancing the energy market – the participation as secondary and tertiary reserve is generally suitable for industry [14]. The main potential suppliers of flexible electricity capacities are energy-intensive companies. However, non-energy-intensive consumers, such as commercial companies and public sector organisations, are also expected to provide flexibility to the system [15].

The paper presents a study on the potential of the possible shift of electricity load from peak to off-peak times in the Latvian energy sectors: households, industry and commercial/public.

2. MATERIALS AND METHODS

The analysis of the Latvian electricity market is based on the data of AS Augstsprieguma tikls (AST) (*independent high voltage power transmission and servicing in the Republic of Latvia*) and AS Sadales tikli (ST) (*Sadales tikls AS is the maintainer and developer of the electricity network in Latvia*). Data from the Central Statistical Bureau of Latvia and Nord Pool were also used to obtain the information on price fluctuation during the year.

The net electricity consumption in Latvia made up to the total of 7.3 TWh (in 2019), an average Nord Pool day-ahead price for the Latvian bidding area decreased to 46.28 EUR/MWh [16]. Local generation covered 84.7 % (in 2019) of the national consumption.

Figure 1 presents data on electricity consumption for the period of 2015–2018. The electricity consumption of the industrial and commercial/public sectors increased, but not significantly, and in the household sector there was a slight decline in consumption.

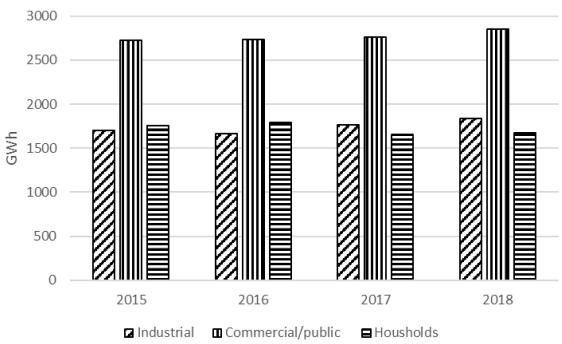

Fig. 1. Electricity consumption of household, commercial/public and industry sectors in 2015-2018.

In this study, public buildings were divided into groups based on the Real Estate State Cadaster Information System (RESCIS) and CSB division (see Table 1).

Table 1. Division of Public Buildings

Non-residential buildings	2018	
	Number, thous.	Area, mil. m^2
Hotels and similar buildings	5.622	2.68
Office buildings	7.101	6.42
Wholesale and retail trade buildings	8.099	4.33
Public entertainment, education, hospital or institutional care buildings	6.386	9.55
Other non-residential buildings	1.635	1.49

2.1. Analysis of the Latvian Household Electricity Consumption

The household sector is a key sector in the current energy grid in the European Union (EU). Electricity consumption in this sector amounts to 29 % of total consumption [17]. In Latvia, this percentage is slightly lower – it is about 25–26% of the total electricity consumption. As mentioned above, there has been a slight reduction in the electricity consumption of the household sector since 2015. This reduction can be explained by the improved energy efficiency of electric appliances and by the fact that since 2010 the number of the population has dropped by 200 000 reaching 1 million 920 thousand at the beginning of 2019 [18].

EUROSTAT data during the period of 10 years (2007–2017) show that EU-28 electricity consumption in the household sector increased by 0.1 %. Despite the great progress made in household appliances and light energy efficiency, the upward trend is mainly determined by the increase in the number of households, as well as in the number of household appliances.

Results of the Survey of Consumption of Electricity in Households conducted by the CSB and EUROSTAT show that for cooking households mainly consumed electricity (32.7 % of all households surveyed), natural gas (29.7 %) or liquefied petroleum gas (LPG) (24.1 %). Only small share of households (13.5 %) used firewood for cooking.

The survey data show that the household in Latvia on average consisted of 2.4 persons and the average heated floor space thereof comprised 69 m^2. One household on average consumed 182 kWh of electricity per month in 2015 and 189 kWh in 2018.

The analysis of the municipality electricity consumption revealed that the largest electricity consumption was observed in Riga and Riga region in 2018. Households in Riga consumed more than 40 % of all electricity consumed in the country. After analysing the data on the average electricity consumption per household in the municipalities, it has been concluded that, for example, one household in Garkalne and Babīte counties consumed almost 2.5 times more electricity per year than an average household in the country. Each Latvian region has very different electricity consumption per household and it is more dependent on population density. It

very much depends on the type of heating, outdoor lighting, operation of different water pumps and other appliances in private houses.

2.2. Analysis of Latvian Industry Electricity Consumption

In 2018, the largest consumers of energy resources in Latvia were the transport sector which accounted for 30.1 % of the total energy consumption, households – 28.8 % and industry – 22.9 %. Compared to 2017, a rise in the final energy consumption was recorded in the transport sector (3.7 %), industry (14.4 %), and households (3.1 %), while a decline in agriculture and forestry (3.8 %) as well as amount consumed by other consumers (3.4 %) was observed in 2018 [18].

According to the CSB data, the largest consumption of electricity in the industry sector was recorded in the "manufacturing of wood, wood products and cork, except for furniture; in the manufacturing of straw articles and plaiting materials" – 807 GWh. The second largest consumer was the sector of "food products, beverages and tobacco" – 284 GWh, which was followed by the "manufacturing of other non-metallic mineral products" – 281 GWh in 2018. From 2015 to 2018, electricity consumption in industry increased by 7.6 %, reaching 1842 GWh in 2018. The greatest consumption of electricity was recorded in the sector of wood, wood products and cork manufacturing – 43.8 % of the final electricity consumption in the industry.

To perform the analysis of electricity consumption of the Latvian industry sector and to optimise manufacturing companies' specific equipment performance with an aim to balance the energy demand during peak hours, the calculations were made using final average electricity consumption per hour by the industry sector in 2018.

2.3. Analysis of Latvian Commercial/Public Sector Electricity Consumption

The largest electricity consumers in Latvia are commercial and public sectors where notable changes were not recorded in the final electricity consumption from 2015 to 2018 (see Fig. 1). The analysis of electricity consumption of commercial and public sectors by months shows that a majority of seasonal changes directly depend on the duration of light time (longer during winter and autumn season), the use of electric heating devices and also possibly summer holidays in educational institutions.

Compared to 2017 (2764.7 GWh), (2856.4 GWh) the Latvian final electricity consumption of the commercial and public sectors increased by 3.2 % in 2018, which was due to the commissioning of new office buildings, as well as opening of 15 co-production offices and expansion of retail premises in 2018 [19].

3. RESULTS

3.1. Households

In order to assess the flexible loads for shifting in the Latvian *household sector*, an in-depth survey of six households was carried out: four apartments and two single family houses.

Household No. 1 (HH1) – 4 people (2

adults, 2 children): 3-room apartment, 75 m^2, the average electricity consumption in winter is 279 kWh/month, in spring – 248 kWh/month, in summer – 247 kWh/month, in autumn – 254 kWh/month; electricity consumption differs between weekdays and weekends. *Household No. 2 (HH2) – 2 people (2 adults – young family)*: 2-room apartment, 42 m^2, the average electricity consumption in winter is 80 kWh/month, in spring – 66 kWh/month, in summer – 64 kWh/month, in autumn – 77 kWh/month; electricity consumption differs between weekdays and weekends. H*ousehold No. 3 (HH3) – 2 people (2 adults – seniors)*: 2-room apartment, 37 m^2, the average electricity consumption in winter is 41 kWh/month, in spring – 38 kWh/month, in summer – 19 kWh/month (pensioners are in the summer house for almost the entire summer period), in autumn – 40 kWh/month. H*ousehold No. 4 (HH4) – 2 people (2 adults – young family):* 2-room apartment, 50 m^2, the average electricity consumption in winter is 108 kWh/month, in spring – 98 kWh/month, in summer – 78 kWh/month, in autumn – 109 kWh/month; electricity consumption differs between weekdays and weekends.

Single-family house No. 1 (HP1) – 4 people (2 adults, 2 children): 2-floors, 120 m^2, the average electricity consumption in winter is 399 kWh/month, in spring – 441 kWh/month, in summer – 365 kWh/month, in autumn – 367 kWh/month; electricity consumption differs between weekdays and weekends. The small difference in electricity consumption in the summer and winter period is due to the use of electricity in the spring/summer for gardening (watering) and the filling and cleaning of the pool, while the use of warm floors in the winter smoothest it out. *Single-family house No. 2* (HP2) – 4 people (2 adults 2 children): 2-floors, 172 m^2, the average electricity consumption in winter is 344 kWh/month, in spring – 344 kWh/month, in summer – 352 kWh/month, in autumn – 365 kWh/month; electricity consumption differs between weekdays and weekends. The small difference in electricity consumption in the summer and winter period is due to the use of electricity in the summer for gardening (watering), while the use of ground heat pump in the winter/autumn smoothest it out.

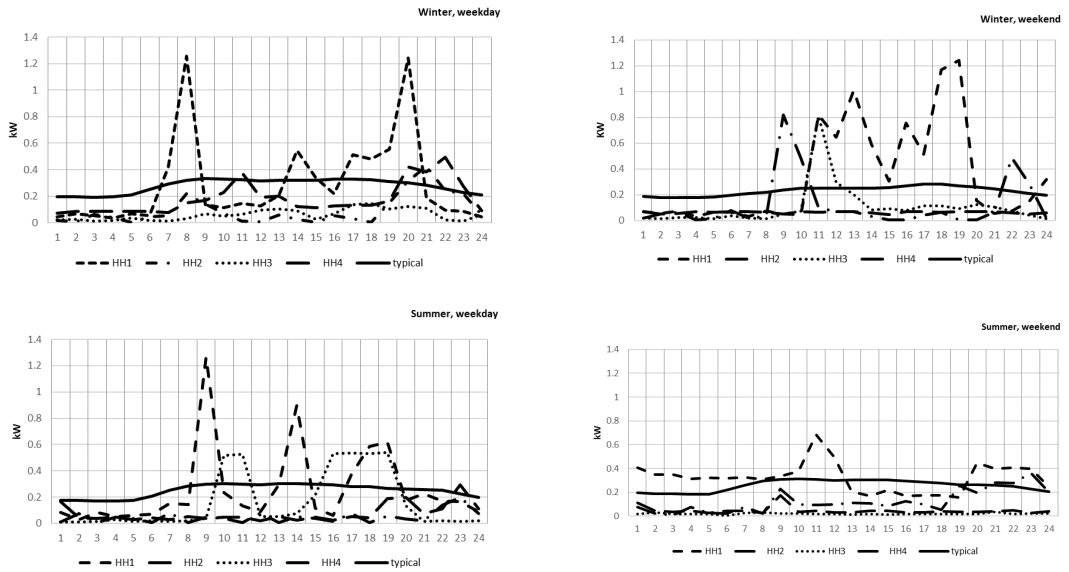

Fig. 2. Electricity consumption of the analysed households (flats) compared to the Latvian typical daily curve.

In order to analyse the difference of the peak loads for each household, the electricity consumption load graphs for all surveyed households for the standard winter weekday and weekends, as well as the standard summer weekday and weekends were compared with a standard Latvian daily electricity consumption curve ("typical" – curve in the graph) (see Fig. 2). A typical load distribution curve calculation is based on the percentage distribution of the total daily electricity consumption using Nord Pool data.

Figure 2 shows that the electricity consumption curves of households only partially correspond to the typical electricity consumption curve in Latvia. Typical electricity consumption curve in Latvia increases from 6:00 to 9:00 and from 16:30 to 18:00 in winter and all consumption curves show higher peaks during winter evenings. Morning peaks of the weekend fall in the later hours of the morning than on weekdays. Typical peak consumption in Latvia increases from 5:30 to 9:00 in summer. Morning peaks of the weekend fall in the later hours of the morning than on weekdays.

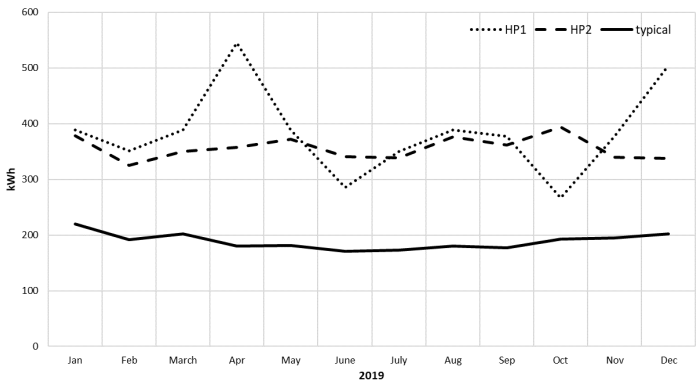

Fig. 3. Electricity consumption of the analysed households (single family houses) compared to the Latvian typical yearly curve.

Figure 3 shows that the electricity consumption curves of households only partially correspond to the typical electricity consumption curve in Latvia. The curves show the peaks of electricity consumption in spring and summer time due to the use of electricity for gardening (watering) and the filling and cleaning of the pool. Figure 3 shows the peaks of electricity consumption of HP1 in winter which is due to the start of the cold weather and intensive use of electric floor heating.

Detailed hourly/monthly data from the smart meter for the period of 2019–2020 were obtained and used for the analysis. The survey was carried out for the analysis of the household electricity consumption in order to perform demand-side management for the shift of flexible workloads in the first household. Household characteristics: data about family members; number, type, power of electrical appliances; time of use, usage frequency, and daily usage of appliances. A special questionnaire was developed for households and the respondents completed it.

All households use a washing machine once a week, except for HH1, HP1 and HP2 – twice a week. A dishwasher is used by HH1 (it is suitable for 4-person household) almost every day, twice a day on working days, and every weekend three times a day.

Since the objective of our study was to evaluate the possibility to shift electrical load from peak time to off-peak time, it was found that two household appliances – washing machine and dishwashers – were suitable for reducing loads because other power-consuming devices could not be used at other times for their intended purpose. Another option to shift electrical load from peak time to off-peak time in private house households is to turn on the garden watering system at night time.

If the whole Latvian household sector shifts washing machine load, it is calculated that an average electricity consumption decreases till 43 GWh/year and for dish washer – 31 GWh/year. Calculation showed that electricity consumption for garden watering systems based on average consumption from June to September was about 21 GWh/year. It is a very approximate calculation since the observed households have one water pump and there is no separate meter for consumed water for garden needs.

3.2. Industry Sector

In order to assess the flexible load transfer in the Latvian *industry sector*, an in-depth survey of three companies was carried out:

- fruit and vegetable processing and preserving company;
- confectionery company;
- underwear manufacturing company.

The paper presents calculations of the potential for demand side management to reduce peak loads for two *enterprises specialising in food product manufacturing: confectionery company and fruit and vegetable processing and preserving company*. The analysis was performed for 2018 and 2019. In order to analyse electricity consumption of the group of enterprises, the specific equipment was determined, as well as questionnaires for power and operating time schedules were developed.

Curve of the Latvian daily electricity consumption by industry sector is shown in Fig. 4. Calculations of the load distribution curve in the industry sector are based on the percentage distribution of the total daily electricity consumption using CSB, EUROSTAT and Nord Pool data. In order to analyse the difference of the peak loads for food product manufacturing company, the average hourly electricity consumption schedule for all analysed companies in 2018 and load graphs were compared with a standard hourly electricity consumption curve of the Latvian industry sector.

Fig. 4. Average hourly electricity consumption in 2018.

Figure 4 shows that the electricity consumption curves of the analysed companies only partially correspond to the electricity consumption curve of the Latvian industry sector. Peak consumption of the Latvian industry sector increases from 5:00 to 10:00, from 12:00 to 13:00 and from 14:00 to 15:00. For the confectionery company, the curve corresponds more to the curve of the industry sector because the company works in two shifts and powerful production lines shut down early in the morning, as well as product cooling tunnels are turned on two to four times a day because the direct gas fire oven is used for product baking. It can be one of the options how to optimise the operating time of powerful production lines (for example, hard and soft biscuit lines) and cooling tunnels in order to balance energy demand during peak hours. Let us assume that all manufacturing companies working in the confectionery sphere (60 companies) may choose to shift their powerful production lines to the early hours of the morning in case of load transfer.

After the analysis of the available data, it was calculated that in case of the load shift of powerful production lines of confectionery companies an average electricity consumption for load shift could be 36.58 GWh/year.

In order to assess the flexible load transfer in the Latvian *commercial/public sector*, an in-depth survey of two office buildings and one shopping mall was carried out. The analysis of impact of time schedule optimization and demand side management of electrical appliances on energy demand was performed in public buildings (office buildings and retail trade buildings).

The analysis was carried out on the basis of the available data on the electricity consumption of *two office buildings*. One building is *a state institution* that works only 5 days a week (only working days) and 8 hours a day and another *office building rents out premises to 31 companies*, some of them work in 2 shifts. The analysis of wholesale and retail trade buildings was carried out on the basis of the available data on the electricity consumption of an average *shopping mall* (~ 5000 m^2) with a supermarket (food etc.) that includes a warehouse. A mall offers a range of industrial goods, clothing, household, perfumery stores, as well as small businesses that offer services, e.g., hairdressing salons, cafes, key production, etc. The working time of a shopping mall is 8:00–22:00. In order to analyse electricity consumption of the office buildings, equipment, power and operating time schedules were determined.

To be able to compare the daily electricity consumption of office buildings and retail trade buildings, an average consumption of the buildings in question was obtained. After examination of the office and retail market overviews of the largest Latvian real estate companies (Latio, Arco Real Estate, Ober-Haus Real Estate Advisors) it was concluded that Latvia had 0.67 square meters of office space per capita (2017 data) and the average retail space per capita was 1.07 m^2 in Latvia.

To compare the daily average electricity consumption per hour by all Latvian office buildings and retail trade buildings with the final average electricity consumption per hour by the Latvian commercial and public sector, some assumptions were made based on the analysis of the following information: CSB data on the population (at the beginning of 2018 there were 1 934 379 people), RESCIS data on the number and area of office buildings and data about standard shopping centre (5000 m^2) classification of commercial property – retail formats for Latvia [20]. Calculation of the Latvian daily electricity consumption by the commercial and public sector is based

on the percentage distribution of the total daily electricity consumption using CSB, EUROSTAT and Nord Pool data.

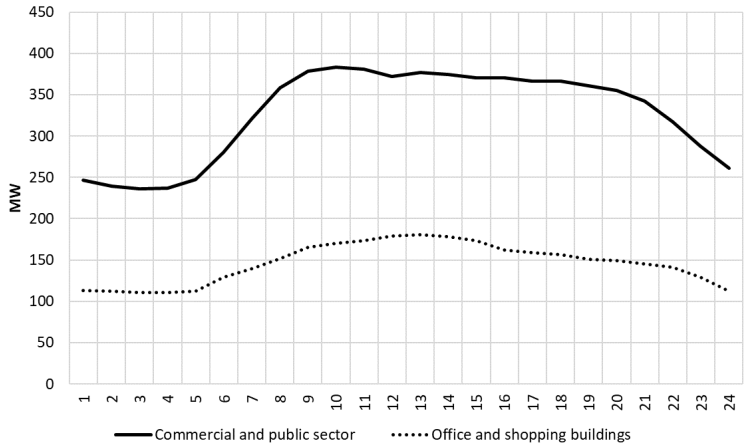

Fig. 5. Daily average electricity consumption by office and shopping buildings compared to the commercial and public sector in 2018.

Figure 5 shows that the electricity consumption curve of the analysed buildings in the commercial and public sector only partially corresponds to the electricity consumption curve of this sector. Peak consumption of the Latvian commercial and public sector increases from 5:00 to 10:00 and lasts till 20:00 due to the work of educational institutions at this time, the reception time in clinics and the conduct of most of the examinations in hospitals etc.

After the analysis of the available information, it was concluded that the largest consumers of electricity in office buildings were microclimate and comfort equipment (ventilation and cooling equipment). The largest consumers in retail trade buildings were storage equipment (showcases, refrigerators etc.), as well as ventilation and cooling equipment.

Analysing the research and tests regarding microclimate in non-residential buildings conducted by researchers of RTU Department of Heat Engineering and Technology [21], [22], it is assumed that a ventilation machine works 24 hours a day during the winter (3 months), and 16 hours a day during other seasons – 6560 hours per year; air-conditioning works during the summer for an average of 14 hours a day during 3 months or 1260 hours per year. Such an operation can be suitable for retail trade buildings, office buildings and hospitals, for educational institutions operating hours per year can be lower. These power loads can be transferred to night hours through the use of stored energy not directly from the network in order to balance energy demand during peak hours. If we assume that 20 % of all office buildings and wholesale and retail trade buildings use this type of ventilation machine and air-conditioner to operate electricity from energy storage systems, an average electricity consumption for load transfer can be 897.4 GWh/year in case of load transfer from peak hours.

4. CONCLUSIONS

According to the "Annual Statement of Transmission System Operator for the Year 2018", it is expected that the share of large, conventional generating capacity will decrease in the coming years, but the role of small, decentralised generation and active consumers will increase. It is necessary to introduce a national electricity data exchange platform in Latvia in order to promote the digitization of the electricity system and to ensure the involvement of decentralised generation and active consumers in balancing the electricity system and ensuring reserves.

The study concludes that the Latvian energy sectors, households, industry, and commercial/public sector have the potential to transfer load shift from peak time to off-peak time.

In the household sector (flats), two household appliances – washing machine and dishwasher – are suitable for reducing loads because other power-consuming devices cannot be used at other times for their intended purpose. For private houses, electricity demand for garden watering systems can be transferred to night (off-peak) time. Factors that will contribute to the maximum ability to reduce loads are highly dependent on change in the user behaviour, flexibility in the use of electrical appliances and users' willingness to use electrical appliances not according to their preferences, but depending on electricity demand management for reduction of peak loads. Taking into account the desire of the population to use more energy efficient household appliances and to follow a "greener" lifestyle, the household sector shows significant new achievements. All such activities in the long-term are important for making a good consumption forecast, increasing the use of more efficient equipment in order to reduce consumption, and promoting the use of smart meters to expand knowledge of new demand side management strategies in electrical networks.

The industry sector also has the potential for shifting loads, but in this case, it is entirely up to the owners of the companies. This requires a more accurate calculation from an economic point of view, whether it will be profitable in financial terms for the company to shift the load to the night time and pay workers nightly rates in accordance with the Latvian legislation.

Consequently, in the commercial/public sector there is no potential of load transfer due to the fact that public buildings mostly work during the day and this is the time when it is necessary to maintain a favourable climate; therefore, the load shifting is possible only if the air is prepared at night (cooled or heated), stored and returned to the building during the day. This opportunity may be considered in the next study. It can be one of the options how to optimise the operating time of powerful ventilation and cooling equipment in order to balance energy demand during peak hours.

The aim of these optimization actions is to change the characteristics of electricity consumption taking into account the overall consumption picture, the time profile of consumption, the contractual supply parameters in order to achieve savings on electricity costs.

The results of the study are highly dependent on the input data. In the course of this study, the main shortcomings were related to electricity consumption data unavailability by energy sectors (households, industry and commercial/public sector). Statistics and smart meter data were

used as more accurate data (information on the electrical equipment used by manufacturers, on various technological solutions etc.). Energy consumption data for industry and commercial/public energy sectors are protected by Article 19 of the Commercial Law.

ACKNOWLEDGEMENTS

In accordance with contract No. 1.2.1.1/18/A/001 between ETKC Ltd. and the Central Finance and Contracting Agency, the study has been conducted by Lafivents Ltd. with support from the European Regional Development Fund (ERDF) within the framework of the project "Energy and Transportation Competence Centre".

REFERENCES

1. EUROSTAT. (2020). *Electricity Production, Consumption and Market Overview*. Available at https://ec.europa.eu/eurostat/statistics-explained
2. *National Energy and Climate Plan of Latvia for 2010–2030*. ME, Riga, 2019.
3. EC. (2011). *Roadmap for Moving to a Competitive Low Carbon Economy in 2050.* Available at https://eur-lex.europa.eu/legal-content/LV/TXT/PDF/?uri=CELEX:52011DC0112&from=LV
4. IEA. (2019). *Global Energy and CO_2 Status Report.* Available at https://www.iea.org/reports/global-energy-co2-status-report-2019/emissions#abstract
5. de Fatima Castro, M., Colclough, S., Machado, B., Andrade, J., & Braganca, L. (2020). European Legislation and Incentives Programmes for Demand Side Management. *Solar Energy*, *200*, 114-124.
6. Azarova, V., Cohen, J.J., Kollmann, A., & Reichl, J. (2020). Reducing Household Electricity Consumption during Evening Peak Demand Times: Evidence from a Field Experiment. *Energy Policy*, *144*, 111657. DOI: https://doi.org/10.1016/j.enpol.2020.111657
7. Yilmaz, S., Chambers, J., & Patel, M.K. (2019). Comparison of Clustering Approaches for Domestic Electricity Load Profile Characterisation – Implications for Demand Side Management. *Energy*, *180*, 665–677. DOI: https://doi.org/10.1016/j.energy.2019.05.124
8. Trotta, G. (2020). An Empirical Analysis of Domestic Electricity Load Profiles: Who Consumes How Much and When? *Applied Energy*, *275*, 115399.
9. Cicek, A., Erenoglu, A.K., Erdinc, O., Bozkurt, A., Tascikaraoglu, A., & Catalao, J.P.S. (2021). Implementing a Demand Side Management Strategy for Harmonics Mitigation in a Smart Home Using Real Measurements of Household Appliances. *International Journal of Electrical Power & Energy Systems*, *125*, 106528.
10. Bandyopadhyay, A., Leibowicz, B.D., Beagle, E.A., & Webber, M.E. (2020). As One Falls, another Rises? Residential Peak Load Reduction through Electricity Rate Structures. *Sustainable Cities and Society*, *60*, 102191.
11. McPherson, M., & Stoll, B. (2020). Demand Response for Variable Renewable Energy Integration: A Proposed Approach and its Impacts. *Energy*, *197*, 117205.
12. Bouvenot, J.-B., Latour, B., Flament, B., & Siroux, M. (2020). High Resolution Stochastic Generator of European Household Specific Electricity Demand Load Curves for Decentralized Power Self-Production Applications. *Energy and Buildings*, *229*, 110480.

13. Valdes, J., Macia, Y. M., Dorner, W., & Camargo, L. R. (2020). Unsupervised Grouping of Industrial Electricity Demand Profiles: Synthetic Profiles for Demand-Side Management Applications. *Energy*, 118962.
14. Khripko, D., Morioka, S. N., Evans, S., Hesselbach, J., & de Carvalh, M. M. (2017). Demand Side Management within Industry: A Case Study for Sustainable Business Models. *Procedia Manufacturing, 8*, 270–277.
15. Cardoso, C. A., Torriti, J., & Lorincz, M. (2020). Making Demand Side Response Happen: A Review of Barriers in Commercial and Public Organisations. *Energy Research & Social Science*, *64*, 101443.
16. NordPool. (2020). *Day-Ahead Prices.* Available at https://www.nordpoolgroup.com/Market-data1/Dayahead
17. Escobar, P., Martínez, E., Saenz-Díez,E. Jiménez, J. C., & Blancoa, J. (2020). Modeling and Analysis of the Electricity Consumption Profile of the Residential Sector in Spain. *Energy and Buildings, 207*. DOI: https://doi.org/10.1016/j.enbuild.2019.109629
18. Central Statistical Bureau (CSB) of Latvia. (2020). *CSB Database.* Available at https://www.csb.gov.lv/en/statistika/db
19. Latio. (2018). *Mazumtirdzniecības platību tirgus pārskats*. *Biroju tirgus pārskats*. Available at http://latio.lv/lv/pakalpojumi/tirgus-analize/komercipasumu-tirgus
20. CRE. (2015). *Tirdzniecības objektu klasifikācija.* Available at https://www.lanida.lv/sites/default/files/inline-files/CRE_classification_retail_LAT.pdf
21. Sorokins, J., Borodinecs, A., & Zemitis, J. (2017). Application of Ground-to-Air Heat Exchanger for Preheating of Supply Air. *IOP Conference Series: Earth and Environmental Science*, *90* (1), 012002. DOI: 10.1088/1755-1315/90/1/012002
22. Zemītis, J., & Kalamees, T. (2019). Analysis of Various Ventilation Solutions for Residential and Non-Residential Buildings in Latvia and Estonia. *Springer Proceedings in Energy*, *1*, 51–61. DOI: 10.1007/978-3-030-00662-4_5

sciendo

LATVIAN JOURNAL OF PHYSICS
AND TECHNICAL SCIENCES
2021, N 2

DOI: 10.2478/lpts-2021-0011

LIQUEFIED NATURAL GAS INFRASTRUCTURE AND PROSPECTS FOR THE USE OF LNG IN THE BALTIC STATES AND FINLAND

J. Savickis[1], L. Zemite[2], L. Jansons[2], N. Zeltins[2], I. Bode[2],
A. Ansone[2], A. Selickis[2], A. Broks[2], A. Koposovs[2]

[1]ITERA Latvija
50 Skanstes Str., Riga, LV-1013, LATVIA
[2]Riga Technical University,
Faculty of Electrical and Environmental Engineering,
Institute of Power Engineering
12-1 Azenes Str., Riga, LV-1048, LATVIA
*e-mail: laila.zemite@rtu.lv

In the early 2010s, only 23 countries had access to the liquefied natural gas (hereinafter – LNG). Import terminals, despite attractive short-term economics, took long time to build, and rigid supply contracts made truly global use of LNG rather complicated. Concerns about geopolitical risks also stunted demand growth from existing supply sources, even when new LNG export routes and sources became available.

Current natural gas market is very different, both in terms of market participants and accessibility and diversity of services. In 2019, the number of LNG importing countries reached 43. Rising competition among suppliers and increasing liquidity of markets themselves created favourable conditions to diversify contract duration, size, and flexibility. In addition, development of floating storage and regasification unit (hereinafter – FSRU) technology provided LNG suppliers with a quick response option to sudden demand fluctuations in regional and local natural gas markets [1].

Moreover, LNG is one of the major options not only for bringing the natural gas to regions where its pipeline supply infrastructure is historically absent, limited or underdeveloped, but also for diversification of the natural gas supply routes and sources in regions with sufficient state of pipeline delivery possibilities. And it concerns smaller natural gas markets, like the Baltic States and Finland as well. Accordingly, prospects for use of LNG there in both mid and long-term perspective must be carefully evaluated, especially in regards to emerging bunkering business in the Baltic Sea aquatory and energy transition in Finland, replacing coal base-load generation with other, more sustainable and environmentally friendly alternatives.

Keywords: *Bunkering, Finland, LNG, LNG infrastructure, natural gas, the Baltic States.*

1. INTRODUCTION

LNG is the natural gas that has been cooled to a liquid state, at about -260° Fahrenheit, for shipment, distribution and storage. The volume of the natural gas in liquid state is about 600 times less than its volume in the gaseous state [2], [3]. Thus, process of liquefaction makes possible to transport the natural gas to significant distances – different continents and parts of the globe, or simply places, which pipeline infrastructure does not reach. Markets that are too far away from producing regions to be connected directly to them via pipeline infrastructure have access to the natural gas exclusively because of LNG.

For large-volume transportation, LNG is loaded onto double-hulled carrier ships, which are used for both safety and insulating purposes. Once the carrier arrives at the receiving port, LNG is off-loaded into storage tanks or regasified for injection into a pipeline distribution network [4]. LNG can also be shipped in smaller quantities, usually over shorter distances and used as a bunkering fuel. There is also a growing segment of very small-scale LNG shipments, which are usually performed by using the same containers as used on trucks in international trade, specially outfitted with cryogenic tanks [5]. Other small-scale LNG activities include peak demand response liquefaction and storage facilities, which can hold the natural gas compactly for periods of high demand. In some regions, particularly, in the US and Canada, LNG is also brought by truck to and from these facilities.

In 2020, there were 29 large-scale LNG import terminals in operation in Europe. Twenty-one of them are located in the current Member States of the European Union (hereinafter – EU) – and therefore subject to the EU regulation, three – in the UK and four – in the third countries (Turkey and the Russian Federation). Twenty-three are land-based LNG import terminals, five – FSRUs, and one, located in Malta, is an import facility comprised of a floating storage unit and onshore regasification facility. Six terminals – South Hook, Dragon, Isle of Grain in the UK, Gate in the Netherlands, Rovigo in Italy and Dunkerque in France – have been granted exemptions from the EU rules on regulated third party access [6].

Europe's increasing prominence in the global LNG market continued throughout 2018, 2019 and 2020. In 2018, its 15 LNG importing countries collectively held a 15.6 % share of the total global LNG import market, demonstrating a 6.4 % rise in comparison with results of 2017.

In 2019, the European LNG importers increased their global market share to 24.2 %, and the volume of LNG imported by 75.6 %. As a whole, the total amount of LNG imported by the EU Member States was more than 108 billion cubic meters (hereinafter – BCM). In comparison with 2018, the rise was rather significant – by 48BCM. The biggest LNG importers in the EU were: Spain with 22.4, France with 22.1, the UK with 18, Italy with 13.5, the Netherlands and Belgium with 8.6 – 8.8 BCM. As a result of increasing import volumes and decreasing average annual prices, the monetary value of the EU LNG imports in 2019 reached 16.2 billion euros (hereinafter – EUR), slightly up from EUR 15.4 billion in 2018 [6]. Qatar was the largest exporter of LNG to Europe, followed by the Russian Federation and the US.

Between 2017 and 2023, the global liquefied natural gas trade is expected to grow by more than 100 BCM, from 391 to 505 BCM, and large share of this growth

is expected to be contributed by the US natural gas exporters. Moreover, shrinking percentage of the natural gas use in the EU Member States has not been an obstacle for the International Energy Agency to estimate that LNG imports to Europe in 2040, if compared to 2016 levels, should increase by almost 20 % [7], because blend of the natural gas and renewables gases (hereinafter – RG) is widely recognised as valid transitional fuel in a way to decarbonization of the EU's power generation and transportation sectors over the next three decades [8].

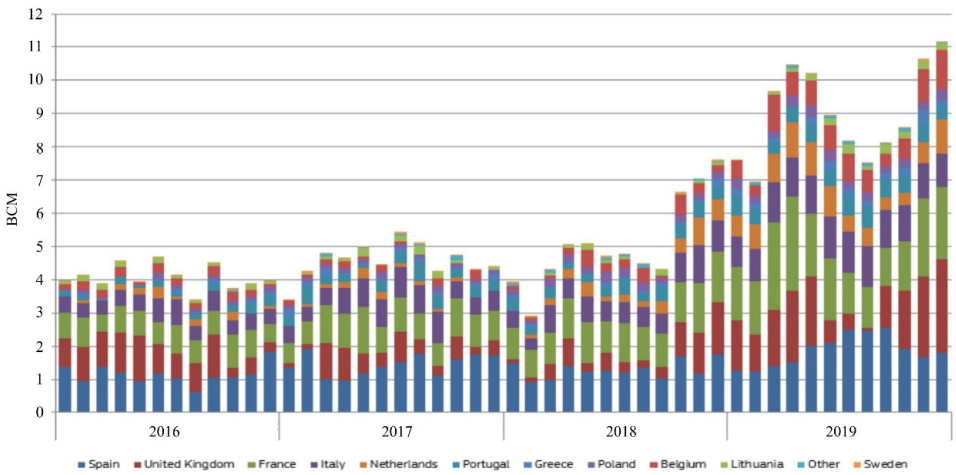

Fig. 1. The EU LNG import (by Member State, in BCM).

Source: EC calculations based on tanker movements reported by Thomson Reuters.

The major pathway to decarbonization of the EU's energy and transport – the European Green Deal – provides a framework for the EU's energy transition with the aim of achieving net-zero greenhouse gas (hereinafter – GHG) emissions by 2050 [9], [10]. The natural gas, including regasified LNG, is being regarded as suitable fuel for the energy transition – in light of its lower carbon intensity compared to heavier fossil fuels. The natural gas might prove not to be carbon neutral enough in a long term, but it is surely clean enough to play an important role in the European energy supply mix in the short and mid-term perspective. As for Europe's transition from fossil fuels such as coal and oil to renewable energy sources (hereinafter – RES), the natural gas can bridge a gap by providing a reliable, non-intermittent source of energy. Therefore, LNG serves to diversify sources and routes of the natural gas import to Europe.

While pipeline natural gas deliveries from Russia and Algeria, amongst others, will continue to supply a large proportion of the natural gas for the EU, with phasing out of coal and lignite-fired power generation and the continued decline of the domestic natural gas production, a growing share of LNG in the European primary energy mix is highly likely [6], especially, in such sectors as maritime and heavy-duty road transport, and power generation.

Table 1. The Natural Gas Consumption in the Baltic States and Finland (TWh (BCM), 2017–2019)

	TWh (BCM)		
	2017	**2018**	**2019**
Estonia	5.2 (0.53)	5.2 (0.53)	4.8 (0.49)
Latvia	13.1 (1.34)	15.1 (1.55)	14.3 (1.46)
Lithuania	24.2 (2.48)	22.3 (2.28)	23.6 (2.42)
Finland	17. 6 (1.8)	21.5 (2.2)	19.5 (2)
Total	60.1 (6.15)	64.1 (6.56)	62.2 (6.37)

Despite the fact that overall natural gas consumption in the Baltic and Finland is decreasing or standing still at best [11], the demand for the Baltic small-scale LNG market is projected to reach 1.908 million tonnes of LNG per annum (between 1.38 and 1.41 BCM of the natural gas per annum) by 2030, actuating at an estimated compound annual growth rate of 14.01 % from 2020 to 2030. Some estimates show that increasing investment in LNG infrastructure and strong support from the local governments for adoption of LNG as a marine and road transport fuel are expected to give a significant push to an actual market growth in the Baltics in the nearest future [12].

As for infrastructure, the expected investment growth includes, but is not limited to, building of new LNG import terminals, bunkering points, truck fuelling stations, and, possibly, small-scale autonomous natural gas supply networks. Currently, the Baltic States and Finland have three operational LNG terminals, only one of which – Klaipėda LNG in Lithuania – is connected to the natural gas transport network. The second terminal of this kind – Hamina LNG in the South-eastern part of Finland – is expected to be in full commercial operation in 2021.

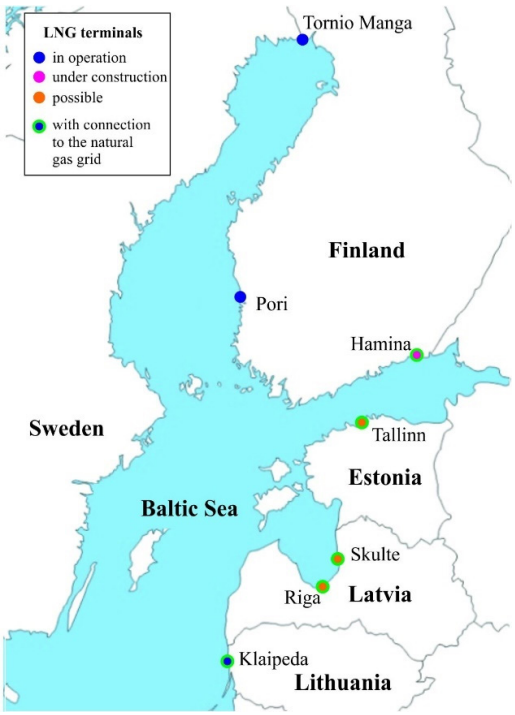

Fig. 2. LNG terminals in the Baltic States and Finland.

Klaipėda LNG terminal currently serves as a hub for LNG import in the north-eastern Baltics; however, with recent developments in Estonia and possible LNG projects in Latvia, at least partial relocation of LNG import traffic might take place by or shortly after 2030 [12].

2. LNG INFRASTRUCTURE AND DELIVERIES TO THE BALTIC STATES

2.1. Lithuania

As it has been mentioned before, the only Baltic State currently possessing LNG terminal is Lithuania. The geographically closest large-scale LNG terminal outside the Baltic States is Świnoujście LNG in Poland, but currently it cannot be part of the Baltic regional natural gas market because it is not yet connected to the Baltic–Finnish natural gas network.

Klaipėda LNG started its operation on 3 December 2014, and therefore Lithuania became the fifth country in the world to use FSRU technology for LNG imports. The central element of the Klaipėda LNG terminal – FSRU "Independence", the LNG carrier built by "Hyundai Heavy Industries", was leased from "Höegh LNG" for ten years with a possibility of buyout. It has a maximum import capacity of almost 4 billion cubic metres (hereinafter – m^3) of the natural gas per annum (2.2 million tonnes of LNG), while it has four storage tanks with total capacity of 170.000 m^3. The Lithuanian Parliament voted to operate its LNG import facility at least until 2044 and advised JSC Klaipedos Nafta to negotiate a purchase of the LNG regasification vessel in the late 2024 [13].

By the end of 2020, the total amount of loading and re-loading operations carried out at Klaipėda LNG terminal reached 200. Since 2014, more than 80 TWh (terawatt-hours (hereinafter – TWh); 8.19 BCM) of the natural gas has been regasified and supplied to the Lithuania national natural gas grid from the terminal. Last year alone, 20 TWh (2.05 BCM) of natural gas was regasified there, and, as a result, approximately 70 % of the year's natural gas delivery in Lithuania was carried out through Klaipėda LNG terminal.

The year 2020 was particularly favourable for the American LNG imports to Europe, including the Baltics. Between 2016 and October 2020, 10 cargoes from the US were delivered to Lithuania, totalling 9.37 TWh (0.96 BCM) of LNG. Last year, LNG cargos from the US made up 37 % of total LNG import of Klaipėda LNG terminal. About 49 % of LNG was imported from Norway, but the rest – by small quantities only – from other sources.

However, in comparison, the US LNG deliveries to Lithuania between 2016 and 2020 corresponded to 0.5 % of all its LNG export operations [7].

As for 2021, more than 14 TWh (1.43 BCM) of regasification capacity has already been ordered at Klaipėda LNG terminal.

2.2. Latvia

Currently, Latvia lacks any elements of the LNG import infrastructure, although several propositions to build a terminal in different locations were presented over the course of the last decade. The first proposition is related to Kundzinsala Southern Project, or more commonly known as Kundzinsala LNG terminal project. According to information of the Freeport of Riga, LNG terminal with an area of 34 hectares was planned to be built on the island of Kundzinsala – the largest island in the Daugava River in Riga, which is mainly used as a maritime trade related industrial area. Instead of planning connection to the natural gas transmission network, developers of

Kundzinsala LNG terminal made a decision in favour of connection to the natural gas distribution grid. The geographical location of the terminal was a reason why its connection to the natural gas transmission network was not regarded as economically and technically feasible. Project team requested and received technical regulations from the Latvian natural gas distribution system operator to make a connection to the natural gas distribution system in Riga. In order to make a connection, the LNG terminal operator was obligated to build the following elements of infrastructure and technical equipment: supply pipeline from the terminal to the distribution system, a gas connection point and a metering station with a gas chromatograph [14].

The expected business areas of the terminal were outlined as follows: bunkering, trade of LNG, including deliveries to road transport filling stations and alternative distribution networks, and injection of regasified natural gas into the Latvian natural gas distribution network.

So far there are no indications that would signal a possible beginning of construction of the LNG terminal complex in Kundzinsala in foreseeable future. As an alternative, a proposal to construct LNG terminal in Skulte, the Northwestern part of Riga Gulf, emerged. Skulte project was presented as a floating regasification unit without LNG storage tanks, but with a direct pipeline connection to the Incukalns underground gas storage (hereinafter – Incukalns UGS) facility. Unfortunately, this type of LNG terminal is not designed to supply unregasified LNG, which could be transported further by trucks, for example, to liquefied or compressed – liquefied natural gas (hereinafter – L-CNG) filling stations [15].

The Skulte project developers state that the project has unique geographic, economic and technological advantages over any other LNG import terminal proposal of comparable capacity. A fact that LNG cold storage facility, which usually takes up to 70–80 % of LNG import terminal building expenses, is not needed was presented as its obvious strong point. Instead, the developers made an assumption that Incukalns UGS will serve as a permanent storage for all delivered natural gas resources, and direct high-pressure pipeline connection between the storage and the LNG terminal will be built. Therefore, unparalleled flexibility would be provided to all the project, as LNG can be acquired extensively in favourable market conditions on a spot market basis, and stored in the UGS for winter consumption, while the terminal can reduce operation in high price periods.

Despite the fact, that preliminary costs of the project are not yet known, the developers announced, that total estimated investments would be at least 3 times less than for any other LNG terminal type of comparable capacity with LNG cold storage option [16].

It is estimated that, being in full operation, the regasification capacity of Skulte LNG terminal would reach 3 million tons of LNG per annum, and it would be able to receive LNG carriers of significantly various sizes: between 40.000 and 170.000 m^3, and unload them in the period of time from 3 to 6 days.

The project is reapplying for the EU Projects of Common Interest (hereinafter – PCI) status under the 5th round of the PCI projects to be decided by the European Commission by the end of 2021 and, according to several sources, this may require repurposing of the project to handle not only traditional LNG, but also biomethane and hydrogen as well [17]. The environmental impact of the project is ongoing since December 2018 [16].

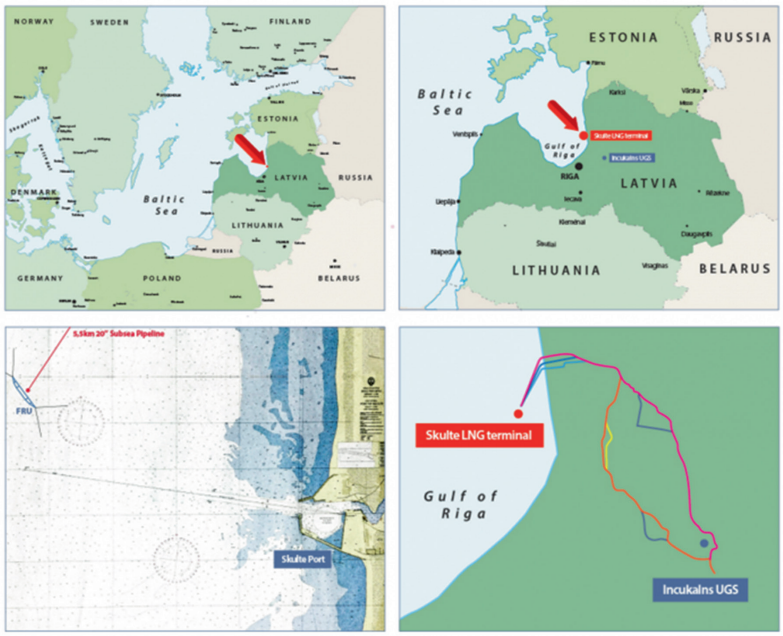

Fig. 3. Proposed location of Skulte LNG terminal with possible pipeline connection routes between it and Incukalns UGS.

Source: skultelng.lv.

Significantly enough, that in 2017, as a part of the Baltic Energy Market Interconnection Plan (hereinafter – BEMIP), the regional natural gas transmission system operators jointly completed the development of the third Gas Regional Investment Plan (hereinafter – GRIP), providing unified information on the planned projects in the BEMIP region. In this plan, the following LNG terminal projects are said to be implemented in the Eastern Baltics: construction of the Paldiski and Tallinn LNG terminals in Estonia, and acquisition of Klaipėda LNG terminal [18], [19]. At the same time, GRIP includes none of potential LNG import terminal projects from Latvia.

2.3. Estonia

Estonia, like Latvia, does not have its own LNG import facility, but Port of Tallinn authority is considering the possibility of building the LNG receiving terminal at a location in either Muuga Harbour or Paldiski South Harbour [18]. The purpose of the LNG terminal would be to receive LNG from carrier ships, store it in storage tanks, vaporise, and then deliver the natural gas to a high-pressure distribution pipeline or to the local major natural gas consumers.

Tallinn LNG terminal in particular would be designed as truck loading, security of supply and bunkering terminal at Muuga harbour with an initial LNG storage capacity of 4000 m³, truck loading rack and up to 0.5 BCM per annum connection to the natural gas grid through a connection point located about 1 km from the terminal. The terminal would be connected to an existing berth.

There is also a possibility to expand the terminal into an on-land break bulk facility that can service any ship on the market by

constructing up to four vertical LNG storage tanks with a storage capacity from 50 000 to 250 000 m^3, connecting to a second berth and expanding the natural gas grid connection up to 4 BCM per annum through connection into the high-pressure grid located about 13 km from the terminal [20].

2.4. Bunkering Activities

According to consulting company "DNV GL", there were 177 LNG-powered vessels in operation worldwide in 2020. By 2027, another 208 vessels using this type of fuel are expected to be built. The highest concentration of such ships is currently recorded in the North and Baltic Seas. Thus, bunkering is a fast growing and attractive business opportunity, which is also welcomed by the Baltic ports, and particularly Port of Klaipėda. The port conducted its first LNG bunkering operation on 8 March 2020, with supply of LNG to a cement carrier from the Malkos Bay Terminal [21]. In addition, on 7 January 2019, the world's largest LNG transportation and bunkering vessel "Kairos" was launched. Its main activity in the port of Klaipėda is moving LNG from the terminal to the LNG reloading station situated next to the gates of the port [22].

On 14 January 2021, the fourth load of approximately 3000 m^3 of LNG arrived at the "Klaipėdos Nafta" reloading station, but the previous three loads were delivered in June, August and November 2020, respectively [23]. Since April 2020, the reloading station is almost exclusively used for operations of the Polish energy company PGNiG. In total, since beginning of its bunkering operations, more than 4000 tons or 250 tank trucks of LNG were loaded in Klaipėda.

Bunkering activities are also carried out in other Baltic countries. For instance, the Estonian natural gas company "Eesti Gaas" – one of the major LNG suppliers and the biggest truck-to-ship bunkering service providers in the Northern Europe – in one month period delivers around 1300 tons of LNG and conducts an average of 65 truck-to-ship bunkering operations [24].

3. LNG INFRASTRUCTURE IN FINLAND

The construction of Finland's first LNG import terminal, located in the city of Pori, was completed in 2016. Currently, it is in full operation. In addition, the Manga LNG import terminal in the city of Tornio was inaugurated in June 2019. There is also the LNG import terminal under construction in Hamina, which is expected to be ready for commercial operation in the first half of 2021 [25].

Construction of the Pori LNG terminal, amounting to EUR 81 million, began in August 2014, and was completed in September 2016, but the first load of LNG arrived there in July 2016. The Ministry of Economic Affairs and Employment of Finland provided EUR 23 million funding for the terminal project. The EC approved the funding under the EU state aid rules in September 2015 [25].

The terminal consists of an LNG tank (height 35 m, outer diameter 42 m), loading docks, process units – compressor and vaporizers –, flare torch (height less than 50 m), three loading docks for road tankers, transformer building, and heat production unit. The terminal has LNG storage capacity of approximately 30.000 m^3. The LNG

deliveries to industrial customers are made through the local natural gas distribution network, by sea in bunkering vessel or by trucks. Ship-to-ship bunkering operations are available at Pori LNG terminal. There is also a 12 km long natural gas pipeline that connects the terminal to the local Industrial Park. Construction of the pipeline, which passes through roads, railways and the seabed, began in early August 2015. A 3.2 km section of the pipeline was laid under the sea, and trenching and pipe-laying works presented multiple challenges due to complicating environmental conditions [26].

Tornio Manga LNG terminal at Röyttä port, Tornio, is the second LNG import facility built in Finland. It is a result of cooperation of several large-scale industrial and energy companies, such as Outokumpu, Ruukki Metals, EPV Energy and Gasum. The companies agreed on the LNG import project to deliver the natural gas to industrial consumers, energy producers and shipping businesses in the North of Finland, where pipeline naturas gas is not available. At the period of construction, it was the largest such facility in the Nordic region with a logistics chain developed around the terminal to create a diversified fuel market benefiting both northern Finland and Sweden [27].

With construction cost of about EUR 100 million, the terminal has complete unloading, storage, pipeline distribution, regasification, truck loading, and ship bunkering facilities. The terminal supplies natural gas to Outokumpu's Tornio steel mill and LNG to local industries, mines, and other consumers in the region. LNG from the terminal will also be supplied to the LNG storage facility at the SSAB Raahe steel mill [28], [29]. From the second half of 2020, Gasum begun delivery of LNG to Eastman Chemical Company in Oulu, as well. The LNG deliveries are carried out by tanker trucks, and the company's switch to usage of LNG is part of the regional commitment to environmental sustainability [30].

Finland's third LNG terminal – Hamina LNG – is currently under construction at the Hamina Harbour, Kotka. Unlike Pori and Tornio terminals, it will be connected to the natural gas transmission system of Finland and to the local natural gas distribution networks. Therefore, Hamina LNG will provide the Baltic–Finnish natural gas market with a new natural gas physical delivery point. It is estimated that the terminal will be in commercial operation by mid-2021.

The storage capacity of the Hamina LNG terminal will initially be 30.000 m^3, with a possibility of upgrade by additional 20.000 m^3. Its entry capacity into the transmission system as well as into the local distribution system will be 0.5 million m^3 per day [25]. It is estimated that approximately 20 ships per year will deliver LNG to Hamina, with a single ship carrying from 5.000 to 25.000 m^3 of LNG.

The Ministry of Economic Affairs and Employment of Finland provided EUR 27.7 million co-funding for the construction of Hamina LNG terminal [31].

4. PROSPECTS FOR THE USE OF LNG IN THE EASTERN BALTICS

For the Baltic States and Finland alike, prospects for the use of LNG can be linked to the following activities: usage of LNG as maritime and road transport fuel, future utilisation of LNG infrastructure for transportation of liquefied biomethane (hereinafter – LBG) and, possibly, other RG, and usage of LNG in energy generation (as an

alternative to fossil fuels with more significant GHG emission intensity).

Directive 2014/94/ EU of the European Parliament and of the Council of 22 October 2014 on the deployment of alternative fuels infrastructure (hereinafter – Directive 2014/94/EU) defines a common framework of measures for the deployment of alternative fuels infrastructure in the EU in order to minimise dependence on oil and to mitigate the environmental impact of transport. It sets out minimum requirements for the building-up of alternative fuels infrastructure, including LNG stations with non-discriminatory access for LNG fuelled vessels and road vehicles. According to the Directive, a core network of refuelling points for LNG at maritime and inland ports should be available at least by the end of 2025 and 2030, respectively. Refuelling points for LNG include, *inter alia*, LNG terminals, tanks, mobile containers, bunker vessels and barges.

Though in the aquatory of the North Sea LNG import terminals are widely spread, the Baltic ports are still struggling to catch up. The LNG terminal development seems favourable for the Eastern Baltics – the Baltic States and Finland, as they will provide decreasing energy dependency by increasing gas supply diversification. Moreover, LNG terminals provide regional shipping with an alternative type of low-emission marine fuel and, in general, with increasingly diverse natural gas supply routes and sources. Among others, Directive 2014/94/ EU obligates the EU Member States to make available bunkering infrastructure for LNG in their territory and allows for their funding through the *Connecting Europe Facility* instruments [32].

Table 2. Types of Alternative Fuels and their Use

Fuel	**Type**	**Passenger cars**			**Heavy-duty vehicles**			**Air transport**	**Rail transport**	**Shipping**		
	Distance (km)	Less than 150	Less than 300	More than 300	Less than 150	Less than 300	More than 300			Inland	Short route	Long route
Natural gas	**LNG**	**X**	**X**	**X**	**X**	**X**	**X**		**X**	**X**	**X**	**X**
	CNG	X	X	X	X	X						
Bio-methane	**LBM**	**X**	**X**	**X**	**X**	**X**	**X**		**X**	**X**	**X**	**X**
	bioCNG	X	X	X	X	X						
Electricity		X	X		X	X			X			
Hydrogen		X	X		X	X			X	X	X	

In comparison with traditional fossil fuels such as heavy fuel oil, the use of LNG releases less CO_2, no sulphur oxide (hereinafter – SO_x), particulate matter and nitrogen oxide, and helps improve air quality. In future, LNG infrastructure can be utilised for import and distribution of LBG, which is a completely renewable energy source that reduces CO_2 emissions by as much as 85 % compared to traditional fuels.

4.1. LNG in Maritime and Road Transport

The EU has strived for an active role in tackling maritime emissions, both at home and globally. In 2018, the International Maritime Organization (hereinafter – IMO) agreed to reduce GHG emissions from shipping by at least 50 % in 2050. The EU and

its Member States play an instrumental role in brokering and securing the deal for the sector, which currently represents 2–3% of global CO_2 emissions. Discussions are already ongoing at the IMO to translate this deal into concrete measures [33].

In Europe, the choice of location for the LNG bunkering terminals depends on two major factors: firstly, the location of potential clients and, secondly, the suitable areas for building a terminal. LNG is considered an alternative fuel mainly for ships operating in liner service. Hence, LNG terminals for bunkering purposes should be constructed in locations where there are the most density of liner services.

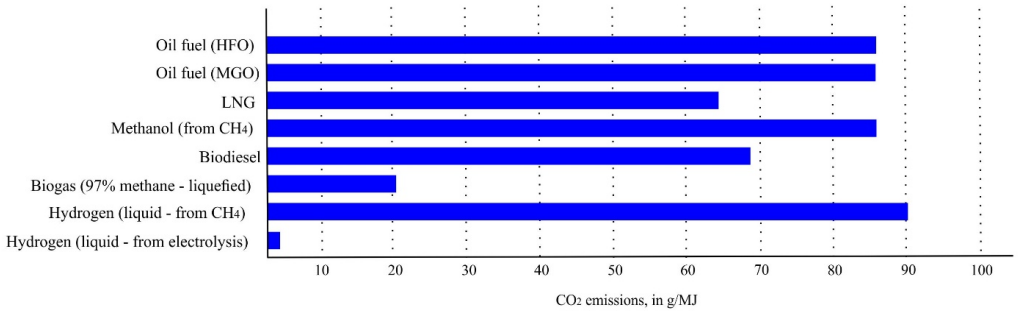

Fig. 4. CO_2 emissions for different types of fuel in shipping.

However, at the same time, choice must be guided by a coastal environmental situation, too, as maritime transport has a direct impact on air quality in many European seaside cities. Exhaust gases from ships are a significant source of air pollution, including SO_x emissions, which are extremely harmful to the human respiratory system. Ships traditionally use fuel oils for propulsion, which can have a sulfur content of up to 3.50 %. For comparison, the sulfur content of fuels used in trucks or passenger cars must not exceed 0.001 %.

The 2012 Sulphur Directive, which was revised in 2016 [34], reduced SO_x emissions by setting maximum sulfur content levels for marine fuels and incorporated new standards set by IMO into the EU legislation both inside and outside protected areas. In 2016, the IMO maintained 2020 as entry-into-force date of the global 0.5 % SO_x cap [33].

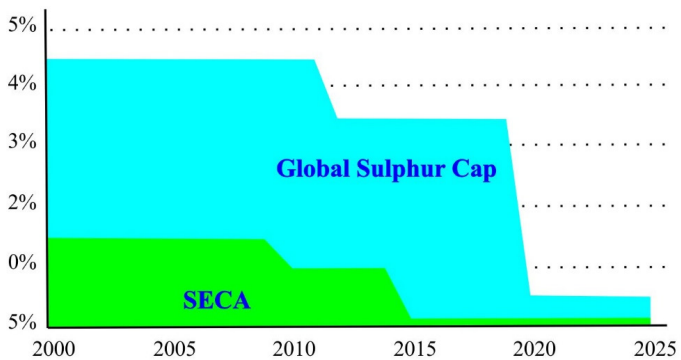

Fig. 5. IMO Sulphur Limits (2000–2025, in %).

However, in some very fragile ecosystems such as the Baltic Sea and the North Sea – designated as "Sulphur Oxides Emissions Control Areas" (hereinafter – SECA) – the maximum SO_x content has been reduced to 0.10 % already in 2015. Such stricter SO_x limits have more than halved SO_x concentrations around SECAs, bringing health benefits to people in coastal regions and ports, while the overall economic impacts on the sector remained minimal [35], [36]. A study on the human health impacts of SO_x emissions from shipping, submitted to IMO's Marine Environment Protection Committee in 2016 by Finland, estimated that by not reducing the SO_x limit for ships from 2020, the related air pollution would contribute to more than 570.000 additional premature deaths worldwide in next five years [37].

The Baltic Sea as one of the Europe's SECA areas also has good prospects to LNG use as a viable alternative maritime fuel. Moreover, the Baltic maritime trade and passenger ferry routes are quite compact, so different types of ships can be used with rather small fuel capacities, as refueling can be done both *en route* to next destination and in port of departure or arrival. Along with electric or hydrogen-powered ships, LNG ferries and transport vessels would contribute significantly to reduction of GHG emissions in the Baltic Sea aquatory in this decade. It is estimated that till 2040, LNG will play an important role in diversification of the maritime fuel portfolio in all regions of the EU. However, to achieve such a diversification in the Eastern Baltics, more active actions should be taken by the state, local authorities, and businesses.

Current energy consumption in the EU transport sector depends on oil fuels by 94 %. This dependency, among other problems, results in high levels of GHG emissions, which, consequently, triggers the necessary to increase the use of less polluting and more cost-effective alternative sources as natural gas. For instance, in comparison with diesel heavy-duty vehicles, LNG fuelled heavy-duty vehicles reduce GHG emissions up to 20 % per kilometre. They also eliminate 100 % of SO_x and particulate matter emissions, and help reach significant noise level reduction in densely populated areas [38].

Despite an increase in registrations in recent years, alternatively powered passenger cars in the EU make up only about 4 % of the total car fleet [39], [40]. In addition, the European consumption of natural gas in the transport sector is also quite low, amounting to less than 1 % of its total natural gas demand and to a bit more than 2 % of all vehicles on the road today [41], [39], [42].

Table 3. Road Vehicles by Fuel Types in the EU* (2018; %)

Type of Vehicle	Gasoline	Diesel	Hybrid Electric	Electric**	CNG, LNG, LPG	Other
Passenger cars	54	41.9	0.7	0.2	2.8	0.3
Light commercial vehicles	7.1	91.2	0	0.3	1.3	0.1
Medium and heavy-duty commercial vehicles	1	98.3	0	0	0.4	0.2
Buses	0.8	95.4	0.3	0.3	2.7	0.4

*- including the United Kingdom
* - battery electric + plug-in hybrid
Source: ACEA Report Vehicles in use, Europe 2019

At the same time, natural gas and other gases, both in the compressed and liquified states, are considered one of the most important elements of the European road transport decarbonisation path. By law, they are regarded as part of "alternative fuel" scope. According to Article 2 (1) of Directive 2014/94/EU, "alternative fuels" are sources of fuel or energy, which at least partially replace fossil fuel oil sources in vehicle power supply and which have the potential to contribute to decarbonisation of transport and the environmental performance of the transport sector. It defines, *inter alia*, the following alternative fuels: electricity, hydrogen, liquid biofuels (biodiesel, bioethanol and hydrogenated vegetable oil), biomethane, compressed natural gas (hereinafter – CNG) and LNG. It should also be pointed out that CNG and LNG can originate from various sources – both conventional natural gas and biogas – upgraded till the biomethane level. From the chemical standpoint, natural gas and biomethane are practically identical.

In the Baltic States and Finland, the percentage of alternatively fuelled road vehicles remain rather low, with the natural gas-powered road vehicle fleet in Latvia being equal to about a few hundred. Currently there are only two LNG filling stations in the Baltic States, both located in Estonia, and 9 filling stations located in Finland. It is important to mention that most of these filling stations can serve both CNG and LNG fuelled vehicles. L-CNG filling stations allow filling CNG for light and LNG for heavy-duty vehicles. Such filling stations have lower capital and operating costs than separate LNG and CNG filling stations of similar capacity [43]. LNG is used as a raw material in L-CNG filling stations, and it is stored at a very low temperature: about -163 °C, at a pressure of 1 bar. 1 litre of LNG at a pressure of 1 bar contains about 600 litres of natural gas. The type of CNG and LNG combined station is very advantageous in case if there is no natural gas grid access nearby [44].

L-CNG filling stations are advantageous for several reasons, as they:

- allow expanding the network of alternative fuel filling stations throughout the Baltic region and Finland;
- allow setting up natural gas based multifuel type filling stations in places, where pipeline natural gas is not available, or construction of corresponding infrastructure is not financially feasible;
- expand potential availability of RG, firstly and foremostly, LBM [44].

As for the beginning of 2021, there were four public CNG filling stations, one closed filling station and three natural gas filling points available in Latvia. A study by the Ministry of Transport on the Development of Alternative Fuels concludes that the natural gas, including CNG and LNG, will be a transition fuel in a way to transport sector decarbonisation. Thus, in next fifteen years, according to the most ambitious scenario of the gas filling station expansion along the Latvian natural gas distribution network, 172 CNG (69 of them along Core TEN-T network roads in 9 municipalities) and 6 LNG stations could be installed [45]. It is highly likely that at least some of these stations would be suitable to serve CNG and LNG simultaneously.

According to the most optimistic estimates of the alternative fuel development in Latvia as a whole, by 2050 CNG and LNG will account for more than any other transport fuel in fleet, including diesel and gasoline, but for fulfilment of such a high ambition much stronger and politically coordinated support of RE industry, firstly and foremostly domestic biomethane production and use, is necessary [46].

4.2. LBM and LNG in Energy Generation

The statistics show that the dynamics of the biomethane production with its subsequent conversion into LBM has demonstrated a significant upward pattern between 2018 and 2020. In this period, a number of biomethane plants in the EU have increased by 51 %, from 483 in 2018 to 729 in 2020. There are currently eighteen countries producing biomethane in Europe, with Germany having the highest share of biomethane production plants (232), followed by France (131) and the UK (80) [47].

In the Baltic States, upgrading of the biogas to biomethane level with subsequent injection into the natural gas transportation or distribution grids is not developed yet. However, at least Latvia with 59 existing biogas plants and 17 of them being located 10 or less km away from the natural gas distribution grids could benefit both from biomethane production and local sales (where CNG filling stations and/or small-scale biomethane liquifying facilities are installed onsite) and injection of the biomethane into the natural gas networks [40].

Moreover, in this decade the EU production of LBM is set to increase by factor of ten. The EU LNG heavy-duty transport is expected to reach 280.000 units in the same period. Using a 40 % LBM mix with LNG will help reduce the CO_2 emissions from those trucks by 55 %. In the shipping sector, 50 % of large container vessel orders today are LNG fuelled or ready for conversion to LNG. 20 % of LBM mix in maritime transport would reduce CO_2 emissions by up to 34 %.

But, as it was stated before, a tandem of the natural gas and biomethane could be named as one of the most promising mid-term transport decarbonisation solutions in the Baltic States and Finland as well. LBM can be transported using the existing LNG infrastructure with no further technological adaptations or additional costs. For this reason, the support of LNG infrastructure is fundamental to ensure the deployment of LBM in the coming years. Today, the EU has 53 ports where LNG bunkering is available and over 330 LNG filling stations, and the number of filling stations is meant to increase sixfold, reaching 2000 by 2030.

The use of the current LNG infrastructure will also boost cross-border trade of LBM in Europe [48].

In addition to its conventional role in the natural gas market, LNG may also be an energy source for power generation. Power generation from LNG is partially used to maintain the regasification at the LNG receiving terminals, as these processes are rather energy demanding. The basic thermodynamic processes used in power generation from LNG are: the direct expansion of the regasified and pressurized natural gas, the Rankine cycle and Brayton cycle with use of an auxiliary fluid which expands and propels the turbine. For the pressures up to 3 Megapascals, the suitable option for power generation is simple Rankine cycle and Brayton cycle, for higher pressures – the direct expansion of regasified LNG or other complex processes based on modified Rankine or Brayton cycles should be considered [49].

In the Baltic region, use of LNG in power generation is a viable energy transition option, which might prove itself suitable while supporting Finland's gradual elimination of coal, lignite and, possibly, peat in its power generation sector. If CO_2 intensity of the natural gas and coal (hard coal), lignite and peat is compared, it is obvious that natural gas contributes to almost 50 % CO_2 emission cut. Namely, CO_2 intensity of hard coal is about 0.34 kg of CO_2 per kilowatt-

hours (hereinafter – kWh), the intensity of lignite and peat: 0.36–0.41 and 0.38 kg of CO_2/kWh, but the intensity of natural gas – 0.20 kg of CO_2 /kWh of energy generated.

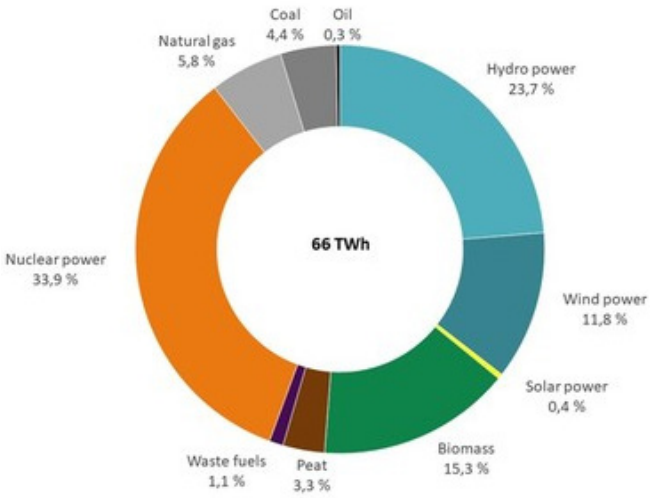

Fig. 6. Electricity production in Finland (2020, by source in %).

Source: energia.fi.

LNG is suitable for large- and small-scale power generation: both in cogeneration and condensation cycles. For example, from 66TWh of electricity produced in Finland last year, coal contributed to 4.4 %, peat – to 3.3 %, but natural gas – to 5.8 %. If at least a half of energy generated from coal in future comes from natural gas – including LNG-based generation, it will mean that an increase in "the natural gas electricity" will be able to reach 1.9 TWh, with associated CO_2 emission dropping by almost a half.

5. CONCLUSION

The Baltic States and Finland currently have three operational LNG terminals, and one more terminal is about to come online later this year. Two out of three terminals are located in the Northern part of Finland and lack connection to the Finnish national natural gas grids and, therefore, common Baltic–Finnish natural gas market. It makes Klaipėda LNG terminal the only facility in the region, which has such a connection, and can play its role in the market.

The situation, however, is about to change at least from the formal standpoint, as Hamina LNG terminal will soon become the second LNG terminal in the Eastern Baltics to possess an ability to participate in the natural gas market in a capacity of a brand-new natural gas supply route.

Currently the Baltic–Finnish natural gas market shows signs of relative stability, and the gradual switch from the pipeline natural gas to LNG might be expected in

the mid-time perspective. The role of LNG is expected to grow both in maritime and road transport of the Eastern Baltics, and its power generation sector – especially, with Finland's transition from usage of coal in electricity and heat generation to another, more environmentally friendly sources. The deadline for coal generation phase-out is May 2029; however, Finnish energy producers can voluntarily make a transition by 2025 [50].

It will open door for another generation technologies and fuel sources, such as LNG and eventually – LNG and LBM mix, to step in. As LNG–LBM mix can be used both in transport and power generation, it is one of the most promising options for energy transition in the Eastern Baltics at a large scale – it will not be limited only to certain areas, where natural gas pipelines are available, and will bring benefits of gas technology usage to industrial regions with large energy consumption and urge to develop local energy logistic chains [25]. LNG will soon become indispensable in the growing bunkering business niche of the Baltic Sea aquatory. More terminals and more suppliers will mean a more dense market and better offers, both in ship-to-ship and track-to-ship bunkering segments.

In the road transport, wider coverage of L-CNG fuelling stations will bring extra profit to fuel retailers, and ensure an ever-expanding network of alternative fuel access points across the Baltic States and Finland. It would help cover the areas of four countries, where natural gas grids are not available, but CNG and LNG vehicles need to be fuelled anyway. But in regions, where biomethane production will develop, bioCNG and small-scale LBM fuelling stations and facilities can emerge as part of an alternative gas infrastructure for road transport fuelling.

The development of LNG import terminals of any kinds is the hardest thing to predict in the Eastern Baltics. Despite the fact that several projects in Latvia and Estonia are at different stages of planning, soon completion of at least one of them is rather questionable, and subject to further clarification.

ACKNOWLEDGEMENTS

The research has been supported by the National Research Programme, project "Trends, Challenges and Solutions of Latvian Gas Infrastructure Development" (LAGAS) (No. VPP-EM-INFRA-2018/1-0003).

REFERENCES

1. Bresciani, G., Heiligtag, S., Lambert, P., & Rogers, M. (2020). *The Future of Liquefied Natural Gas: Opportunities for Growth*. [online]. [accessed 1 December 2020]. Available at https://www.mckinsey.com/industries/oil-and-gas/our-insights/the-future-of-liquefied-natural-gas-opportunities-for-growth
2. Nersesian, R. L. (2010*). Energy for the 21st century: A comprehensive guide to conventional and alternative sources*. M.E. Sharp.
3. Whitney, G., & Behrens, C. E. (2010). *Energy: Natural Gas: The Production and Use of Natural Gas, Natural Gas Imports and Exports, EPAct Project, Liquefied*

Natural Gas (LNG) Import Terminals and Infrastructure Security, Underground Working Gas Storage, Fisher-Tropsch Fuels from Coal, Natural Gas and Biomass, Gas Hydrates, Gas Shales, Hydraulic Fracturing, Alaska Natural Gas Pipelines. The Capitol.Net, Inc.

4. US Office of Fossil Energy. Liquefied Natural Gas (LNG). (n.d.). [online]. [accessed 12 January 2021]. Available at https://www.energy.gov/fe/science-innovation/oil-gas/liquefied-natural-gas
5. Swennen, R. (ed.) (2017). *China's gas development strategies*. Springer.
6. DG Energy. (2020). *Quarterly Report on European Gas Markets*. [online]. [accessed 5 March 2021]. Available at https://ec.europa.eu/energy/sites/ener/files/quarterly_report_on_european_gas_markets_q4_2019_final.pdf
7. EC. (2020). *EU-U.S. LNG Trade*. U.S. liquefied natural gas (LNG) has the potential to help match EU gas needs. [online]. [accessed 10 January 2021]. Available at https://ec.europa.eu/energy/sites/ener/files/eu-us_lng_trade_folder.pdf
8. IEA. (2019). *The Role of Gas in Today's Energy Transitions*. [online]. [accessed 5 February 2021]. Available at https://www.iea.org/reports/the-role-of-gas-in-todays-energy-transitions
9. Bryden, D., & Denton, S.-J. (2020). *The European Green Deal – Overview and Status Report*. [online]. [accessed 25 January 2021]. Available at https://www.lexology.com/library/detail.aspx?g=b18af039-49eb-484e-ac52-25820a7513e3
10. EC. (n.d.). *What is the European Green Deal?* [online]. [accessed 14 January 2021]. Available at https://ec.europa.eu/commission/presscorner/detail/en/fs_19_6714
11. Hokerts, J. (2020). Gāze – ekoloģiskiem un ekonomiskiem risinājumiem. In *Heat Supply Conference*, Riga.
12. Energia Market Research. (2019). *Baltic Countries Small-Scale LNG Market Outlook, Trend and Opportunity Analysis, Competitive Insights, Actionable Segmentation & Forecast 2020–2030*. [online]. [accessed 14 January 2021]. Available at https://www.energiasmarketresearch.com/baltic-small-scale-lng-market-report/
13. Gas Processing and LNG. (2020). *Lithuania to Import LNG until at least 2044, to Purchase LNG Vessel*. [online]. [accessed 10 March 2021]. Available at http://www.gasprocessingnews.com/news/lithuania-to-import-lng-until-at-least-2044,-to-purchase-lng-vessel.aspx
14. Gaso. (2019). *Kundziņsalas dienvidu projekts. Tehniskie noteikumi*.
15. Sināts, M. (2020). *Compressed Natural Gas as an Alternative Fuel for Road Transport in Latvia*. Master Thesis. Riga: RTU.
16. Skulte LNG Terminal. (2019). [online]. [accessed 3 February 2021]. Available at https://www.skultelng.lv/en/the_project/#i32
17. Summary: Revised TEN-E Regulation – Future Financing of European Energy Infrastructure. (2020). [online]. [accessed 16 January 2021]. Available at https://hsfnotes.com/energy/tag/pcis/
18. Conexus Baltic Grid. (n.d.). *Medium-Term Strategy for 2019–2023.* [online]. [accessed 9 January 2021]. Available at https://www.conexus.lv/uploads/filedir/Media/conexus_mid_term_strategy.pdf
19. GRIP Annex A: Infrastructure Projects. (2017). [online]. [accessed 6 January 2021]. Available at https://entsog.eu/public/uploads/files/publications/GRIPs/2017/entsog_BEMIP_GRIP_2017_Annex_A_web.pdf
20. Tallinn LNG. [online]. [accessed 31 January 2021]. Available at https://www.tallinnlng.com/
21. Seatrade Maritime News. (2020). *Lithuania's Klaipeda Port Embarks on LNG Bunkering*. [online]. [accessed 31 January 2021]. Available at https://www.seatrade-maritime.com/bunkering/lithuanias-klaipeda-port-embarks-lng-bunkering
22. World Maritime News. (2019). *Nauticor to Become Sole Charterer of LNG Bunker Vessel Kairos*. [online]. [accessed 10 February 2021]. Available at https://www.offshore-energy.biz/nauticor-to-become-sole-charterer-of-lng-bunker-vessel-kairos/

23. Vessel Finder. (2021). *PGNiG Received its Fourth LNG Delivery in Klaipėda*. [online]. [accessed 1 February 2021]. Available at https://www.vesselfinder.com/news/19934-PGNiG-received-its-fourth-LNG-delivery-in-Klaipda
24. Eesti Gaas. (n.d.). *LNG – Clean Fuel with Reasonable Cost*. [online]. [accessed 1 March 2021]. Available at https://www.gaas.ee/en/for-business/lng-liquefied-natural-gas/lng-bunkering/
25. Ministry of Economic Affairs and Employment of Finland. (2019). *Finland's Integrated Energy and Climate Plan.* [online]. [accessed 1 February 2021]. Available at https://ec.europa.eu/energy/sites/ener/files/documents/fi_final_necp_main_en.pdf
26. Hydrocarbons Technology. (n.d.). *Skangas LNG Import Terminal, Port of Tahkoluoto, Pori.* [online]. [accessed 1 February 2021]. Available at https://www.hydrocarbons-technology.com/projects/skangas-lng-import-terminal-port-of-tahkoluoto-pori/
27. LNG World News. (2019). *Manga LNG Inaugurates Tornio Receiving Terminal*. [online]. [accessed 10 February 2021]. Available at https://www.offshore-energy.biz/manga-lng-inaugurates-tornio-receiving-terminal/
28. Archana Rani, K.S. (2019). *Finland Commissions Tornio Manga LNG Receiving Terminal*. [online]. [accessed 2 February 2021]. Available at https://www.nsenergybusiness.com/news/finland-tornio-manga-lng-terminal/
29. Manga LNG Terminal. (n.d.). [online]. [accessed 5 February 2021]. Available at https://www.torniomangalng.fi/en/hankkeen-esittely/
30. Gasum. (2020). *Gasum Partners with New Customer in Liquefied Natural Gas Deliveries from Manga LNG Terminal in Tornio, Finland*. [online]. [accessed 23 January 2021]. Available at https://www.gasum.com/en/About-gasum/for-the-media/News/2019/gasum-partners-with-new-customer-in-liquefied-natural-gas-deliveries-from-manga-lng-terminal-in-tornio-finland/
31. Mediatiedote. (2020). *Tukes has Authorised the Construction of the Hamina LNG Terminal*. [online]. [accessed 2 February 2021]. Available at https://tukes.fi/en/-/tukes-has-authorised-the-construction-of-the-hamina-lng-terminal
32. Directive 2014/94/EU of the European Parliament and of the Council of 22 October 2014 on the deployment of alternative fuels infrastructure. [online]. [accessed 4 February 2021]. Available at https://eur-lex.europa.eu/legal-content/EN/TXT/?uri=celex%3A32014L0094
33. EC. (2020.) *Cleaner Air in 2020: 0.5 % Sulphur Cap for Ships Enters into Force Worldwide*. [online]. [accessed 4 March 2021]. Available at https://ec.europa.eu/transport/modes/maritime/news/2020-01-03-sulphur-cap_en
34. Directive 2016/802/EU of the European Parliament and of the Council relating to a reduction in the sulphur content of certain liquid fuels. [online]. [accessed 4 March 2021]. Available at https://eur-lex.europa.eu/eli/dir/2016/802/oj
35. International Maritime Organization. (n.d.). *Emission Control Areas (ECAs) Designated under MARPOL Annex VI*. [online]. [accessed 1 March 2021]. Available at https://www.imo.org/en/OurWork/Environment/Pages/Emission-Control-Areas-(ECAs)-designated-under-regulation-13-of-MARPOL-Annex-VI-(NOx-emission-control).aspx
36. Damgaard, J. (2020). *Low Sulphur Regulations after 1 January 2020.* [online]. [accessed 6 January 2021]. Available at https://britanniapandi.com/2020/01/low-sulphur-regulations-after-1-january-2020/
37. International Maritime Organization. (2016). *Air Pollution and Energy Efficiency*. Study on effects of the entry into force of the global 0.5% fuel oil sulphur content limit on human health. [online]. [accessed 9 March 2021]. Available at https://wwwcdn.imo.org/localresources/en/MediaCentre/HotTopics/Documents/Finland%20study%20on%20health%20benefits.pdf
38. Osorio-Tejada, J., Llera, E., & Scarpellini, S. (2015*). LNG: Aan Alternative Fuel for*

Road Freight Transport in Europe. [online]. [accessed 1 March 2021]. Available at https://zaguan.unizar.es/record/62843/files/texto_completo.pdf

39. European Automobile Manufacturers Association. (2018). *Vehicles in Use*. [online]. [accessed 9 March 2021]. Available at https://www.acea.be/statistics/tag/category/vehicles-in-use
40. Savickis, J., Zeltins, N., & Jansons, L. (2019). Synergy between the Natural Gas and RES in Enhancement of Security of Energy Supply in the Baltic Countries (Problem Statement). *Latvian Journal of Physics and Technical Sciences*, *56* (6), 17–31. DOI: https://doi.org/10.2478/lpts-2019-0032
41. ICCT. (2018). *European Vehicle Market Statistics, 2018/2019*. [online]. [accessed 3 March 2021]. Available at https://theicct.org/sites/default/files/publications/ICCT_Pocketbook_2018_Final_20190408.pdf
42. Savickis, J., Zemite, L., Zeltins, N., Bode, I., Jansons, L., Dzelzitis, E., …. & Ansone, A. (2020). The Biomethane Injection into the Natural Gas Networks: The EU's Gas Synergy Path. *Latvian Journal of Physics and Technical Sciences*, *57* (4), 34–50. DOI: 10.2478/lpts-2020-0020
43. Sharafian, A., Talebian, H., Blomerus, P., Herrera, O., & Mérida, W. (2017). A Review of Liquefied Natural Gas Refueling Station Designs. *Renewable and Sustainable Energy Reviews*, *69* (November 2016), 503–513. https://doi.org/10.1016/j.rser.2016.11.186
44. Reķis, J., Šmigins, R., Gailis, M., & Klāvs, G. (2018). *Pētījums par Eiropas Parlamenta un Padomes 2014. gada 22. oktobra Direktīvas 2014/94/ES par alternatīvo degvielu ieviešanu scenārijiem autotransporta sektorā*. *40003142793*, 146.
45. Bode, I. (2019). *Alternatīvās degvielas izmantošana* (presentation).
46. On Alternative Fuels Development Plan 2017–2020. [online]. [accessed 8 March 2021] Available at https://likumi.lv/ta/en/en/id/290393-on-alternative-fuels-development-plan-20172020
47. European Biogas Association, Gas Infrastructure Europe. (2020). *The European Biomethane Map 2020*. [online]. [accessed 3 March 2021]. Available at https://www.europeanbiogas.eu/wp-content/uploads/2020/06/GIE_EBA_BIO_2020_A0_FULL_FINAL.pdf
48. BioLNG Makes Carbon Neutrality a Reality for EU transport. (2020). [online]. [accessed 4 March 2021]. Available at https://www.europeanbiogas.eu/wp-content/uploads/2020/11/News-Release_BioLNG_Paper_EBA-GIE-NGVA-Europe-SEA-LNG-WEB.pdf
49. Franco A., & Casarosa C. (2014). Thermodynamic and Heat Transfer Analysis of LNG Energy Recovery for Power Production. *Journal of Physics: Conference Series*, *547*
50. Ministry of Economic Affairs and Employment of Finland. (2020). *Investment Incentives to Promote Rapid Phase-Out of Coal in Energy Production.* [online]. [accessed 9 January 2021]. Available at https://valtioneuvosto.fi/en/-/1410877/asetuksella-investointikannuste-hiilen-energiakaytosta-ripeasti-luopuville

sciendo

LATVIAN JOURNAL OF PHYSICS
AND TECHNICAL SCIENCES
2021, N 2

DOI: 10.2478/lpts-2021-0012

CORROSION AND ELECTROCHEMICAL IMPEDANCE SPECTROSCOPY OF THIN TiAlN AND TiCN PVD COATINGS FOR PROTECTION OF BALLAST WATER SCREEN FILTERS

R. Kalnina*, V. Priednieks, K. Lukins, A. Gasparjans, A. Rijkure

Latvian Maritime Academy,
5b Flotes Str., Riga, LV-1016, LATVIA
*e-mail: renate_kalnina@inbox.lv

The electrochemical impedance spectroscopy (EIS) and corrosion behaviour of physical vapour deposited (PVD) TiAlN and TiCN coatings of 50 µm mesh shaped AISI 316 stainless steel were estimated under simulated marine conditions (3.5 wt. % NaCl solution). The coatings were prepared by creating adhesive Cr-CrN interlayer with the thickness of about 0.3 µm. The obtained thicknesses of produced coatings were measured to be in a range between 2 and 3.5 µm. The presence of protective coatings leads to corrosion potential (E_{corr}) shifting to more positive values as compared to the bare stainless steel. This effect indicates higher protection efficiency of coated steel under marine conditions. The protective behaviour of produced coating leads to the decreased corrosion current density (j_{corr}) by indicating up to 40-fold higher polarization resistance as compared to resistance of the naturally formed oxide layer over the stainless steel. The Nyquist and Bode plots were obtained with the help of EIS measurements by applying alternating potential amplitude of 10 mV on observed E_{corr}. The obtained plots were fitted by appropriate equivalent circuits to calculate pore resistance, charge transfer resistance and capacitance. The present study reveals that pore resistance was the highest in the case of TiCN coating (R_{pore}=3.22 kΩ·cm^2). The increase in duration of the immersion up to 24 h leads to change in the capacitive behaviour of the coatings caused by the penetration of the aqueous solution into pore system of TiCN coating with low wettability and surface passivation of reactive TiAlN coating. The presence of defects was confirmed by examining the obtained samples with the help of the scanning electron microscope.

Keywords: *Coatings, corrosion, electrochemical impedance spectroscopy, marine conditions, protection, PVD.*

1. INTRODUCTION

The mechanical degradation of stainless steel components causes the considerable attention during application under the industrial [1], electronics [2] marine, automotive and aerospace [3], [4] conditions for the certain period of exposure to mechanical, chemical, and electrochemical impacts. Ballast water stability and maneuverability are required to ensure the buoyancy of ships. The technological development provides the construction and use of larger sized modern cargo ships. It leads to the highest consumption and more frequent uptake and release of ballast water [5]. Ballast water tanker, pumping, and filtering systems typically experience the combination of above mentioned impacts and other types of severe wear causing factors [6].

It has been recently estimated that between 10 and 12 billion tons of ballast water are transported worldwide each year. The ballast water typically contains bacteria, plankton, viruses, small fish, crabs or jellyfish which are mostly invasive to ecosystems on the route of cruising ships. Studies have shown that around 7,000 marine and coastal species travel daily and frequently cross the world's oceans and seas in such a way. It results in irreversible ecological variations and economic losses [7].

The International Convention for the Control and Management of Ships' Ballast Water and Sediments (BWM 2004) was adopted by the International Maritime Organisation (IMO) in 2004 and subsequently entered into force on 8 September 2017 to perform action for the prevention of such a global environmental problem. The aims of BWM 2004 are to govern the process of ballast water exchange and reduce the risk of invasive aquatic species to influence the foreign ecosystems.

According to BWM 2004, the installations for treatment of ballast water and sediment are required and they should be completely implemented till 8 September 2024. In addition, it is important to underline that BWM 2004 does not define specific water treatment technologies. Eventually, shipowners must make a choice between existing technologies available on the market and innovative technologies recently introduced or currently under research and development. Innovative and sustainable technologies provide a clear advantage in meeting the demand for construction of new ships in accordance with the strictest environmental requirements [5]. The operation of currently applied ballast water management systems (BWMS) typically includes the combination of physical separation with centrifugal force and disinfection (e.g., electro-chlorination and ultraviolet – UV radiation) approaches.

Fixed or movable types of stainless steel-based ballast water screens or disks are typically applied during the pre-treatment stage of BWMS to efficiently remove suspended solids or organisms with sizes above 50 μm. Typical filters include automatic backwash (counter-flow) mechanisms for self-cleaning to ensure continuous operation. The main objective of such an approach is to reduce the degree of disinfection treatment and required contact time. It helps avoid the additional treatment caused by larger sized organisms that block the filter sieve mesh. It also leads to reduced concentration of sediment in ballast water. The presence of sediment particles reduces the efficiency of UV radiation and causes habitat for benthic organisms.

The backwash mode typically leads to the discharge of the suspended/filtered

solids and wastewater from the filter in the same area where the ballast is taken. It should be noted that additional backwash water treatment is recommended before every discharging process [8].

It should be emphasised that all BWMS have been tested under aggressive terrestrial conditions with complex water conditions (different water parameters and large numbers of organisms) to demonstrate that the D-2 standard is met. Therefore, problems that cannot be foreseen are only brought to light in practice mainly due to clogging and corrosion of the screen filters.

The tendency of filters to clog relates primarily to filter design and small mesh sizes [9].

Filters with a nominal pore size in the range ≥10 μm and <50 μm are typically applied to ballast water treatment. Simplistically, the ballast water discharge standard differentiates the target organisms in three size categories: >50 μm sized organisms (predominately zooplankton); 10–50 μm sized organisms (predominately algae) and larger sized bacteria. Most suppliers choose filtration with a cut-point at around 40 μm resulting in an immediate and very efficient removal of zooplankton. The BWMS manufacturers offer 40 μm ballast water self-cleaning filters made of stainless steel 304L, 316L for standard applications [10]. These facts typically cause the demand for the improved resistance of exposed components to reduce the expenditures for the required periodic shutdowns and repairs [11], [12].

The epoxy is one of the most popular currently applied steel elements protecting coating under marine conditions. The wear of such a coating leads to environmental pollution with highly stable microplastics [13]. The global demand for high-performance corrosion and wear resistant coatings and smart approaches stood nearly 14.61 billion US$ in 2018 and was projected to reach over 22.78 billion US$ by 2027 [14]. The partial or complete replacement of microplastics or hazardous compounds generating coatings with more durable thin physical vapour deposited (PVD) coatings and development of innovative structures will evidently play a vital role in environmental protection. Wear, erosion, and corrosion are the most common forms of chemical and mechanical attack. The most common form of degradation is usually initiated at the surface of the materials under the harshest working environments.

Generally, the breakdown of the passive films, crevice corrosion, pitting, galvanic corrosion, inter-granular corrosion, selective leaching, erosion-corrosion, and chemical stress corrosion are more commonly investigated and reviewed types of corrosion in literature. As next to water, steel corroding chlorides are the most common chemicals found in nature. Therefore, chloride caused stress corrosion (cracking) requires more careful examination [15], [16].

It is important to minimise the concentration of growth defects in order to improve the tribological properties of PVD hard coatings [17], [18]. PVD coating technology had intensive progress last decade, and it was successfully adapted even for protection of fine powder coatings. Ceramic hollow particles have been coated with Cu-metal (the thickness of 0.4-2.5 μm) [19], [20]; Ti (0.15–0.25 μm); and Ti-TiN (0.2–0.4 μm) [21]. The protection of Mg-alloys with thin coatings is one of the most challenging objectives to enable the safe application of low density components under marine conditions [22], [23]. Current solutions still cannot meet automotive industry test requirements.

The metallic substrate has no direct contact with the corrosive environment in

case of a typical coating-metal substrate system. However, the presence of voids, pinholes, droplets, poor adhesion, difference in chemical composition between the coating matrix and droplet lead to corrosion [24], [25]. These defects are considered the primary causes of failures in coating/metal systems.

It should be noted that macrodefects caused by inclusions in the dense coating do not always present a break-point in corrosion resistance [26]. Transition metal nitrides are widely applied due to high hardness, high electrically conductivity, and good corrosion resistance [27], [28]. Corrosion resistance of hard coatings, like TiAlN, TiN, and TiCN, depends on microstructure defects. Such hard coatings typically exhibit trans-passive state under marine water conditions [28].

The mechanism of corrosion and material microstructure both play an important role in the corrosion process [29]. A coating/metal substrate system is examined in the present study to understand the effect of galvanic corrosion caused by the presence of defects in the coating. Electrochemical reaction is the prevalent corrosion mode. Electrochemical characterisation of the tested coatings is performed in the present study to investigate their corrosion behaviours in a simulated marine (corrosive) environment.

The corrosion behaviour of produced coated samples is studied and compared with the help of potentiodynamic polarization and the electrochemical impedance spectroscopy (EIS) methods. It should be noted that quantitative evaluation of the kinetic parameters for the observed corrosion mechanisms is a complicated process by employing the potentiodynamic polarization technique alone [30]CrN, TiAlN and multilayer TiAlN/CrN coatings, deposited on steel substrate using a multi-target reactive direct current magnetron sputtering process, were studied in 3.5% NaCl solution by potentiodynamic polarization and electrochemical impedance spectroscopy (EIS). More detailed information about the electrochemical reaction at the electrode/electrolyte interface can be interpreted with the help of appropriate equivalent circuit supported EIS measurement data. The use of EIS technique allows detecting the resistive and capacitive nature of the electrochemical interface, thus identifying the effect of micropores on the localized corrosion behaviour.

2. THE OBJECT FOR RESEARCH AND DEVELOPMENT

The high-quality stainless steel screen offered by most vendors has a relatively short lifespan. The failed stainless steel AISI 316L screen filter after 6-month long operation under real operational conditions was selected for preliminarily research and development activities at the *Latvian Maritime Academy* (LMA), as demonstrated in Fig. 1. The chemical and galvanic corrosion was observed as the main cause of the screen filter failure in addition to solid particles containing slurry that caused abrasive wear of the formed corrosion product layer (e.g., rust). Therefore, it was decided to apply hard coating over the stainless steel screen filter material to estimate the chemical and electrochemical corrosion resistance under simulated marine conditions.

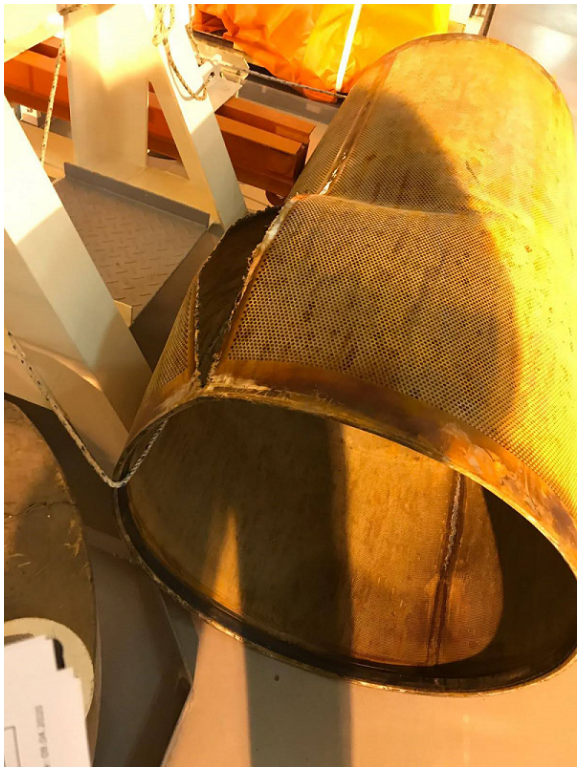

Fig. 1. Failed screen filter after 6-month service under real conditions.

3. EXPERIMENTAL METHODS

The 50 µm mesh shaped flat substrate samples of stainless steel AISI 316 (EN 1.4401) with dimensions of 25×15×2 mm were polished with the help of the diamond polishing disc and SiC polishing pads down to 0.5 µm. The produced substrates were cleaned by immersion in the ultrasonic bath for 1 h with subsequent drying under vacuum and final sputter-cleaning in argon plasma with bias voltage -850 V at 400 °C for 1 h. The Cr-CrN interlayer with the thickness of about 0.3 µm was created to provide high adhesion strength between stainless steel substrate and the selected coatings. The interlayer coating and TiCN and TiAlN coatings (with a content of Al 0 and 55 at. %, respectively) were deposited on substrate with the help of a modernised vacuum installation NNV-6,6-I1 [31], the operating principle of which is based on the method of PVD under a reactive nitrogen atmosphere. The deposition temperature for each coating was 500 °C.

The obtained specimens are marked as follows: uncoated AISI 316 (R), coated with TiCN (A) and TiAlN (B). A scanning electron microscope *Hitachi TM3000 (Tabletop)* equipped with energy-dispersive X-ray spectroscopy (EDS) was used to observe the surface morphology. The thickness of produced coatings was measured with the help of the kalotest method according to the method developed by *BAQ* (Germany).

Potentiodynamic polarization and electrochemical impedance spectroscopy measurements were performed under simulated

marine conditions (3.5 wt. % NaCl solution) in the three-electrode (potentiostatic) mode in the presence of the saturated calomel reference electrode (SCE) and platinum (Pt) counter electrode (CE) with a working surface of 2 cm^2. Protective silicone isolated specimens with an exposed surface area of about 1 cm^2 were used as working electrodes (WE).

Potentiodynamic polarization measurements were performed using Autolab PGSTAT30 galvanostat/potentiostat system with General Purpose Electrochemical System GPES software. After the open circuit potential (E_{OCP}) stabilization, lower potential limits of linear sweep voltammetry were set in a range between -0.7 and 0 V by selecting a scan rate of 5 $mV \cdot s^{-1}$.

According to Faraday's law, the penetration rate is calculated by Eq. (1):

$$CR = K_1 \cdot \frac{i_{corr}}{\rho} \cdot EW_{alloy}, \quad (1)$$

where CR – the penetration rate (the thickness loss per unit of time), $mm \cdot year^{-1}$; $K_1 = 3.3 \cdot 10^{-3}$ $mm \cdot year^{-1}$ (only consistent valence groupings were used); i_{corr} – corrosion current density ($\mu A \cdot cm^{-2}$); ρ – alloy density, ($g \cdot cm^{-2}$); EW_{alloy} – the alloy equivalent weight (dimensionless in this calculation) [32].

The protective efficiency P_i (%) of the coating was calculated as follows:

$$P_i = \left[1 - \frac{i_{corr}}{i_{corr}^0}\right] \times 100, \quad (2)$$

where i_{corr} and i_{corr}^0 indicate the corrosion current density of the coating and substrate, respectively.

The porosity F (%) of coating is calculated according to Eq. (3):

$$F = \left[\frac{R_{pm}}{R_p} \times 10^{-\left|{}^{\Delta E_{corr}}/_{\beta_a}\right|}\right] \times 100, \quad (3)$$

where R_{pm} and R_p are the polarization resistances of the substrate and coating-substrate systems (calculated by GPES according to Eq. (4)), respectively; ΔE_{corr} is the corrosion potential difference between the substrate and applied coating, and β_a is the anodic Tafel constant of substrate [33].

$$R_p(R_{pm}) = \left(\frac{\delta \Delta E}{\delta i}\right)_{i=0,\ {}^{dE}/_{dt} \to 0}, \quad (4)$$

where a small potential scan $\Delta E(t)$ is defined with respect to the corrosion potential shown in Eq. (5) [32]:

$$\Delta E = E - E_{corr}. \quad (5)$$

3.1. Electrochemical Impedance Spectroscopy

Alternating current (AC) impedance for all specimens was derived using an *AutoLab* with potentiostat/galvanostat *PGSTAT30* and Frequency Response Analyzer (FRA) module. A sinusoidal AC perturbation of 10 mV amplitude was applied to the electrode at the observed E_{corr} over the frequency range of 10 mHz to 10 kHz after short (approximately 10 min) and long (approximately 24 h) exposure time in a corrosive medium before testing by applying the observed E_{corr} (conditioning). *NOVA 2* software was used for the analysis of the obtained plots and fitting to the selected equivalent circuits. Equivalent circuits were generated with the help of the *EQUIVCRT* software. It should be noted that specimens exposed for a long period were immersed in the fresh 3.5 wt. % NaCl solution to avoid the effect of NaCl concentration changes caused by reactions and evaporation of the liquid phase.

4. RESULTS AND DISCUSSION

The SEM images of the surface morphology of the as-deposited TiCN and TiAlN coatings are shown in Fig. 2.

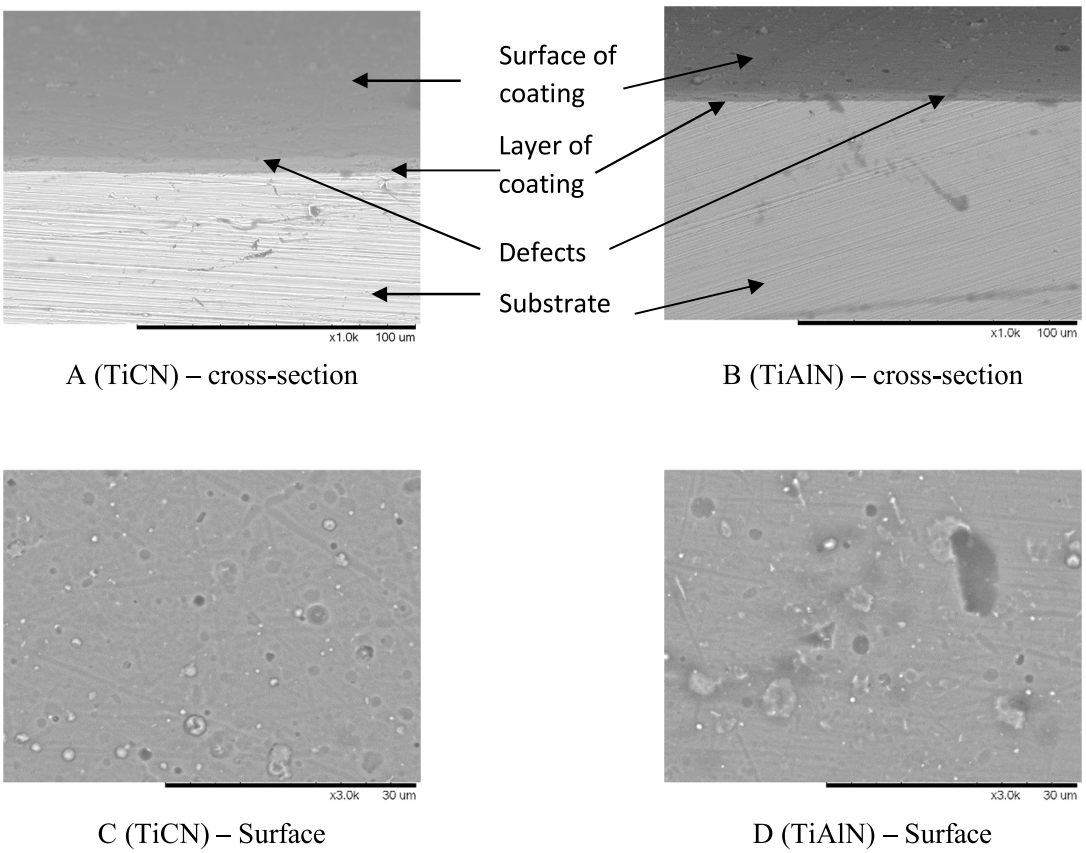

Fig. 2. SEM coating and substrate cross-sections of TiCN (A) and TiAlN (B); and morphology of as-deposited coatings TiCN (C) and TiAlN (D).

The Tafel plots obtained for steel substrate and coated specimens are shown in Fig. 3, and the obtained potentiodynamic polarization data from GPES are shown in Table 1. E_{corr} of the steel substrate is about -0.36 V and i_{corr} is 1.79 μA·cm^{-2}. TiCN and TiAlN coatings show that E_{corr} shifts towards the positive side (-0.19 and -0.18 V) with down to 20-fold lower i_{corr} as compared to the substrate. These results indicate better corrosion resistance for TiCN and TiAlN coatings over steel substrate, confirming that the transition metal nitrides are more inert to a chemical attack.

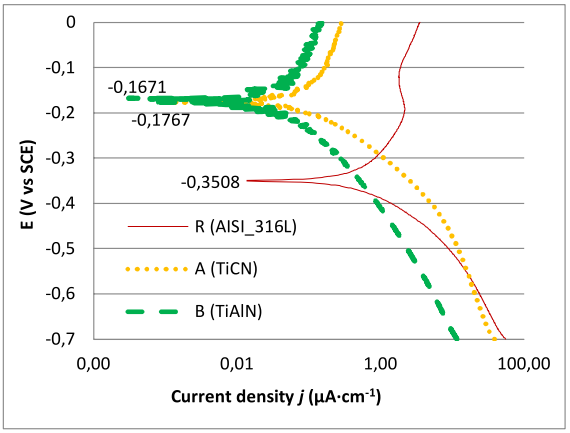

Fig. 3. Potentiodynamic polarization curves (Tafel plots) of as-received tested specimens.

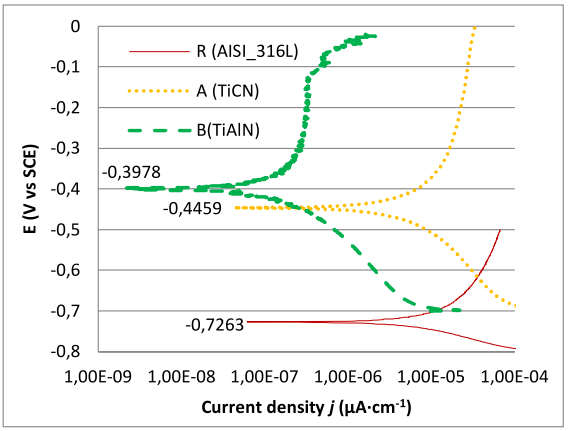

Fig. 4. Potentiodynamic polarization curves (Tafel plots) of as-received tested specimens after 24 h immersion.

Table 1. Potentiodynamic Polarization Data of Tested Specimens in 3.5 wt.% NaCl Solution

	E_{corr}	i_{corr}	β_a	β_c	R_{pm}, R_p
	(V)	(μA·cm^{-2})	(V·decade^{-1})	(V·decade^{-1})	(Ω·cm $^{-2}$)
R	-0.36	1.79	0.08	0.15	$1.24 \cdot 10^4$
A	-0.19	0.19	0.09	0.30	$1.60 \cdot 10^5$
B	-0.18	0.09	0.16	0.35	$5.27 \cdot 10^5$

Table 2. Penetration Rate, Protective Efficiency and Porosity Calculation Results from Potentiodynamic Polarization Data after 24 h Immersion

	CR	P_i	F
	(mm·year^{-1})	(%)	(%)
R	$3.75 \cdot 10^{-3}$	-	-
A	$8.43 \cdot 10^{-4}$	89.24	0.51
B	$4.94 \cdot 10^{-4}$	94.98	0.01

The obtained Nyquist plots exhibit an overlay of at least two semicircles for all the samples, indicating multiple time constants due to a short exposure time in the simulated marine environment. It could be concluded that the applied short exposure duration (10 min) is not sufficient to reveal the significant degradation of the substrate [30], [34], as shown in Fig. 5. The TiAlN coated material exposed for a short period exhibits the highest charge transfer resistance (R_{ct}) as compared to TiCN coated sample exposed for a short period, as demonstrated in Table 3. The absolute impedance increases in the same order (AISI 316; TiCN, and TiAlN), as demonstrated in Fig. 6 a (log|Z| vs. log (f) – Bode plot). Phase angles of stainless steel and coated samples are about 67 and 77°, respectively, as demonstrated in Fig. 6 b (phase angle vs. log (f) – Bode plot). This result indicates a slightly more homogeneous surface of coated samples as compared to uncoated stainless steel. The inhomogeneous behaviour of stainless steel can be explained with the effect of the naturally formed oxide coating on the alloy surface which consists of different types of oxides with different resistance to degradation under simulated marine conditions.

The generated equivalent circuit for AISI 316 stainless steel substrate after long exposure (24 h) is demonstrated in Fig. 8. This circuit consists of double layer capacitance (Q_{dl}) parallel to the charge transfer resistance (R_{ct}). Both are in series with the solution resistance (R_s) located between the working electrode (WE) and the tip of the *Lugging* capillary. The *EQUIVCRT* software is programmed to regard the Q for the constant phase element. This element accounts for deviations from ideal dielectric behaviour related to the surface inhomogeneities, calculated according to Eq. (6):

$$Y(\omega) = Y_0(j \cdot \omega)^{n_{dl}}, \quad (6)$$

where Y_0 is the adjustable parameter applied to non-linear least squares fitting; n_{dl} is an adjustable parameter in the range from 0.5 up to 1 and is generated from the slope of log|Z| vs. log (f) (Bode plot). The phase angle $\boldsymbol{\theta}$ varies between 0° (n_{dl}=0 in the case of a perfect resistor) and 90° (n_{dl}=1 in the case of a perfect capacitor). A value of $\boldsymbol{\theta}$ between 60 and 70° represents a leaky capacitor behaviour of stainless steel with n_{dl}=0.78). TiCN and TiAlN exposed for a short period exhibit perfect resistor and capacitor behaviour, respectively. These effects can be explained with high passivity of the TiCN coatings to the saline water and low wettability caused by the presence of carbon [35], which also limits the penetration of the water into pores of the coating. However, the presence of aluminium in the TiAlN coating leads to a hydrolyzation reaction between free Al and water. Corrosion products like amorphous aluminium monohydroxide ($AlOOH_{amorph}$) and crystalline aluminium hydroxide ($Al(OH)_{3crystal}$) form and generate the highly passivating layer on the surface of the TiAlN coating [36].

This effect leads to replacement of double layer capacitance (C_{dl}) by the constant phase element at n_{dl}<1. The circuit description code (CDC) for the AISI 316 stainless steel after 24h long exposure to aqueous 3.5 wt. % NaCl solution matches the *R[QR]*, as demonstrated in Fig. 8.

The low coating thickness typically leads to rapid formation of localized galvanic cells (galvanic corrosion occurs) due to penetration of aqueous solution (electrolyte) into pores almost immediately after the immersion of coated material [37] of the equivalent circuits for electrochemical impedance spectroscopy (EIS). Therefore, corrosion occurs at two interfaces consisting of electrolyte coating and electrolyte substrate. The presence of an adhesive

interlayer and the use of gradient or multilayer PVD coatings typically cause additional galvanic corrosion sub-interfaces between layers with different electrochemical properties (potentials).

Previous exposure of specimen to the air leads to a slight reduction in a corrosion rate caused by the decreased aqueous solution penetration rate through the defects of coatings even after bubbling of cell with nitrogen gas. The finite length diffusion process requires the adoption of the cotangent diffusion element (O) in series with the charge transfer resistance in CDC of tested PVD TiCN and TiAlN coatings. The resulting CDC can be expressed as $R(Q[R(Q[RO])])$ to fit the electrochemical impedance spectroscopy data of the coated samples after 24h immersion in the simulated marine conditions, as demonstrated in Fig. 9. The cotangent diffusion element is typically applied for simulation of finite length diffusion in the case of one boundary imposing a fixed concentration for diffusing species [38]; therefore, the complex admittance of finite length diffusion can be expressed according to Eq. (7).

$$Y(\omega) = \{Y_0(j \cdot \omega)^{1/2}\}\coth\,[BY_0(j \cdot \omega)^{1/2}]. \quad (7)$$

The equation includes two parameters – an admittance (Y_0) and a time constant (B). Reactant diffusion duration through the coating is characterised by the "time constant" parameter, which can be expressed according to Eq. (8).

$$B = \frac{\delta}{\sqrt{D}}, \quad (8)$$

where D is the diffusion coefficient and δ is the thickness of the coating.

The coating capacitance (Q_{coat}) value after 24 h exposure is the highest for TiCN (94), indicating a more homogeneous surface as compared to TiAlN coated specimen. The inhomogeneity of TiAlN coating contributes not only to the surface roughness and defects in the coating, but also to the presence of reactive Al and coating generated by the reaction products (e.g., AlOOH) [18]. The aqueous 3.5 wt. % NaCl solution penetrates trough all defects of the original coating and reaction products by accessing the unreacted material.

The presence of micrometre sized pores in the tested coatings results in the decreased coating capacitance and the increased charge transfer resistance after 24 h long exposure. The long exposure results in insignificant variations in the Q_{dl} and n_{dl} values of the tested coatings as compared to the stainless steel substrate. The shape of Bode plots after long exposure indicates the same corrosion mechanisms occurring in TiCN and TiAlN coatings.

Table 3. EIS Data Obtained by Equivalent Circuit to Fit Tested Coatings Studied after 10 min and 24h Immersion

Tested specimen	R_s ($\Omega \cdot cm^2$)	C_{coat}-Y_0 ($\mu F \cdot cm^{-2}$)	n_{coat}	R_{pore} ($\Omega \cdot cm^2$)	Q_{dl}-Y_0 ($\mu F \cdot cm^{-2}$)	n_{dl}	R_{ct} ($k\Omega \cdot cm^2$)	O-Y_0 ($\mu\Omega \cdot cm^2 \cdot \sqrt{s}$)	B ($\sqrt{s}$)
R (AISI 316)$_{10\ min}$	18.1	-	-	-	83.1	0.78	82	-	-
R (AISI 316)$_{24h}$	18.5	-	-	-	0.16	0.90	1.62	-	-
A (TiCN)$_{10\ min}$	19.5	6.36	0.84	3.22	$900 \cdot 10^{-13}$	0	2.47	18.1	$6.47 \cdot 10^{-6}$
A (TiCN)$_{24h}$	18.4	94.0	0.72	180	0.10	0.76	2.17	2704	1.51
B (TiAlN)$_{10\ min}$	20.1	37.0	0.85	0.21	9.88	1.00	14.3	19.7	1.52
B (TiAlN)$_{24h}$	19.4	91.1	0.85	390	0.16	0.96	3.51	12700	8.74

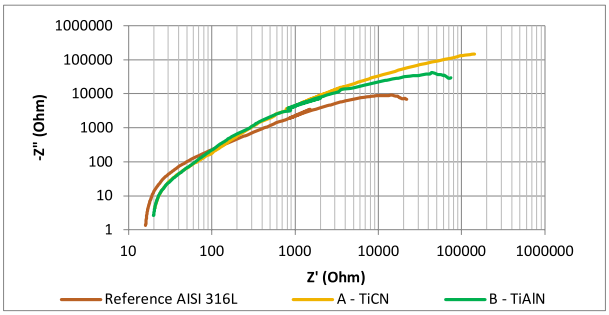

Fig. 5. Nyquist plots of the tested specimens after 10 min immersion.

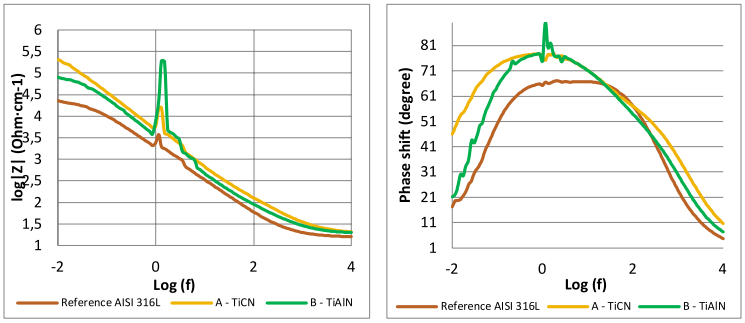

a b

Fig. 6. Bode plots of the tested specimens after 10 min immersion:
(b) – log|Z| vs. log (f); (a) – phase angle vs. log (f).

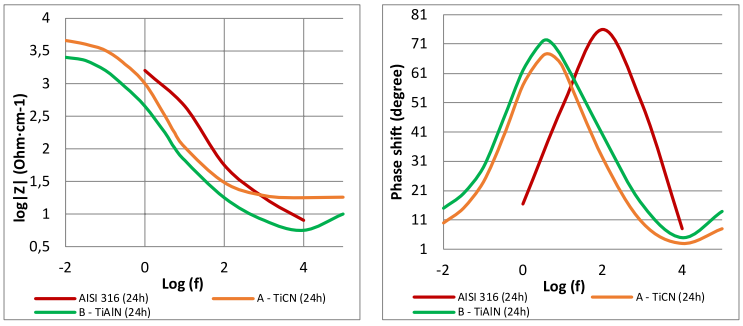

a b

Fig. 7. Bode plots of the tested specimens after 24 h immersion:
(b) – log|Z| vs. log (f); (a) – phase angle vs. log (f).

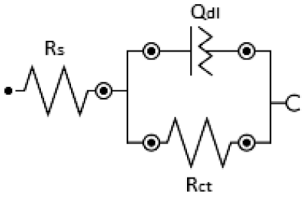

Fig. 8. Equivalent circuit to fit the electrochemical impedance spectroscopy data of the AISI 316 after 10 min immersion.

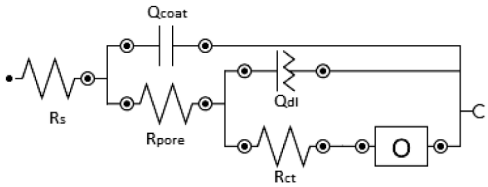

Fig. 9. Equivalent circuit to fit the electrochemical impedance spectroscopy data of the coated samples after 24h immersion.

5. CONCLUSIONS

The thickness of the produced TiCN and TiAlN coatings from 2 up to 3.5 μm provides up to 95 % higher protective efficiency as compared to the surface of the mesh shaped stainless steel AISI 316 substrate (reference sample) after 10 min immersion and 24 h exposure under simulated marine conditions (3.5 wt. % NaCl solution). The selected PVD coating method leads to the formation of low porosity (up to 0.51 % in the case of TiCN). The presence of free Al in TiAlN coating leads to the formation of passive AlOOH reaction product.

The increased duration of immersion up to 24 h leads to penetration of liquid inside the pinholes and macrodefects with diameters less than 10 μm. This process results in E_{corr} shifting toward a more negative potential as compared to samples after immersion for a short period of time. It can be concluded that TiAlN PVD gradient coating can provide higher protection efficiency after short immersion time, while TiCN PVD gradient coating can maintain less changed protective efficiency after 24 h long immersion under the simulated marine conditions (3.5 wt. % NaCl solution).

The EIS measurements indicate that TiAlN coating exhibits better corrosion resistance after 24h exposure to the simulated marine condition due to the formation of AlOOH as compared to the tested TiCN coated and uncoated mesh shaped stainless steel 316.

ACKNOWLEDGEMENTS

The research has been supported by the by the Ministry of Education and Science of Latvia within postdoctoral research project No. 1.1.1.2/VIAA/3/19/477. The authors thank the teams of Riga Technical University (Latvia), Klaipeda University (Lithuania), and Tallinn University of Technology (Estonia) for support in providing the failed screen filter, production of specimens, and electrochemical performance tests, respectively.

REFERENCES

1. Irtiseva, K., Baronins, J., Krūmiņš, J., Ozolins, J., Kļaviņš, M., & Medne, O. (2020). Development of Peat Processing Methods for Production of Innovative Products. *Key Eng. Mater.*, *850*, 9–15.
2. Kommel, L., & Baronins, J. (2017). Dependence of Wear of Cu-Cr-S Alloy on Hardness and Electrical Conductivity in Sliding Electrical Contact. *Solid State Phenomena, 267*, 229–233.
3. Arshad, A., Samarasinghe, S., Akeel, F.A.M., & Urbahs, A. (2020). A Simplified Design Approach for High-Speed Wind Tunnels. Part I: Table of Inclination. *J. Mech. Sci. Technol.*, *34*, 2455–2468.
4. Arshad, A., Andrew, N., & Blumbergs, I. (2020). Computational Study of noise reduction in CFM56-5B using core nozzle chevrons. In: *Proceedings of the 11th International Conference on Mechanical and Aerospace Engineering* (ICMAE) (pp. 162–167), IEEE, 2020.
5. Kalniņa, R., & Romule, A. (2020). Analysis of Ballast Water Treatment Technologies on Ships Operating in the Baltic Sea Region. *Transp. Aerosp. Eng.*, *8*, 15–20.
6. Shishkin, A., Mironovs, V., Vu, H., Novak, P., Baronins, J., Polyakov, A., & Ozolins, J. Cavitation-Dispersion Method for Copper Cementation from Wastewater by Iron Powder. *Metals (Basel)*, *8*, 920.
7. WWF International. (2009). *Silent invasion – The spread of marine invasive species via ships' ballast water*. Gland, Switzerland.
8. Drake, L.A., Wier, T.P., Parson, E.W.J., & Grant, J.F. (2016). *Recommendations for evaluating multiple filters in ballast water management systems for US type approval*. USA: Naval Research Laboratory.
9. ALfa Laval Corporate AB. (2017). *Muddy waters and filter clogging in ballast water treatment*. Tigre, Argentina. Available at https://www.alfalaval.lat/globalassets/documents/products/process-solutions/ballast-water-solutions/muddy_waters_and_filter_clogging_in_ballast_water_treatment.pdf
10. Andersen, A.B. (2017). *Should you Accept Stainless Steel Filter-Screens in your Ballast Water Management System?* Available at https://www.linkedin.com/pulse/should-you-accept-stainless-steel-filter-screens-your-andersen/
11. Bhushan, B., & Gupta, B.K. (1991). *Handbook of tribology: Materials, coatings, and surface treatments*. USA: McGraw-Hill.
12. Cai, F. (2011). *Tribological and electrochemical corrosion behaviours of titanium nitride and chromium nitride based PVD coating systems.* PhD Thesis. Princeton: Princeton University. ISBN 9780494815458.
13. Sharifinia, M., Bahmanbeigloo, Z.A., Keshavarzifard, M., Khanjani, M.H., & Lyons, B.P. (2020). Microplastic Pollution as a Grand Challenge in Marine Research: A Closer Look at their Adverse Impacts on the Immune and Reproductive Systems. *Ecotoxicol. Environ. Saf.*, *204*, 111109.
14. Transparency Market Research. (n.d.). *High-Performance Anti-Corrosion Coatings Market.* Available at https://www.transparencymarketresearch.com/high-performance-anticorrosion-coatings-market.html
15. Méndez, C.M., Covinich, M.M., & Ares, A.E. (2013). Resistance to corrosion and passivity of 316L stainless steel directionally solidified samples. In M. Aliofkhazraei (Ed.), *Developments in Corrosion Protection* (pp. 41–63). ISBN 978-953-51-1223-5.
16. Baronins, J., Podgursky, V., Antonov, M., Bereznev, S., & Hussainova, I. (2016). Electrochemical Behaviour of TiCN and TiAlN Gradient Coatings Prepared by Lateral Rotating Cathode Arc PVD Technology. *Key Eng. Mater.*, *721*, 414–418.
17. Panjan, P., Čekada, M., Panjan, M., & Kek-Merl, D. (2009). Growth Defects in PVD Hard Coatings. *Vacuum*, *84*, 209–214.

18. Baronins, J., Antonov, M., Bereznev, S., Raadik, T., & Hussainova, I. (2018). Raman Spectroscopy for Reliability Assessment of Multilayered AlCrN Coating in Tribo-Corrosive Conditions. *Coatings*, *8* (7), 229.
19. Shishkin, A., Kozlov, V., Drozdova, M., Rulev, J., Mironov, V., & Hussainova, I. (2016). Low-density composite powder for lightweight parts made by means powder metallurgy. In Proceedings of the World PM2016; European Powder Metallurgy Association (EPMA) (pp. 93–94). 9–13 October 2016, Hamburg, Germany.
20. Shishkin, A., Drozdova, M., Kozlov, V., Hussainova, I., & Lehmhus, D. (2017). Vibration-Assisted Sputter Coating of Cenospheres: A New Approach for Realizing Cu-Based Metal Matrix Syntactic Foams. *Metals (Basel)*, *7*, 16.
21. Shishkin, A., Hussainova, I., Kozlov, V., Lisnanskis, M., Leroy, P., & Lehmhus, D. (2018). Metal-Coated Cenospheres Obtained via Magnetron Sputter Coating: A New Precursor for Syntactic Foams. *JOM, 70* (7), 1319–1325.
22. Hoche, H., Groß, S., & Oechsner, M. (2014). Development of New PVD Coatings for Magnesium Alloys with Improved Corrosion Properties. *Surf. Coatings Technol.*, *259*, 102–108.
23. Taha, M.A., El-Mahallawy, N.A., Hammouda, R.M., & Nassef, S.I. (2010). PVD Coating of Mg-AZ31 by Thin Layer of Al and Al-Si. *J. Coatings Technol. Res.*, *7*, 793–800.
24. Wang, C.,Wang, G., Feng, Z., Ji, X., Li, Q., Zhang, Z., & Song, D. (2011). Strengthen Water Conservancy Construction, Use Water Resources Scientifically, and Develop Modern Agriculture. *Procedia Environ. Sci.*, *10*, 1595–1600.
25. Williams, J. A. (1999). Wear Modelling: Analytical, Computational And Mapping: A Continuum Mechanics Approach. *Wear*, *225–229*, 1–17.
26. Merl, D.K., Panjan, P., Panjan, M., & Čekada, M. (2007). The Role of Surface Defects Density on Corrosion Resistance of PVD Hard Coatings. *Plasma Process. Polym.*, *4*, 613–617.
27. Yang, M., Allen, A.J., Nguyen, M.T., Ralston, W.T., MacLeod, M.J., & DiSalvo, F.J. (2013). Corrosion Behavior of Mesoporous Transition Metal Nitrides. *J. Solid State Chem.*, *205*, 49–56.
28. Ibrahim, M.A.M., Korablov, S.F., & Yoshimura, M. (2002). Corrosion of Stainless Steel Coated with TiN, (TiAl)N and CrN in Aqueous Environments. *Corros. Sci.*, *44*, 815–828.
29. Baronins, J., Antonov, M., Bereznev, S., Raadik, T., & Hussainova, I. (2019). Raman Spectroscopy of Multilayered AlCrN Coating under High Temperature Sliding/ Oxidation. *Key Eng. Mater.*, *799*, 9–14.
30. William Grips, V.K., Barshilia, H.C., Selvi, V.E., & Rajam, K.S. (2006). Electrochemical Behavior of Single Layer CrN, TiN, TiAlN Coatings and Nanolayered TiAlN/CrN Multilayer Coatings Prepared by Reactive Direct Current Magnetron Sputtering. *Thin Solid Films*, *514*, 204–211.
31. Urbahs, A., Savkovs, K., Urbaha, M., & Kurjanovičs, I. (2012). Nanostructured Intermetal-Ceramic Coatings for Blades of Gas Turbine Engines. *Nanodevices and Nanomaterials for Ecological Security: NATO Science for Peace and Security Series B: Physics and Biophysics,* 307–314. Dordrecht: Springer.
32. ASTM. (1997). *ASTM G59 – 97e1 Standard Test Method for Conducting Potentiodynamic Polarization Resistance Measurements*. ASTM International: West Conshohocken.
33. Yoo, Y.H., Le, D.P., Kim, J.G., Kim, S.K., & Van Vinh, P. (2008). Corrosion Behavior of TiN, TiAlN, TiAlSiN Thin Films Deposited on Tool Steel in the 3.5 wt.% NaCl Solution. *Thin Solid Films*, *516*, 3544–3548.
34. Liu, H.-N., Nomura, M., Ogi, K., & Sakamoto, M. (2001). Abrasion Resistance of High Cr Cast Irons at an Elevated Temperature. *Wear*, *250*, 71–75.
35. Subramanian, B., Thampi, A., Manivasagam, G., & Dhandapani, P. (2015). Influence of Needle-Like Morphology on the Bioactivity of Nanocrystalline Wollastonite – An in Vitro Study. *Int. J. Nanomedicine*, 107–118.

36. Bowen, P., Highfield, J.G., Mocellin, A., & Ring, T.A. (1990). Degradation of Aluminum Nitride Powder in an Aqueous Environmet. *J. Am. Ceram. Soc.*, *73*, 724–728.
37. Liu, C., Bi, Q., Leyland, A., & Matthews, A. (2003). An Electrochemical Impedance Spectroscopy Study of the Corrosion Behavior of PVD Coated Steels in 0.5 N NaCl Aqueous Solution: Part II. EIS Interpretation of Corrossion Behaviour. *Corros. Sci.*, *45*, 1257–1273.
38. BOUKAMP, B. A (1986). Nonlinear Least Squares Fit Procedure for Analysis of Immittance Data of Electrochemical Systems. *Solid State Ionics*, *20*, 31–44.